University of Southampton

PhD Thesis

High–lift actuation weight estimation using low–cost methods

Author:
Benjamin Moss

Supervisor:
Prof. Andrea Da Ronch

A thesis submitted
towards the degree of Doctor of Philosophy

in the

Aerodynamics and Flight Mechanics Research Group
Aeronautical and Astronautical Engineering

15th October, 2021

Declaration of Authorship

I, Benjamin Moss, declare that this thesis titled, "High–lift actuation weight estimation using low–cost methods" and the work presented in it are my own. I confirm that: I confirm that:

1. This thesis and the work presented in it is my own and has been generated by me as the result of my own original research.
2. This work was done wholly or mainly while in candidature for a research degree at this University;
3. Where any part of this thesis has previously been submitted for a degree or any other qualification at this University or any other institution, this has been clearly stated;
4. Where I have consulted the published work of others, this is always clearly attributed;
5. Where I have quoted from the work of others, the source is always given. With the exception of such quotations, this thesis is entirely my own work;
6. I have acknowledged all main sources of help;
7. Where the thesis is based on work done by myself jointly with others, I have made clear exactly what was done by others and what I have contributed myself;
8. Parts of this work have been published: [1], [2], [3].

[1] B. R. Moss, A. Da Ronch, and N. Tyler, "High-Lift Actuation Weight Estimation using Low Cost Methods," AIAA, 2020.

[2] B. R. Moss, A. K. Bagheri, and A. D. Ronch, "Effect of mesh characteristics on the flow solutions around a multi–element airfoil using su2," in *AIAA AVIATION 2020 FORUM*. DOI: 10.2514/6.2020-3218. eprint: https://arc.aiaa.org/doi/pdf/10.2514/6.2020-3218. [Online]. Available: https://arc.aiaa.org/doi/abs/10.2514/6.2020-3218.

[3] B. R. Moss, A. D. Ronch, and C. Conti, "Quantifying the impact of high-lift actuator mass on dynamic aeroelasticity for the nasa common research model," in *AIAA Scitech 2021 Forum*. DOI: 10.2514/6.2021-0907. eprint: https://arc.aiaa.org/doi/pdf/10.2514/6.2021-0907. [Online]. Available: https://arc.aiaa.org/doi/abs/10.2514/6.2021-0907.

Signed:
Date:

"*Big whorls have little whorls*
Which feed on their velocity,
And little whorls have lesser whorls
And so on to viscosity."

Lewis Fry Richardson

Acknowledgements

There are a lot of people I need to thank, without whom completing my PhD would have not been possible.

Firstly I would like to thank my supervisor, Prof. Andrea Da Ronch, who has been one of the few constants with my PhD. He has provided me a lot of guidance and has pushed me to be more rigorous in all of my work. To my second supervisor Dr Scott Walker, I am grateful for his high-level guidance and pastoral support at times when I felt lost in the weeds of being a research student.

I am extremely thankful for my industrial sponsors and collaborators Airbus UK, Filton and to Moog Aircraft Group, Wolverhampton. At Airbus, I am particularly grateful to Thomas Engelbrecht and Murray Cross who have always made time to meet with me and to put their wealth of aircraft design knowledge at my disposal. Both never hesitated to introduce me to the right people at the right time. At Moog, I would like to express a deep gratitude to Neil Tyler for providing me with a huge array of knowledge and data on high-lift actuation design. His input has been truly game-changing for my doctorate. I am also unexpectedly grateful to Maj. Danny Downham and all of the team at 510 Specialist Team, Royal Engineers for their timely support in the final weeks of my write-up.

Though he wasn't present in person for the final year, I am extremely grateful to my dear friend Dr Christian Laurent for being my PhD 'daddy'. A sublime conversationalist, among much else he taught exactly how much mischief a PhD required (and could tolerate). He would make an excellent PhD supervisor. I must also thank Claudio Conti. Without him, Chapter 6 would not have been possible. He is a far superior engineer to me and I am looking forward to seeing the output of his own doctorate.

I couldn't write an acknowledgement without thanking my parents, Capt. Robert Moss and Dr Jane Fallows. Having been through a PhD programme herself, Mum has knows the ordeal first-hand. I don't know what I would have done without knowing they were a phone call away.

Finally, and most importantly, to Gwen. With no other ties to the place, she moved to Southampton with me when I told her that I wanted to do a study for a doctorate here. She has always been there for me, and I hope always will. I love her very much.

I would like to acknowledges the financial support from the Engineering and Physical Sciences Research Council (EPSRC) Industrial CASE studentship supported by Airbus Operations SAS (17100044). The author also acknowledge the use of the IRIDIS High–Performance Computing Facility, and associated support services at the University of Southampton, in the completion of this work.

UNIVERSITY OF SOUTHAMPTON

Abstract

Faculty of Engineering and Physical Sciences
Aeronautical and Astronautical Engineering

Doctor of Philosophy

High–lift actuation weight estimation using low–cost methods

by Benjamin Moss

Civil passenger aircraft use high-power actuation systems to deploy high–lift surfaces on the leading and trailing edges of their wings. The mass and size of these systems scales with the expected load the high–lift surfaces are deploy. The problem is that estimated maximum panel loads are not known to a high degree of confidence in the conceptual and preliminary phases of design. The concequence of this in the early phases of the design cycle is that actuation system mass cannot be incorporated to any optimisation loop and traded off against design variables as part of an aerostructural optimisation. This increases uncertainty in the wing weight and the corresponding structural design margins. Ultimately, this uncertainty degrades performance and provides pessimistic estimates of dynamic aeroelastic response.

This thesis presents a solution in three parts. First it presents a method for estimating the high–lift actuation system using the aircraft's high–lift geometry. Second, it introduces a novel approach to estimating high-lift panel loads using low cost computational methods suitable for conceptual and preliminary aircraft design. Third, it quantifies the impact of the high–lift actuation system on the dynamic aeroelastic response.

Contents

List of Figures

List of Tables

List of Abbreviations

2D/3D	**2-D**imensional/**3-D**imensional
AR	**A**spect **R**atio
ASSO	**A**erostructural **S**hape **O**ptimisation
CFD	**C**omputation **F**luid **D**ynamics
CLB	Climb
CO_2	Carbon dioxide
CoP	**C**entre **o**f **P**ressure
CRM	NASA **C**ommon **R**esearch **M**odel
CRZ	Cruise
DES	Descent
DoE	**D**esign **o**f **E**xperiments
DS	**D**ouble **S**lotted flap
DSF	**D**ouble **S**lotted **F**owler flap
DSM	**D**esign **S**tructure **M**atrix
EASA	**E**uropean **A**viation and **S**afety **A**uthority
FEM	**F**inite **E**lement **M**ethod
FFT	**F**ast **F**ourier **T**ransform
FL	**F**light **L**evel
GRA	**G**eared **R**otary **A**ctuator
HLSM	**H**igh–**L**ift **S**urrogate **M**odel
HLPW3	**H**igh–**L**ift **P**rediction **W**orkshop **3**
I/B	**In**board
IDF	**I**ndividual **D**isciplinary **F**easible
IFR	**I**nstrument **F**light **R**ules
ISW	**I**nfinite **S**wept **W**ing
LFL	**L**anding **F**ield **L**ength
LHS	**L**atin **H**ypercube **S**ampling
MAC	**M**ean **A**erodynamic **C**hord
MDF	**M**ulti-**d**isciplinary **F**easible
MDO	**M**ulti-disciplinary **D**esign **O**ptimisation
MG	**M**aturity **G**ate
MLW	**M**aximum **T**ake-**o**ff **W**eight
MTOW	**M**aximum **L**anding **W**eight
NS	**N**avier-**S**tokes
O/B	**O**ut**b**oard
OAD	**O**rthogonal **A**rray **D**esign
OEI	**O**ne **E**ngine **I**noperable
OEW	**O**perating **E**mpty **W**eight
OLHS	**O**ptimised **L**atin **H**ypercube **S**ampling
PAX	Passenger
PDE	**P**artial **D**ifferential **E**quation
PDU	**P**ower **D**rive **U**nit
PFD	**P**rimary **F**light **D**isplay

Q3D	**Q**uasi **3-D**imensional
RANS	**R**eynolds-**a**veraged **N**avier-**S**tokes CFD
RMS	**R**oot-**M**ean **S**quared
SMT	**S**hear, **M**oment and **T**orque
SS	**S**ingle **S**lotted flap
SSF	**S**ingle **S**lotted **F**owler flap
TFTC	**T**hrust **S**pecific **F**uel **C**onsumption
TOFL	**T**ake–**o**ff **F**ield **L**ength
TS	**T**riple **S**lotted flap
TSF	**T**riple **S**lotted **F**owler flap
UD	**U**niform **D**esign
UJ	**U**niversal **J**oint
UoS	**U**niversity **o**f **S**outhampton
UVLM	**U**nsteady **V**ortex-**L**attice **M**ethod
VLM	**V**ortex-**L**attice **M**ethod

Physical Constants

Acceleration due to gravity	$g = 9.81\,\mathrm{m\,s^{-2}}$

List of Symbols

a	Local speed of sound	$\mathrm{m\,s^{-1}}$
AR	Wing aspect ratio	-
c	Chord length	m
C_D	Drag coefficient	-
$C_{D_{\mathrm{avg}}}$	Average drag coefficient	-
C_L	Lift coefficient	-
$C_{L,inv}$	Inviscid (VLM) lift coefficient	-
cC_L	Lift coefficient multiplied by local chord	-
C_{L_A}	Approach lift coefficient	-
$C_{L_{\mathrm{avg}}}$	Average lift coefficient	-
$C_{L_{max}}$	Maximum lift coefficient	-
$C_{L_{TO}}$	Lift coefficient when on the ground	-
$C_{L,vis}$	Viscous (RANS) lift coefficient	-
C_T	Thrust specific fuel consumption	-
f	Cost function	-
F_{airload}	Aerodynamic force	N
$h_{obstacle}$	Obstacle clearance height	m
k_{fle}	Leading edge scale factor	-
k_{tef}	Trailing edge scale factor	-
K_A	Net rolling aerodynamic drag coefficient	-
K_T	Net rolling thrust coefficient	-
L_{GR}	Ground roll distance	m
L_R	Rotate distance	m
L_{TC}	Transition to climb distance	m
L_{TO}	Total take-off distance	m
L_C	Obstacle clearance distance	m
n_{zw}	Load factor	-
N_{zw}	Ultimate load factor	-
$\boldsymbol{R}$	Flow residual	-
Re	Reynolds number	-
Re_{cr}	Critical Reynolds number	-
S_{flap}	Trailing edge flap area	$\mathrm{m^2}$
S_{slat}	Leading edge slat area	$\mathrm{m^2}$
S_{wing}	Wing area	$\mathrm{m^2}$
S_{csw}	Wing-mounted control surface area	$\mathrm{m^2}$
St	Strouhal number	-
t	Aerofoil thickness	m
T	Thrust	N
$\hat{T}$	RMS thrust	N
$\boldsymbol{U}$	FLow conservative variables	-
V_∞	Free-stream velocity	$\mathrm{m\,s^{-1}}$
V_1	Take-off decision speed	$\mathrm{m\,s^{-1}}$

V_2	Take-off obstacle clearance speed	$\mathrm{m\,s^{-1}}$
V_A	Approach velocity	$\mathrm{m\,s^{-1}}$
V_f	Average flare speed	$\mathrm{m\,s^{-1}}$
V_{fe}	Maximum flap deployment speed	$\mathrm{m\,s^{-1}}$
V_{MC}	Aircraft minimum control speed	$\mathrm{m\,s^{-1}}$
V_{MU}	Aircraft minimum unstick speed	$\mathrm{m\,s^{-1}}$
V_R	Rotate speed	$\mathrm{m\,s^{-1}}$
V_{SR}	Reference stall speed ($\cong V_{CLmax}$)	$\mathrm{m\,s^{-1}}$
V_{TD}	Touchdown speed	$\mathrm{m\,s^{-1}}$
V_{TO}	Aircraft airborne airspeed	$\mathrm{m\,s^{-1}}$
W	Aircraft weight	N
W_a	Aileron system weight	N
W_e	Empty aircraft weight	N
$W_{fix_{LE}}$	Weight of fixed leading edge structure	N
$W_{fix_{TE}}$	Weight of fixed leading edge structure	N
W_{flap}	Trailing edge high-lift device weight	N
W_i	Initial aircraft weight	N
W_{sec}	Aircraft secondary wing weight	N
W_{slat}	Leading edge high-lift device weight	N
W_S	Spoiler system weight	N
W_{TO}	Aircraft take-	N
W_{wing}	Aircraft wing weight	N
x_i	Design variable	-
$\boldsymbol{x}$	Design variable vector	-
α	Angle of attack	rad
γ	Climb angle	rad
γ_a	Approach angle	rad
Γ	Circulation	$\mathrm{rad\,s^{-1}}$
θ_s	Separation angle	$^\circ$
Λ	Wing sweep angle	rad
λ	Wing taper ratio at 20% MAC	-
ν	Relaxation factor	-

Chapter 1

Introduction

1.1 Aviation growth and environmental goals

For more than two decades up until early 2020, commercial aviation demonstrated almost uninterrupted growth. The Airbus Global Market Forecast Report 2017 identified a demand for 34,900 new aircraft of greater than 100 seat capacity by 2036 to replace old models and to satisfy new demand [4]. The COVID-19 pandemic of 2020-21 changed the short and medium-term picture dramatically. with "*...commercial aircraft business activity [dropping] by close to 40%... as the industry faces an unprecedented crisis. Commercial aircraft production rates have been adapted accordingly.*"[5]

Though an exceptionally challenging time for the commercial airline industry, the pandemic provides an opportunity to drastically reduce the carbon emmissions of the existing stock of aircraft as older, less fuel efficient aircraft are retired earlier than previously anticipated. The International Air Transport Association (IATA) has set three ambitious environmental goals [6]:

- An average improvement in fuel efficiency of 1.5% per year from 2009 to 2020.
- A cap on net aviation CO_2 emissions from 2020 (carbon-neutral growth).
- A reduction in net aviation CO_2 emissions of 50% by 2050, relative to 2005 levels.

Despite the pandemic, air travel is likely to rebound eventually and return to growth [7]. Decoupling emissions from passenger growth is an immense challenge, and requires a combination of improvements to operations and to aircraft design. A breakdown of the causes of aviation CO_2 emissions can be understood more clearly by means of a *split-tree*, whereby the 'children' of a particular cause are mutually exclusive and collectively exhaustive drivers of that cause.

The split-tree in Figure 1.1 shows that global aviation CO_2 (top level) depends only on the number of passenger miles flown and the CO_2 per passenger mile (Level 1) if air travel is not artifically constrained (for example by governement intervention). This means that reducing aviation CO_2 requires either a decrease in passenger miles flown (which, in free market economies, depends almost entirely on the cost per passenger mile) or a reduction in CO_2 per passenger mile. As discussed earlier, the number of passenger miles is only expected to increase in the long-term. Aviation emissions reduction must therefore come entirely from reducing the emissions per passenger mile.

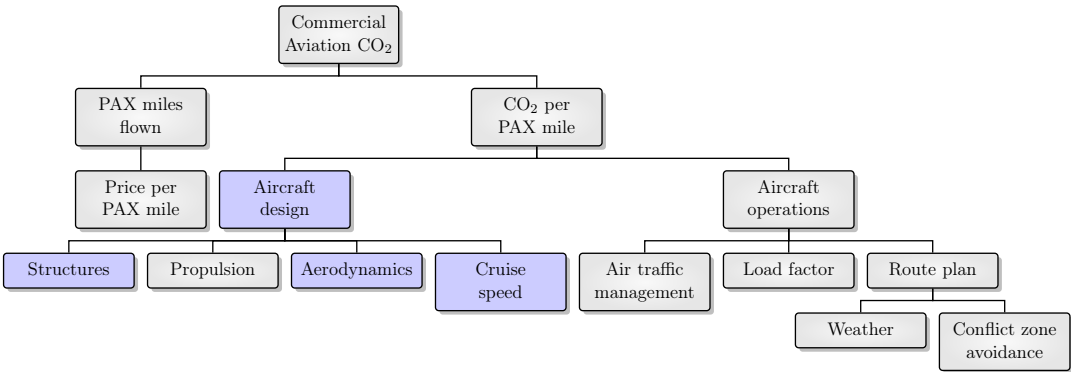

FIGURE 1.1: Breakdown of causes of commercial aviation CO_2 emissions. Light grey boxes are out of scope in this research project.

Aircraft operations and aircraft design are the two variables which impact the CO_2 per passenger mile. For the purposes of this research, aircraft operations will be considered an independent variable which should influence the aircraft design, rather than vice-versa.

The Airbus Global Market Forecast (GMF) report 2017 [4] revealed that more than 70% of new aircraft orders in the next 20 years will be for single–aisle aircraft, representing nearly half the total value of aircraft sales (Figure 1.2). A lot of attention is given to long-haul commercial aviation, with record-breaking direct flights such as the recent Perth–London route serviced by the Boeing 787 Dreamliner featuring in a number of news sources. Much less attention in both academia and in the media is given to the dominance of short-haul aviation, the majority of which is performed by single–aisle aircraft.

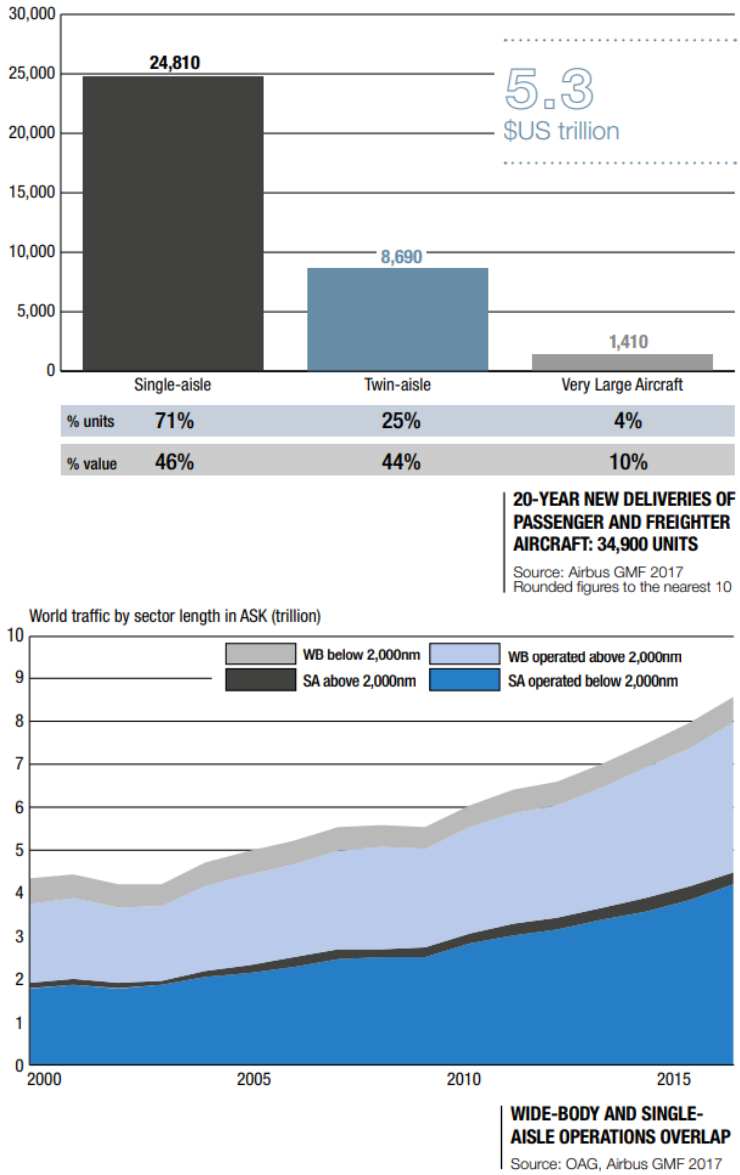

FIGURE 1.2: Graphs from the Airbus GMF 2017 showing the current and future dominance of narrow–bodied aircraft and short-haul flying [4].

The Airbus A320ceo/neo single-aisle aircraft dominates the order-book and (variant–dependent) has a range of up to 3500nm. Eurocontrol [8] defines short-haul routes as being less than 810 nmi, medium-haul as being between 810 nmi and 2160 nmi, and long–haul routes greater than 2160 nmi. Despite the A320 being comfortably able to perform long–haul flights, Figure 1.2 reveals that the overwhelming majority of single-aisle operations are less than 2000 nmi.

The most important aspects of aircraft design for CO_2 emissions are shown on the bottom level of Figure 1.1 and are found in the linearised Bréguet range equation in Eqn. 1.1. CO_2 emissions are directly proportional to the fuel burnt [9], and the disciplines identified in this equation are the principal foci of research and development in industry and academia.

$$W_{fuel} \simeq \underbrace{W_{ZF}}_{\text{Structures}} \times \underbrace{TSFC}_{\text{Propulsion}} \times \underbrace{\frac{D}{L}}_{\text{Aerodynamics}} \times \underbrace{\frac{1}{M}}_{\text{Cruise operating point}} \times \underbrace{\frac{R}{a}}_{\text{Air properties}} \tag{1.1}$$

These disciplines cannot be considered in isolation and interact strongly with each other when optimal designs are pursued.

As far as flight is concerned, it is perhaps unsurprising that the wing is the most crucial component. Civil jet aircraft operate in the transonic regime – cruising at between Mach 0.79 and 0.89, where the air is compressible and shock waves appear on the upper surface of the wing due to the locally supersonic flow [10]. A rapid increase in drag is seen above Mach 0.8, and a number of transonic drag reduction methodologies are used, most notably the use of swept–back wings and supercritical aerofoil sections. In describing the level of engineering that went into the 747 wing, Irving [11] wrote:

> *"Designing the wing involved literally thousands of decisions that could add up to an invaluable asset, a proprietary store of knowledge. A competitor could look at the wing, measure it even, and make a good guess about its internal structure. But a wing has as many invisible tricks built into its shape as a Savile Row suit; you would need to tear it apart and study every strand to figure out its secrets."*

1.2 Aircraft design considerations and challenges

Traditional industrial aircraft design proceeds through a series of maturity gates (MG) in which disciplines are treated as separate. For example, structures are optimised once the external aerodynamic shape is frozen. In this siloed approach, each discipline is developed with little or no interaction from the other multifaceted aspects of the design. In down–selecting the final aircraft concept, design parameters are tightened and addressed in ever increasing detail [12]. At MG 5, the concept is frozen, meaning the shape and structural layout are fixed and the aircraft target loads are set. MG 5 has the objective of anticipating the certification load values, and quantifying this data as target loads. Design target loads are the limiting loads that an aircraft or aircraft component must be designed to withstand. Sticking to development timelines means that it is critical to limit the risk in setting these target loads [13]. If flight tests reveal that the target loads are underestimated, expensive re–design is often required. If the target loads are instead overestimated, the aircraft will be heavier than needed with degraded performance.

In a typical product development program, approximately 90% of the cost of an aircraft type's development and production is committed by design decisions made in the first 10% of the design cycle [14]. The outsized influence on programme cost of the early design stages makes accurate assessment of the suitability and optimality of whole–aircraft concepts vital to the programme success. At Bombardier Aerospace, three 'levels' of fidelity are employed at the conceptual stage of aircraft design: 'Level 0', using knowledge–based tools; 'Level 1', incorporating mixed–fidelity physics–based aerodynamic and structural–analysis tools; and 'Level 2', using surrogate models constructed from high–fidelity simulations [12]. In Level 0, designers explore a large parameter space relying heavily on empirical and linear correlations to satisfy the

business case of a future platform [15]. Down–selection takes place in the subsequent levels, where the design parameters are progressively tightened and addressed in ever increasing detail using the higher–cost, higher–fidelity methods to converge on the final aircraft concept.

1.2.1 Computational fluid dynamics fidelity levels

Aircraft design necessarily makes use of computational fluid dynamics of various levels of fidelity and computational cost. Fluid flows are governed by three basic principals: conservation of mass, conservation of energy and conservation of momentum. The Navier–Stokes (N–S) equations represent the most accurate mathematical description that describe viscous, rotational and compressible flow [5].

Direct Numerical Simulation (DNS)

Direct solutions to the N–S equations, known as Direct Numerical Simulation (DNS), resolve all flow features and turbulent eddies at all length scales. The computational domain needs to be large enough to capture the largest flow features, and fine enough to resolve the smallest. The this ensures that the accompanying computational cost is prohibitive for almost all applications outside of turbulence research. At current rates of improvement of computational capability, DNS might be ready for widespread commercial applications by 2080 [16]. DNS solves the N–S equations for viscous, unsteady, rotational, compressible flow at all turbulent length scales.

Large Eddy Simulation

Large Eddy Simulations (LES) use semi-empirical turbulence models to approximate the smaller, less energetic, sub-grid length scales, while resolving the large eddies that are most influenced by the geometry of the problem. This trade–off reduces the computational cost with little reduction in accuracy of the numerical solution. However, LES is still far too computationally expensive for most engineering design problems, though Spalart expects that LES will become a useful industrial tool in 2045 – 35 years earlier than DNS. LES solves the N–S equations for viscous, unsteady, rotational, compressible flow at the largest, most relevant length scales.

Reynolds–Averaged Navier–Stokes Equations

Solutions to the Reynolds–Averaged Navier–Stokes equations are the highest level of fidelity that has widespread utility within aeronautical engineering. RANS equations are derived by time–averaging the flow into mean and time–dependent components in a process known as the Reynolds decomposition. The mean part of the flow is numerically solved and is of most interest to engineers. The fluctuating, time–dependent part becomes zero when time-averaged [17] and is substituted for closure coefficients which model the non-linear convective acceleration term (the Reynolds Stress) as a function of mean flow only. The turbulence models available that close these RANS equations are semi-empirical in nature and provide a turbulent viscosity to describe the value of the Reynolds stresses.

Related to the steady RANS solutions is Unsteady RANS (URANS). This has the advantage of being able to capture transient flow phenomena not possible with steady RANS solutions. Whereas steady RANS takes time-averages over an entire time interval, URANS performs time averaging over a single time step only. The author contributed to a published study on numerical errors in URANS flows in [18].

RANS solves the N–S equations for viscous, rotational, compressible flow with time-averaged turbulence.

Euler Equations

When viscosity is neglected, the Navier–Stokes Equations simplify to the Euler equations. These are generally a good approximation for the flow regime outside of the boundary layer.

Solutions to the Euler equations are valid for inviscid, rotational, compressible flow.

Laplace's Equations

While higher fidelity flows based on the N–S equations are non–linear, if Euler's Equation is simplified by assuming incomprehensibility (reasonable for flows where $M_\infty < 0.3$), the resulting potential flow equation reduces to a linear partial differential equation known as Laplace's equation. Laplace's equation has exact solutions and is valid for inviscid, irrotational, incompressible flow.

1.2.2 Solution methods

Non-linear solution methods

Non-linear solution methods are applied to the non-linear flow models such as RANS and Euler. These are usually the Finite Difference Method (FDM), the Finite Element Method (FEM), and the Finite Volume Method (FVM). The latter is most commonly applied to RANS and Euler solvers in part due to its numerical similarity to the actual physical phenomena. The two flow solvers used for the RANS solutions in this work are DLR-Tau and SU2. Both are finite volume solvers [19] [20].

Linear solution methods

As Laplace's Equation is linear, well–known simpler flows can be superimposed to find solutions to more complex ones. Four types of basic solution exist: uniform flow, source flow, doublet flow, vortex flow [21]. Of these, only vortex flow creates lift and multiple solution methods exist for vortex-induced lift including lifting line theory (LLT), the vortex lattice method (VLM) and panel methods. The vortex lattice method is used extensively for the low–cost loads estimation method introduced in Chapter 5 and involves modeling the lifting surfaces as an infinitely thin sheet of discrete vortex ring elements. This allows computation of the lift and induced drag while the effect of thickness and viscosity is neglected [22]. The VLM is discussed further in Section 5.1.2.

Summary

Aircraft design increasingly makes use of 3D Computational Fluid Dynamics simulations to replace and complement wind–tunnel tests. CFD allows many more configurations to be tested and can model full–scale aircraft in almost any conceivable flow condition, but is still limited by available computing power. Historically, the holy grail of CFD has been to solve the Navier–Stokes equations, but with no analytical solution for most realistic flow regimes, approximations or simplifications, such as those described earlier, must be sought. The CFD used for analyses in this research is of two main types with two different fidelity levels:

1. RANS models, which are are used extensively in industry and academia for high–fidelity modelling of all flight phases.

2. The Vortex–Lattice Method which are employed extensively in the early exploratory and conceptual Ddesign phases of aircraft development because of the low computational cost compared to 3D RANS [12].

1.2.3 Shortcomings of modern MDO

In contrast to the traditional approach to aircraft design outlined in Section 1.2, contemporary aircraft design has seen a trend towards a concurrent approach where aircraft are optimised through a multi–disciplinary optimal strategy. Modern computational capabilities have made it possible to increase the fidelity of some aspects of the conceptual design phase by using high–fidelity RANS CFD simulations and automatic optimisation techniques. Gradient–based optimisation of wing sections and planforms can produce superior lift and drag characteristics for a given operating point (or points) compared to a baseline design [23]. As thinner wings will generally have lower induced drag for a given shape and wetted area, shape optimisation of wing sections needs to be constrained in thickness and/or volume to prevent unrealistically thin sections from being produced [24].

High–fidelity estimates are often restricted to purely aerostructural considerations [25]. These two disciplines are certainly the most tightly–coupled and important for wing optimisation and offer a clear benefit over the traditional approaches, but the two disciplines involved are not exhaustive. For example, the design and optimisation of the high–lift system is not one which generally occurs in the conceptual design phase, unless the field performance requirement of the aircraft is particularly non–standard. As well as being vital for the take–off and landing stages, the high–lift system accounts for up to 11% of the production cost of a typical jet transport aircraft [26]. High–lift design and optimisation is typically left to the end of the design stage, when much of the aircraft geometry has already been committed [27].

1.2.4 Wing weight and aeroelastic considerations

The wing weight can be broken down into two categories: load-bearing structural (or primary) wing weight, and non-load-bearing (or secondary) wing weight. Wings have the single largest impact on aircraft aerodynamic performance; they are the primary lifting surfaces and a contain the a significant quantity of load-bearing structure. They therefore make a considerable impact on aircraft all-up weight, contributing approximately one third of the aircraft dry mass [28]. The Airbus A320 wing structure weighs over 18,000kg [29] and has an all-up operating empty weight (OEW) of 39,500kg [30]. High–fidelity coupled aerostructural optimisation such as in [24] optimises the aerodynamic design of the wing and their internal structure concurrently. Coupling aerodynamics and structural models to compute the static aeroelastic shape of aircraft wings is essential when designing flexible wings [31] and is particularly important for swept wings, where bending-twist coupling can result in large changes in the twist distribution [32]. This approach is extremely effective at optimising the combined aerodynamic shape and load–bearing structure for a wing, particularly for a single-point optimisation cruise configuration when subject to constraints such as minimum payload and minimum range.

Load-bearing structural weight and cruise aerodynamics are tightly–coupled and extremely important for wing design, but the whole–wing weight estimation is still needed to make an accurate estimate of the structural contribution to the induced

drag of the aircraft (and therefore design objectives such as reducing mission fuel burn). Although the load-bearing structural weight can be estimated to a high degree of precision within a coupled aerostructural optimisation, total wing weight does not enjoy the same level of fidelity [25]. Within a conceptual aerostructural optimisation of a cruise wing, total wing weight estimation is usually performed using one of several empirical correlations that either extrapolate total wing weight from the FEM wing weight and the final wing area [33], or from the geometric parameters of the selected wing design [34].

While the mass distribution of the wing causes a significant effect on the dynamic properties of a structure, it is typically considered less during initial design efforts, with harmful unforeseen dynamics discovered later in the design process overcome through mass distribution alterations [35]. Knowledge of the high–lift actuation system mass and distribution could therefore allow for more precise aeroelastic tailoring in the early phases of designs (design work before MG 5). Aeroelastic tailoring involves controlling the directional stiffness of an aircraft structural design to achieve light weight airframe designs [36], and is an example of passive aeroelastic control [37].

The high-resolution knowledge of primary structural weight contrasts strongly with the low-resolution knowledge of the contribution of the secondary wing weight typical early in the design cycle. There is therefore a fidelity–inconsistency between the calculation of primary (load–bearing) wing weight and secondary (non–load–bearing) wing weight. This has two important consequences which form one of the motivations of this research:

1. While the wing aerodynamic and structural optimality can be known to a high degree of precision, the additional non–structural weight of the wing contains considerably more uncertainty than the load–bearing structure. This is because design parameters which affect the secondary wing weight are often made after the design freeze of the wing planform and shape [38]. For example, the high-lift actuation system - a key focus of this work, is not designed and sized until well into the aircraft development timeline and not until after the primary structural design has been finalised. The uncertainty in secondary wing weight in the early phases is carried forward to the total wing weight, meaning that payload and fuel margins must be larger to account for this uncertainty.

2. By extrapolating the secondary wing weight from the load–bearing weight of the wing, the weight of components such as the control surfaces, actuation systems, fixed leading and trailing edge surfaces and high–lift panels are prevented from informing the optimiser and being traded off against the other design parameters.

As major engineering rework is often caused by systems integration challenges and changing economic requirements [12], an MDO capability that provides high fidelity in a small number of disciplines, or without sufficient consideration for constraints of off–design cases that typically drive the design, is in reality a low fidelity model at the system level. One of the requirements for improving the state–of–the art in MDO, therefore, is to increase the number of disciplines involved in the optimisation and constraint formulation, and/or to increase the fidelity of the modelling of the disciplines which already included in the optimisation.

A significant contribution to the non–structural mass distribution within the wing is made by the high–lift geared rotary actuators (GRAs) [39], [40]. These reduction gearboxes turn high RPM rotation from hydraulic motors into high torque rotation that is used to deploy the flaps and the slats. These dense GRAs are small fractions

of a metre in any dimension, and are therefore small enough to be considered lumped masses from an aeroelastic analysis perspective. Every slat and flap panel has two, with the largest and heaviest being in the the trailing edge (TE) of each wing due to the torque demand of the large trailing edge flap panels. The sizes of these masses can be estimated from knowledge of the torque required of them and from industrial data which sizes the actuators.

1.3 Research aims and objectives

It is the prospect of reducing the uncertainty in dynamic aeroelasticity and aircraft sizing that has motivated this study. In [1], a low–cost actuation mass estimation method was presented, which used industrial data to correlate rated output torque with mass for high–lift GRAs. This method was used to estimate the mass of the high–lift actuation system including the GRAs in the high–lift configuration of the NASA Common Research Model (CRM), an open source model of a representative wide–bodied jet airliner. Herein, a methodology for increasing the fidelity of the mass estimate of the high-lift actuation system, a major contributor to secondary wing weight, is presented. We also develop tools for undertaking this using low cost CFD methods. Finally, the implications of being able to quantify the actuation system mass and distribution in early–phase aircraft design is demonstrated. These three areas of focus are summarised below and in Figure 1.3.

1. 'What': Demonstrating the ability to make a priori estimates of the high-lift actuation weight using industrial actuation data and high–lift actuation design requirements.

2. 'How': Development of novel low cost methods to estimate the high-lift surface hinge moments that are used to facilitate actuation mass estimates.

3. 'Why': Using the high–lift actuation weight estimation to quantify its impact on the dynamic aeroelastic response of an airliner wing.

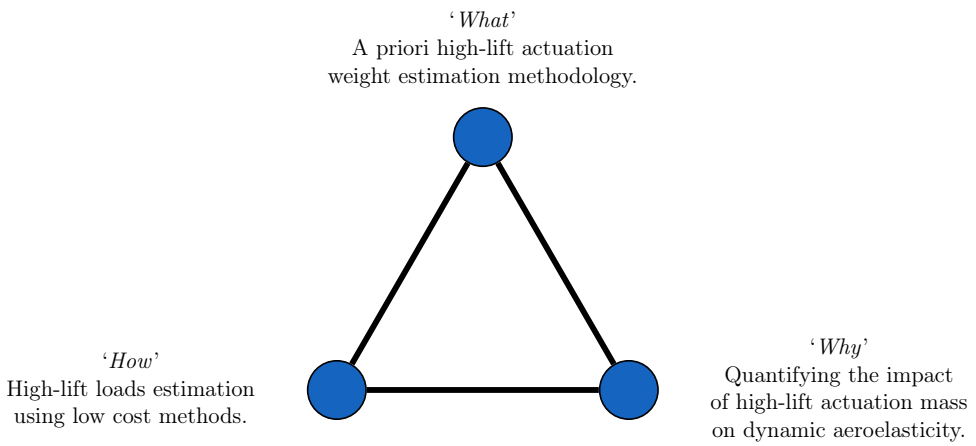

FIGURE 1.3: The three main areas of focus.

These three areas are the topics of Chapters 3, 5, and 6 respectively. Chapter 4 on robust multi–element aerofoil meshing supports the work in Chapter 5. The limitations and future work are detailed in Chapter 7.

Chapter 2

Literature Review

2.1 Overview of secondary wing weight and its estimation

2.1.1 Existing Methods

In order to reduce the uncertainty inherent in selecting the optimal configuration for a high-lift wing, an accurate assessment of the wing weight, W_{wing}, needs to be made. An attempt to attribute the secondary weights of the wing to individual factors was made by Torenbeek [41] in 1992. These simple equations, and accompanying categorisation of flap systems, approximate a relationship between the take–off weight of an aircraft and the secondary wing weight, based on empirical data for aircraft that were already in service. He identified six major contributions to the secondary weight, W_{sec}, which are summarised in Table 2.1.

Symbol	Description
$W_{fix_{LE}}$	Fixed leading edge structure
$W_{fix_{TE}}$	Fixed trailing edge structure
W_{slat}	Leading edge high-lift devices (excluding actuation)
W_{flap}	Trailing edge high-lift devices (excluding actuation)
W_S	Spoilers
W_a	Ailerons

TABLE 2.1: Wing secondary weight components.

Where

$$W_{sec} = W_{fix_{LE}} + W_{fix_{TE}} + W_{slat} + W_{flap} + W_S + W_a \tag{2.1}$$

and these contributions are identified in the diagram of a typical wing inf Figure 2.1.

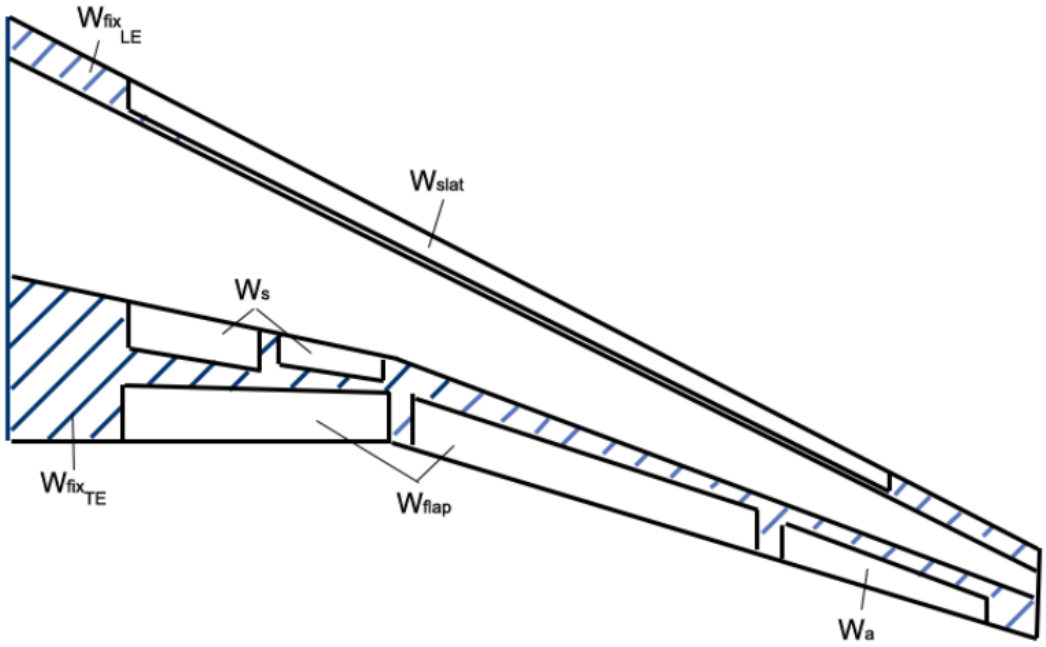

FIGURE 2.1: Contributions to secondary wing weight [42].

The equations given by Torenbreek for each of these contributions is given in 2.2 (all values in Newtons). The areas of the relevant sections, S_{fix}, S_{slat} and S_{flap} are in m^2.

$$W_{fix_{LE}} = 75 S_{fix_{LE}} k_{fle} \left(1 + 1.6\sqrt{W_{TO}/10^6}\right) \tag{2.2a}$$

$$W_{fix_{TE}} = 60 S_{fix_{TE}} \left(1 + 1.6\sqrt{W_{TO}/10^6}\right) + S_{fix_{TE}} \Delta \tag{2.2b}$$

$$W_{slat} = 160 S_{slat} \left(1 + 0.7\sqrt{W_{TO}/10^6}\right) \tag{2.2c}$$

$$W_{flap} = 100 S_{flap} k_{tef} \left(1 + \sqrt{W_{TO}/10^6}\right) \tag{2.2d}$$

The factor k_{fle} accounts for the strengthening of the leading edge structure to support movable Krüger flaps such that:

$k_{fle} = 1.0$ when no leading edge devices are present.

$k_{fle} = 1.4$ with leading edge devices.

The trailing edge scaling factors k_{tef} and correction Δ (from Eqn. 2.2b) are

The type of flaps are given as single, dual or triple–slotted (SS, DS, TS), and the same architectures with Fowler motion (SSF, DSF, TSF). The advantage of these equations is their simplicity and their ability to account for the different trailing edge flap types in Table 2.2. However, no account is taken for the considerable weight of the actuation devices – whose mass depends strongly on the torque demanded by the aerodynamics – though Rudolph [26] does provide some linear relationships between panel area and actuation weight.

Since these linear statistical relationship models were established in the early-mid 1990s, there has also been a strong trend by both Airbus and Boeing towards the simplification of the high-lift system. Single–element trailing edge devices now

Type	Δ	k_{tef}	Comment on k_{tef}
SS	0	1.0	Add 20% for auxiliary t.e. flap
DS	45	1.5	Fixed front vane
		2.0	Variable geometry
TS	105	2.4	Variable geometry
SSF	0	1.8	Add 20% for auxiliary t.e. flap
DSF	45	2.5	Fixed front vane
TSF	105	2.9	Variable geometry

TABLE 2.2: Scaling factors for trailing edge flaps.

dominate newer aircraft models (Figure 2.2) due to the considerable cost and weight advantages that come with achieving the aerodynamic requirements with a single flap. There is no evidence of this trend reversing, and new variants of the same type (eg. 747-800) have seen simplifications of their trailing edge systems compared to the older versions.

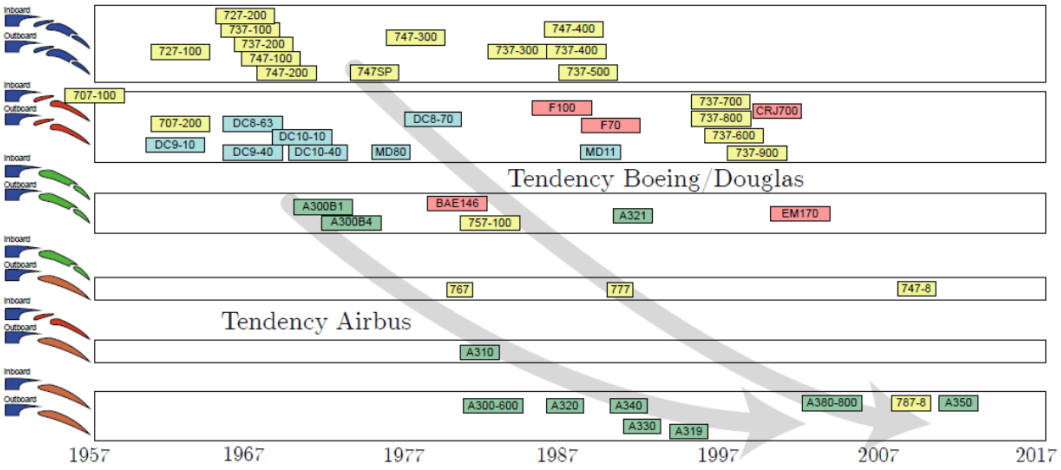

FIGURE 2.2: Trend in trailing edge device complexity [42] [43].

Another relation for airliner wing weight was produced by Leoviriyakit, Kim and Jameson [34] and estimates the total wing weight from just the wing design parameters:

$$W_{wing} = 0.0051 \left(W_{TO} N_{zw}\right)^{0.557} S_{wing}^{0.649} AR^{0.5} \left(t/c\right)_{root} \left(1+\lambda\right)^{0.1} \cos\left(\Lambda\right)^{-1} S_{csw}^{0.1} \quad (2.3)$$

Where N_z is ultimate load factor, equal to 1.5 times the limit load factor, AR is wing the aspect ratio, λ is the wing taper ratio, Λ is the sweep angle, and S_{csw} is the area of the wing–mounted control surfaces. $(t/c)_{root}$ is the aerofoil thickness–to–chord ratio at the wing root.

More recently, weight estimation in optimising appears to have become more crude as high-fidelity minimising load-bearing structural weight has been a key focus of optimisation efforts. Kennedy and Martins [33] performed a weight breakdown using preliminary weight estimation techniques. These were based on a combination of statistical correlations and finite–element models of the wing and horizontal tail. The relationship they used is expressed in Equation 2.4:

$$W_{wing}\ (kg) = 1.5W_{wing}^{(FE)} + 15S_{wing} \tag{2.4}$$

$1.5W_{wing}^{(FE)}$ is the finite–element mass (in kg) of the full wing and is scaled by a factor of 1.5 to account for additional mass from components and fasteners not present in the FE model. The secondary mass of the wing comes from a combination of high-lift devices, their associated structures and actuation, the spoilers and the ailerons (see Table 2.1). The term $15S_{wing}$ is a crude estimate of this secondary weight that assumes the secondary wing weight scales linearly with the wing area, S_{wing}. The constant of proportionality, 15, implicitely has units of $kg\ m^{-2}$.

2.1.2 High-lift system weight contribution

The high-lift system makes the largest single contribution to the secondary wing weight [40]. Accurate calculation of the weight of the high-lift system will reduce the uncertainty of the secondary wing weight and allow a more fidelity–consistent estimate for the total wing weight when using high–fidelity conceptual design tools as outlined previously. An approximate breakdown of the high-lift system weight is shown in Table 2.3.

Flap/slat panel weight	Support & mechanisms	Actuation	Fairings
30%	35%	25%	10%

Table 2.3: Approximate weight breakdown of high-lift system[40].

Torenbeek categorised flap systems of different areas and produced approximate relationships between the take–off weight of an aircraft and the secondary wing weight, based on empirical data from existing aircraft [41] while Raymer's contemporary text on aircraft conceptual design [44] uses statistical weight estimation equations that are up to 50 years old [45][46]. This is discussed further in Section 2.1, but as these estimates are based only on simple equations that relate aircraft MTOW and panel area, there is a significant opportunity to improve them at little additional cost using input from the aerodynamic and geometric models of aircraft concepts.

2.2 High-lift system design

One candidate for the next discipline for inclusion in any MDO formulation is the high-lift system. The design and optimisation of the high-lift system is not one which generally occurs in the conceptual design phase, unless the field performance requirement of the aircraft is particularly non–standard. As well as being vital for the take–off and landing stages, the high-lift system accounts for up to 11% of the production cost of a typical jet transport aircraft [26]. High-lift design and optimisation is typically left to the end of the design stage, when much of the aircraft geometry has already been committed [27]. Research published by Kieboom and Elham [47] shows just how different a combined high-lift/cruise optimised wing can be to one optimised in the traditional sequential fashion using the same methods. The importance of the high-lift system on a generic wide–body twin–engined aircraft (such as the Beoing 777 or Airbus A330) was presented by Meredith [48]:

- An increase in maximum lift coefficient of 1.0% translates into an increase in payload of 22 passengers or 2000kg for a fixed approach speed on landing.
- An improvement in lift-to-drag ratio of 1.0% during takeoff allows for a 1300kg payload increase, or 14 additional passengers for a given range.
- A shift of $\Delta C_L = 0.10$ of the lift curve in the linear range results in a 1° reduction in attitude for a given glide slope angle. This allows a reduction in required landing gear height of 0.36m for a given tail strike attitude angle and a decrease in OEW of 630kg.

In recent years, there has been a strong trend by both Airbus and Boeing towards the simplification of the high-lift system in terms of the number of trailing–edge elements. Single–element trailing–edge devices now dominate newer aircraft models (Figure 2.2) due to the considerable cost and weight advantages that come with achieving satisfactory aerodynamic requirements with a just one flap element.

Historically, the conceptual design of the high-lift system has been an extremely manual one. Figure 2.3 shows the high-lift design process at Airbus as described by Flaig in 1993 [49]. Much of the effort involved comes from building up an aerodynamic database from wind tunnel tests and CFD to estimate the field performance of the aircraft being evaluated.

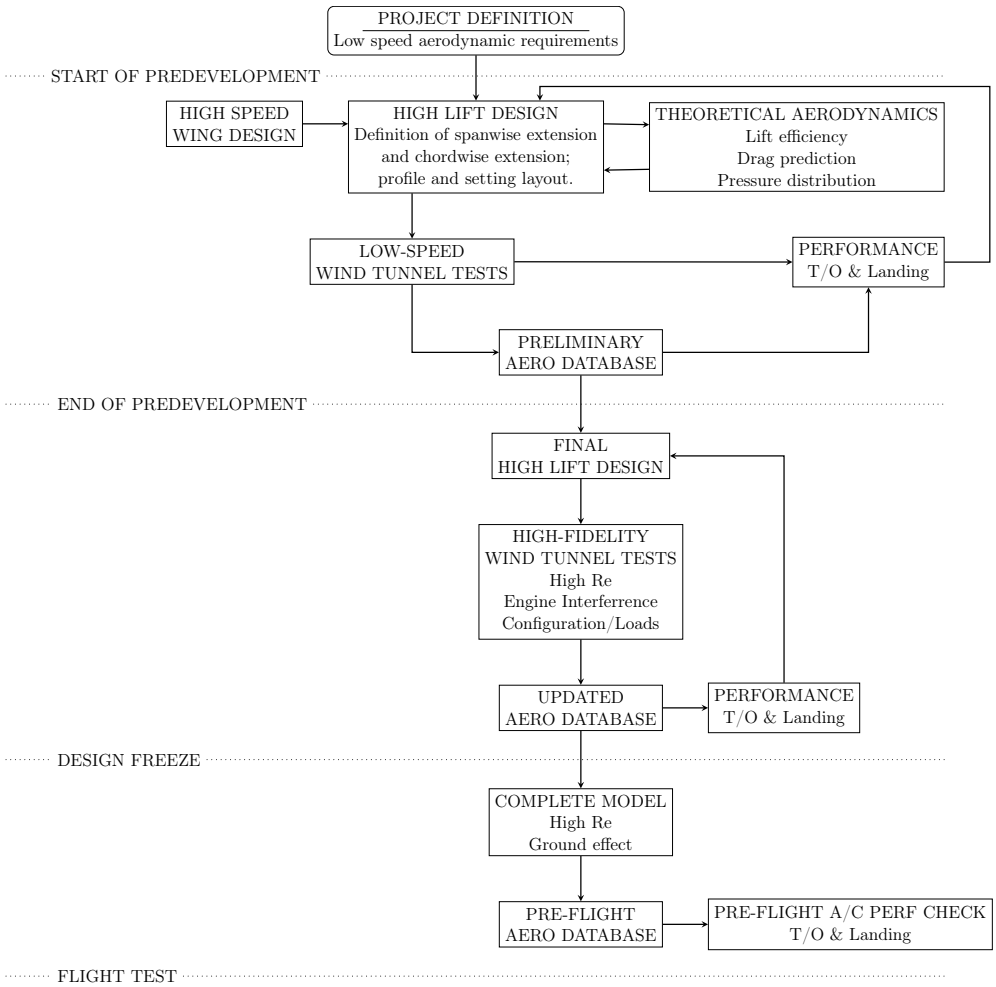

FIGURE 2.3: Airbus high-lift design process (1993) [49].

The next subsections outline the demands on the high-lift system from an aerodynamics perspective, and the way in which systems considerations affect the aircraft.

2.2.1 Aerodynamics

High-lift systems exist primarily to reduce the stall speed of an aircraft so that it can land slowly enough for standard undercarriage designs to withstand. At the same time, higher cruise speeds are achieved by reducing wing drag and fuel consumption using a combination of swept wings and higher wing loadings [44].

In general, deploying trailing edge devices cause an upward shift of the lift curve so that at the same angle of attack, a higher lift coefficient may be achieved. Leading edge devices do not generate more lift at the same angle of attack, but postpone flow separation. This allows for a higher usable angle of attack and also a higher maximum lift coefficient. Figure 2.4 shows the effect high-lift devices have on the aerodynamic characteristics and some of the common flap and slat configurations.

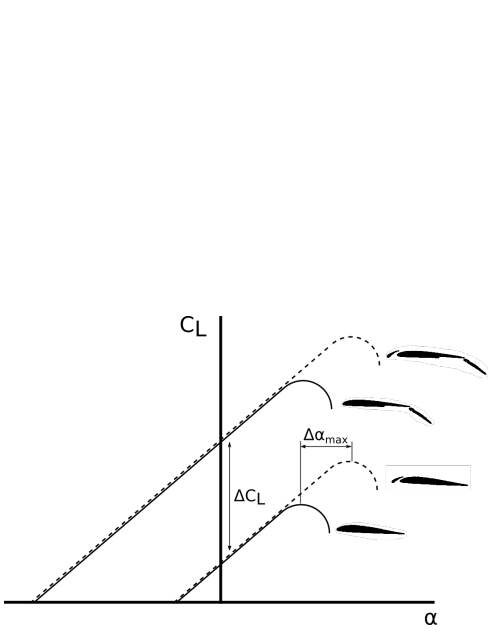

(A) Effect of flaps and slats on aircraft lift [50].

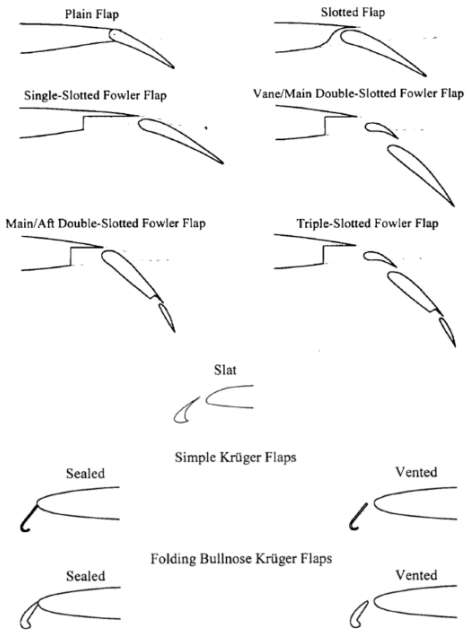

(B) Types of flaps and slats [51].

FIGURE 2.4: Flaps and slats and their simplified effect on the aerodynamics.

As Eq. 2.5 shows, for a fixed wing loading $\frac{W}{S_{wing}}$, C_L needs to be higher during the low-speed take–off and landing phase, than during the high-speed cruise phase.

$$C_L = \frac{1}{\frac{1}{2}\rho V_\infty^2}\left(\frac{W}{S_w}\right) \tag{2.5}$$

Van Dam [50] explained the requirement for high-lift devices by comparing two hypothetical aircraft designs, A and B (both without high-lift devices). One was optimised for cruise, and the other for take–off and landing. Each is governed by the well–know Bréguet range equation.

$$R = a\frac{M_\infty}{C_T}\frac{L}{D}\ln\frac{W_i}{W_e} \tag{2.6}$$

The term $M_\infty \frac{L}{D}$ is referred to by Torenbeek [52] as the range parameter because, for any transonic aircraft, this value needs to be maximised during the cruise phases to achieve the best range [53]. Indeed, as fuel is burnt in cruise and their lift requirement reduces, flight profiles keep this range parameter near the optimum by climbing in stages. Figure 2.5 shows a graph of range parameter against C_L at various Mach numbers for a Boeing 747-400.

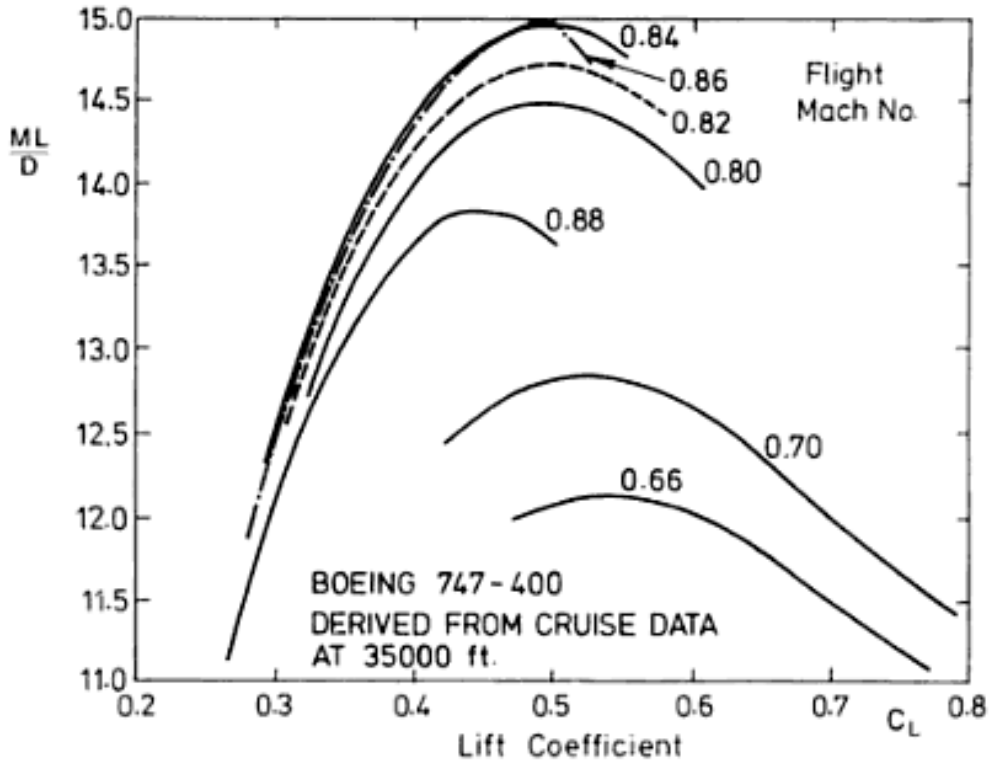

FIGURE 2.5: Range parameter against C_L at various Mach numbers for a Boeing 747-400 [53].

Table 2.4 summarises these results. Aircraft A, optimised for cruise, has a cruise C_L of 0.52 which gives the best range parameter of 14.4. To satisfy the airworthiness requirements for approach, Aircraft A requires $C_{L_{max}} = 2.34$, which lies far outside the capabilities of a simple swept wing without high-lift devices.

Conversely, Aircraft B, optimised for take–off and landing performance performs much more poorly at cruise. Assuming identical drag characteristics, $M_\infty \frac{L}{D} = 11.8$, equating to an 18.3% reduction in cruise efficiency. An aircraft with high-lift devices can, to a large extent, be both of these aircraft.

In order to be able to design and optimise the aerodynamics of a high-lift wing, the requirements that dictate the design of high-lift devices need to be understood. Flaig [49] identified these as:

- Approach speed – reducing this reduces the landing field length and alleviates stresses on the aircraft structure during landing.
- Take–off field length – reducing this reduces the total distance required to accelerate along the ground to lift-off speed, V_{LOF}.
- Climb rate – minimum climb rates, γ, are specified for initial climb and baulked landing, and in the case of one-engine inoperative (OEI).

	Aircraft A (cruise)	Aircraft B (T/O & Landing)
M_∞	0.8	0.8
V_A	145 knots	145 knots
C_L	0.52	0.27
C_{L_A}	1.55	0.79
$C_{L_{max}}$	2.34	1.2
$M_\infty \frac{L}{D}$	14.4	11.8
$\frac{W_{TO}}{S}$	7040 N/m^2	3600 N/m^2
$\frac{W_{Landing}}{S}$	5300 N/m^2	2700 N/m^2

TABLE 2.4: Comparison of two aircraft: one optimised for cruise, and the other for take–off and landing [50].

Take–off

Starting from the aircraft reference stall speed in the take–off configuration, V_{SR}, and the minimum unstick speed, V_{MU}, Section 25.107 of the EASA CERTIFICATION SPECIFICATIONS FOR LARGE AEROPLANES [54] specify the constraints relevant to take–off airspeeds (for two-engine aircraft) summarised in Table 2.5.

Speed	Definition	Constraint
V_{SR}	Reference stall speed in landing configuration	$V_{SR} \geqslant V_{CL_{max}}/\sqrt{n_{zw}}$
V_{MC}	Minimum control speed	$V_{MC} \leqslant 1.13 V_{SR}$
V_1	Critical take–off airspeed	$V_1 \geqslant 1.13 V_{SR}$
V_R	Rotate speed	$V_R \geqslant V_1$, $V_R \geqslant 1.1 V_{MU}$
V_{TO}	Lift-off speed of the aircraft	$V_{TO} \geqslant V_R$
V_2	Airspeed at which aircraft clears 35ft obstacle	$V_2 \geqslant V_1$, $V_2 \geqslant 1.1 V_{MC}$
γ	Climb angle	$\tan\gamma \geqslant 0.024$

TABLE 2.5: Relevant take–off speeds and constraints [54].

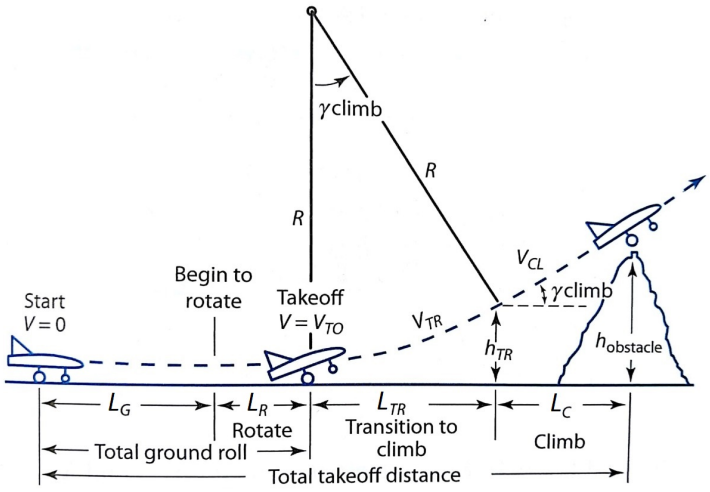

FIGURE 2.6: Diagram showing relevant take–off airspeeds [44].

The high-lift system at take–off is mainly driven by minimising the distance required to clear an 11m obstacle, known as *take–off field length* (TOFL). It consists

ground roll, rotation, transition and climbing distance, all of which must be reduced to improve this aspect of the field performance:

$$L_{TO} = L_{GR} + L_R + L_{TR} + L_C \tag{2.7}$$

where the ground run distance, L_{GR}, assuming the initial velocity is 0. L_{GR} is given by: [44]

$$L_{GR} = \frac{1}{2gK_A} \ln\left(\frac{K_T + K_A V_R^2}{K_T}\right) \tag{2.8}$$

Coefficients K_A and K_T are given by Eqns. 2.9 and 2.10:

$$K_T = \frac{\hat{T}}{W} - \mu_r \tag{2.9}$$

$$K_A = \frac{\rho}{2(W/S)}(\mu_r C_{L_{TO}} - D_{aero}) \tag{2.10}$$

The average thrust during ground roll, $\hat{T}$, is taken to be equal to the thrust at $V = 1/\sqrt{2}V_R$ and the rolling friction coefficient, μ_r, is assumed to be 0.03. The lift coefficient, $C_{L_{TO}}$ is based on when the aircraft is on the ground. Weight, $W = 1/2\rho S C_{L_{max}} V_{SR}^2$, is the MTOW and ρ is the air density at sea-level, 1.125kg/m^3. Since the rotation time from V_R to the lift–off attitude can be assumed to be ≈ 3 seconds for large aircraft, $L_R = V_R \cdot 3s = 1.1V_{SR} \cdot 3s = 3.3V_{SR}$.

During transition from V_R to V_{TO}, the aircraft accelerates from $1.13V_{SR}$ to $1.23V_{SR}$, giving an average speed during transition of $1.18V_{SR}$. Assuming this value of V_{TR} and an average lift coefficient during transition of about 90%, the vertical load factor, n, can be found:

$$n = \frac{L}{W} = \frac{\frac{1}{2}\rho S\,(0.9\,C_{L_{max}})\,(1.18\,V_{SR})^2}{\frac{1}{2}\rho S C_{Lmax} V_{SR}} = 1.25 \tag{2.11}$$

During transition, n must be equal 1.0 plus the centripetal acceleration:

$$n = 1.0 + \frac{V_{TR}^2}{Rg} = 1.25 \tag{2.12}$$

Giving a value for the transition radius, R, of:

$$R = \frac{V_{TR}^2}{g(n-1)} = \frac{V_{TR}^2}{0.25\,g} = 0.56\,V_{SR}^2 \tag{2.13}$$

The climb gradient, $\tan\gamma$ is stipulated to be 2.4% for two-engined aircraft with one engine inoperable. γ depends on the thrust-to-weight ratio and the lift-to-drag ratio: [50]

$$\sin\gamma \cong \frac{T}{W} - \frac{1}{L/D}\bigg|_{1.23V_{SR}} \tag{2.14}$$

The transition length, L_{TR} is given by:

$$L_{TR} = R\sin\gamma = R\left(\frac{T-D}{W}\right) \cong 0.56V_{SR}^2\left(\frac{T}{W} - \frac{1}{L/D}\right) \tag{2.15}$$

And the height climbed by the end of the transition, h_{TR}, is

$$h_{TR} = R\,(1 - \cos\gamma) \tag{2.16}$$

Finally, the horizontal clearance distance, L_c is given by:

$$L_c = \frac{11 - h_{tr}}{\tan\gamma} \tag{2.17}$$

The constant 11 is the obstacle height in metres civil aircraft must clear in accordance with CS 25.113(a)(1) [54] and is considered the end of the take–off length. If the obstacle is cleared during transition, $L_{TR} = \sqrt{R^2 - (R - h_{TR})^2}$ and $L_c = 0$. Putting all this together into Eq. 2.7, gives:

$$\begin{aligned} L_{TO} = & \frac{1}{2g\left(\frac{\rho}{2(W/S)}(\mu_r C_{L_{TO}} - D_{aero})\right)} \\ & \times \ln\left(\frac{\left(\frac{\hat{T}}{W} - \mu_r\right) + \left(\frac{\rho}{2(W/S)}(\mu_r C_{L_{TO}} - D_{aero})\right) 1.28\, V_{SR}^2}{\left(\frac{\hat{T}}{W} - \mu_r\right)}\right) \\ & + 3.3 V_{SR} \;+\; 0.56 V_{SR}^2 \left(\frac{T}{W} - \frac{1}{L/D}\right) \;+\; \frac{11 - h_{tr}}{\tan\gamma} \end{aligned} \tag{2.18}$$

Higher flap settings generally decrease L_{GR} distance but decrease L/D, reducing the climb performance. The aerodynamic design of the take–off configuration therefore involves a compromise between lift and drag.

Landing

Starting from the aircraft reference stall speed in the landing configuration (the full–flap stall speed), V_{S0}, Section 25.125 of the EASA Certification Specifications for Large Aeroplanes [54] and Raymer [44] specify the constraints relevant landing airspeeds for two–engine aircraft, summarised in Table 2.6.

Speed	Definition	Constraint
V_{S0}	Stall speed in landing configuration	$V_{SR} \geqslant V_{CL_{max}}/\sqrt{n_{zw}}$
V_a	Approach speed	$V_a \leqslant 1.23\, V_{SR}$
V_f	Average flare speed	$V_f \approx 1.19\, V_{SR}$
V_{TD}	Touchdown speed	$V_{TD} \geqslant 1.15\, V_{SR}$
γ_a	Approach angle	$\gamma \leqslant 3°$

Table 2.6: Relevant landing speeds and constraints [44] [54].

The load factor, n, can once again be taken as 1.25, and the friction coefficient, μ_r is ten times higher than during take off due to braking. It usually takes 1 to 3 seconds for the pilot to apply the brakes. The obstacle clearance height, $h_{obstacle} = 15$m.

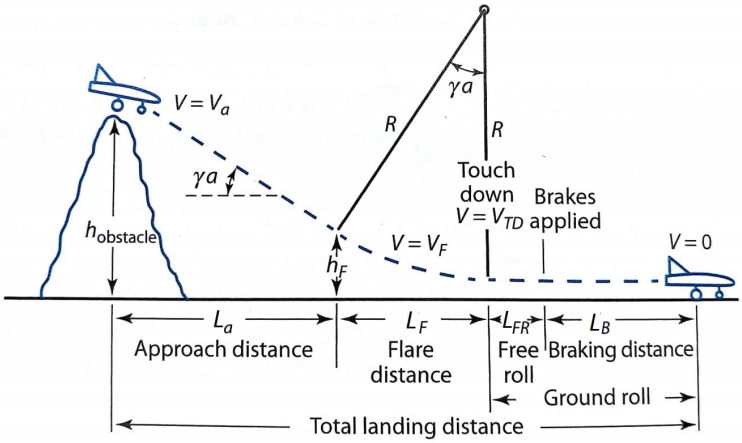

FIGURE 2.7: Diagram showing landing procedure [44].

The landing follows a similar analysis to that outlined for the take–off, but with the speeds and approach angles from Table 2.6.

2.2.2 High-lift Actuation

Light piston engine and turboprop aircraft generally use electrically–driven systems to deploy their high-lift surfaces. The same surfaces on modern narrow and wide–bodied airliners are subject to considerably higher airloads on approach for which electric motors are unsuitable. However, they still require an actuation system that is compact in volume and relatively weight efficient. These systems are usually manufactured by companies external to the aircraft manufacturer. Three categories of component make up the majority of actuation weight in modern airliners: power drive units (PDUs), geared rotary actuators (GRAs), and drive shaft/universal joint combinations.

There are two PDUs in an actuation system: one for the leading edge (slats) and one for the trailing edge (flaps). Both are located inside the aircraft fuselage, between the wing roots. The principal component of each PDU is a hydraulic motor, which turns hydraulic pressure into rotational torque. The torque is delivered through shafts extending out of the PDU in both directions and into each wing. An example of a PDU is shown in Figure 2.8.

These torque shafts extend along the wings as far as the outermost high-lift panel, and use angle gearboxes to route around structural members and to follow the wing kink. Universal joints accommodate wing flex. The torque shafts provide torque to each GRA 'station' with a three–way angle gearbox as shown in Figure 2.9. The red double–headed arrows show torque being delivered to each GRA.

The GRA is a highly compact reduction gearbox which reduces the RPM – and correspondingly increases the torque – delivered by the torque shafts by approximately two orders of magnitude. Each high-lift panel has two GRAs to operate the mechanism that deploys it. An example of an aircraft GRA is shown in Figure 3.1.

A summary of all these components is given in Table 2.7 and a schematic of a typical system shown in Figure 2.11.

Alongside much of the aircraft structure, in the twenty years since the weight breakdown shown in Figure 2.3 was made, the high-lift surfaces have seen increasing use of composites in their construction. The consequence of this is that the relative contribution of the actuation system to the total high-lift weight is also likely to have increased beyond the 25% given here. Accurate actuation weight estimation is therefore fundamental to accurately estimating secondary wing weight.

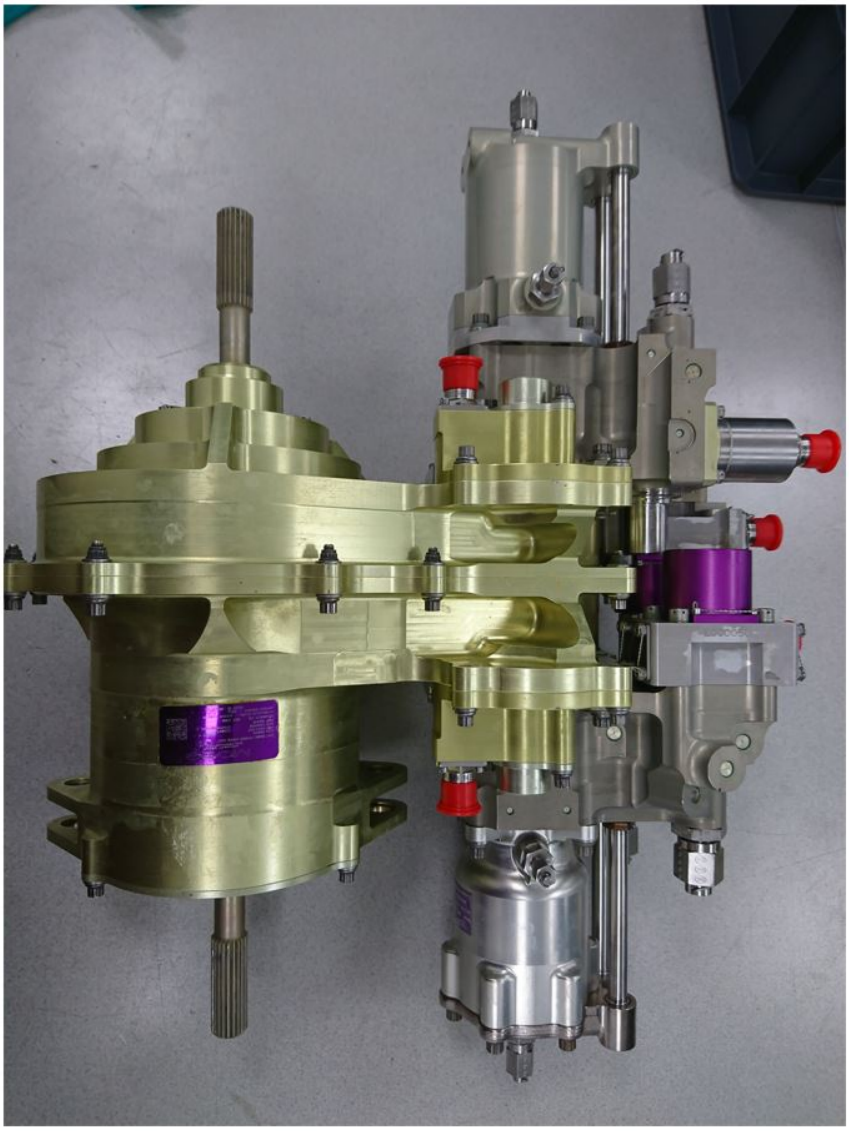

FIGURE 2.8: Photograph of a Power Drive Unit. The shafts extending in both directions to deliver torque to both wings can be seen. Credit: Moog Aircraft Group.

TABLE 2.7: Key high-lift actuation components.

Component category	Quantity per aircraft	Description
PDU	2	One unit each for the flaps and slats. Consists of a hydraulic motor located in the fuselage between the wing roots.
GRAs	8–22	Usually two per flap/slat panel. These compact reduction gearboxes provides high torque to actuate high-lift surfaces against airload.
Shaft & UJ	10–30	At least one shaft/UJ per GRA. They transmit torque from PDUs to GRAs along fast–rotating shafts and UJs accommodate wing flex.
Misc.	N/A	Includes additional components such as wing tip brakes, position sensors, computer controller.

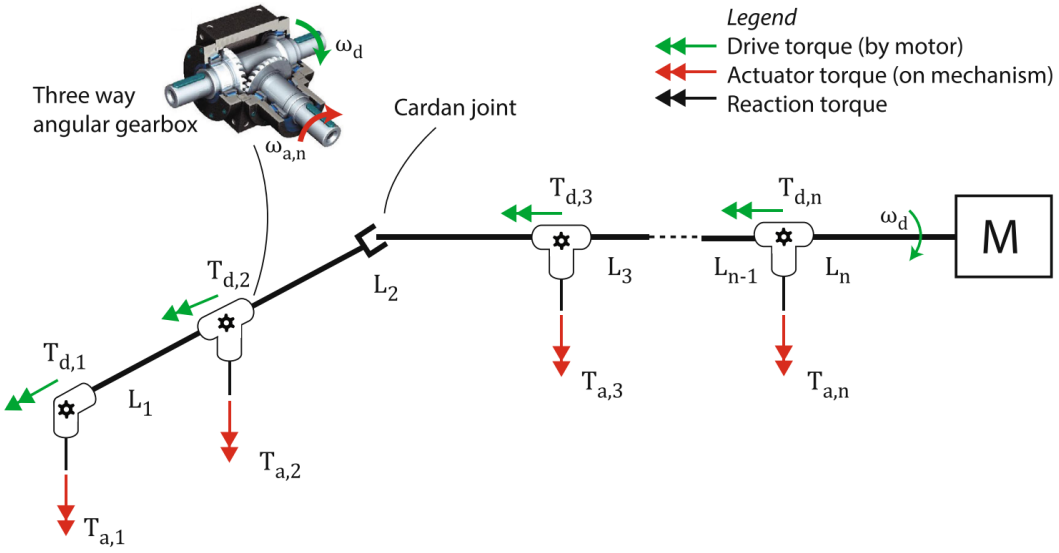

FIGURE 2.9: Schematic of torque tubes and three–way angle gear boxes in part of a high-lift actuation system [55].

FIGURE 2.10: Photograph of a Geared Rotary Actuator. Credit: Moog Aircraft Group.

The geometry of the high-lift panels and the airflow around them induce forces on high-lift system. In order to rotate and extend these panels into the airflow during deployment, these forces need to be overcome by the actuation system. Outlined in this section is a description of the method used to compute the loads and moments on a high-lift panel, and the relationship between these loads and the actuation system

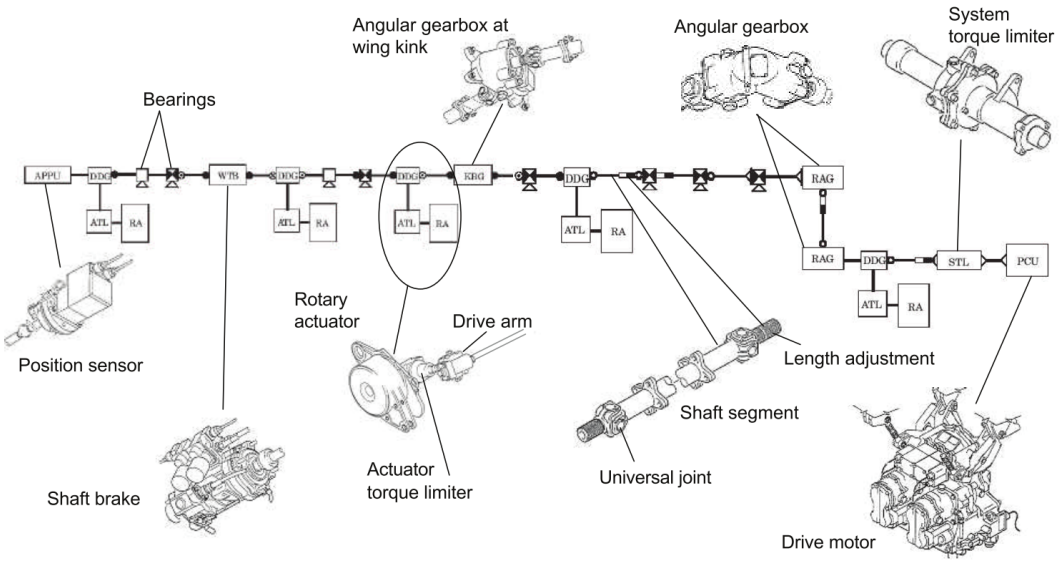

FIGURE 2.11: Components of a high-lift system [39].

design parameters. Moog Aircraft Group has provided much of the expertise in this area.

Leading edge actuation design philosophies

An industrial placement by the author at Moog Aircraft Group revealed that it is common for the aircraft manufacturers to opt for common parts in the high-lift system to save on certification cost, even if there is a weight penalty. One notable example is that of the leading–edge GRAs. Despite the five slat panels on each wing being subject to different loads, common GRAs were used for the inboard and outboard of each slat panel. This meant that although some actuators were larger than required, each aircraft has 20 leading edge GRAs (2 per slat panel, 5 slats per wing) of only two different types, instead of 20 GRAs of 10 different types. These two approaches will be referred to as 'low cost' and 'low mass' respectively. There is a weight penalty associated with opting for a low–cost design and it is quantifying this penalty is not current conceptual design capability. This is discussed further in 3.3.1.

Hinge moments and track loads

Nominally, each high lift panel has two tracks, with one at each end of the panel. These provide structural support to the panels and form the kinematic connection between the fixed wing and the moving flap panel. Each track is driven by one GRA, and the torque demanded of that GRA depends almost entirely on its respective track load and any mechanical advantage delivered by the kinematics at that load station. The tracks are where the torque from the GRAs is delivered to the high-lift panel, and act to rotate it about an axis known as the hinge line [44]. Figure 2.12 diagrammatically represents the tracks on each of the five slat panels and two flap panels of an Airbus A320 aircraft.

Calculating the track loads from CFD data involves finding the location of the centre of action of the pressure forces perpendicular to the panel hinge line hinge so that a hinge moment can be derived. The pressure force on a panel surface is given by the integral in Equation 2.19.

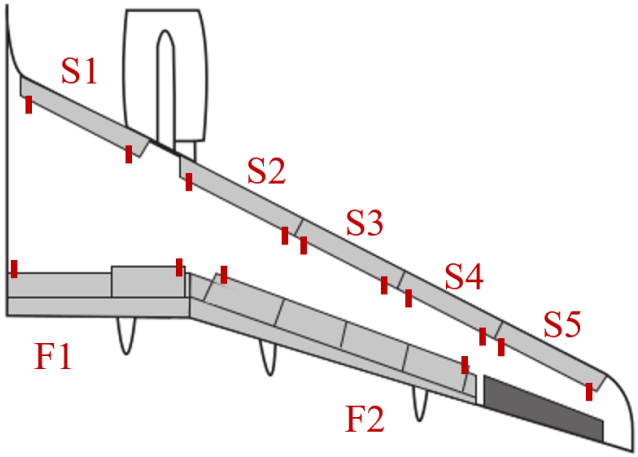

FIGURE 2.12: High-lift panel track locations on starboard wing of Airbus A320. Slat panels are denoted S1-S5 and Flap panels F1,F2.

$$F = \oiint_S -p\,\hat{\mathbf{n}}\,\mathrm{d}S \tag{2.19}$$

Where p is the pressure force on surface element $\mathrm{d}S$ and $\hat{\mathbf{n}}$ with unit normal vector $\mathrm{d}S$. This surface integral encompasses both the physical upper and lower surfaces of the panel. The minus sign indicates that the pressure force operates in the opposite direction to $\hat{\mathbf{n}}$. If the hinge line is given by $\mathbf{h_0} + \hat{\mathbf{h}}$, and $\mathbf{S}$ is the position vector of the surface element $\mathrm{d}S$, the hinge moment is given by Eqn. 2.20.

$$M = \oiint_S -p\,\left((\mathbf{S} - \mathbf{h_0}) \times \hat{\mathbf{h}}\right) \cdot \hat{\mathbf{n}}\,\mathrm{d}S \tag{2.20}$$

This equation is represented diagrammatically in Figure 2.13.

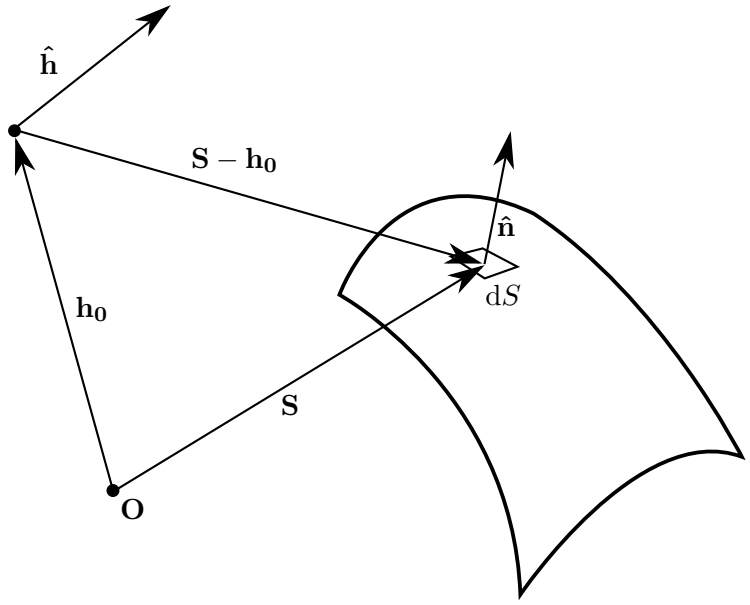

FIGURE 2.13: Surface integral to find pressure–induced moment about a hinge line.

CFD solvers such as DLR-TAU output the pressure-force vectors for each surface element on the aerodynamic surface in question. In this case, Eqn. 2.20 can be

discretised to become

$$F = \sum_{i=1}^{n} \left((\mathbf{S_i} - \mathbf{h_0}) \times \hat{\mathbf{h}} \right) \cdot \mathbf{F_i} \tag{2.21}$$

Where $\mathbf{F_i}$ is the force vector at surface element $\mathbf{S_i}$.

The sum of all the force elements on the high-lift surface (calculated using Eqn. 2.21) has a 'resultant'; a single force vector which is equivalent to this vector sum. The magnitude and perpendicular distance of this resultant from the hinge line give the total hinge moment across both tracks. The individual track load depends on both the force generated by the airload about the hinge–line and on the lateral proximity of the airload resultant to the track. This determines the distribution of the moment between the two tracks (see Figure 2.14).

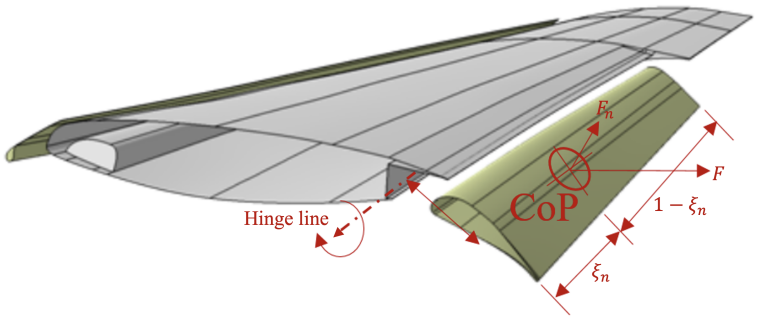

FIGURE 2.14: Diagram of a flap panel showing the hinge–line, force resultant, F, and the lateral position of force resultant, ξ_n as a proportion of panel length. The force resultant, F_n, is the component of F in the direction of the mutual perpendicular to the hinge–line and the panel chord line.

Kinematics

The GRA torque demand can be related to the track torque requirement with the kinematic mechanical advantage (Eqn. 2.22). This is ratio of angle turned by the GRA to the angle turned by the panel and depends on the mechanism design. Based on Moog design experience, a typical value for mechanical advantage for the leading edge system is 15–20, and 3–3.5 for the trailing edge.

$$\text{GRA Torque} = \frac{\text{Track load (kNm)}}{\text{Mech. adv.}} \tag{2.22}$$

High-lift actuation power demand

The power requirements for the leading and trailing edge systems are used to determine the size of the PDUs. The PDU power requirement can be built up by summing the power demands at each panel. These are determined by multiplying peak panel hinge moment, $M_{H\text{panel}}$, by the average angular rotation rate of the associated flap/slat panel. Typical deployment angles for trailing edge and leading edge systems are ϕ_{flap} = 30-40° and ϕ_{slat} = 7-10° respectively. Deployment times, $t_{\text{deploy}} \approx$ 20s. Eqn. 2.23 gives the power requirements for the leading and trailing edges systems including the conversion from degrees to radians and accounting for transmission efficiencies, η, in the order of 90%. The factor of two represents the two wings that each PDU powers.

$$\begin{aligned} \mathrm{PDU}_{LE} &= 2 \sum_{\mathrm{slat}=S1}^{\mathrm{slat}=Sn} M_{H_{\mathrm{slat}}} \frac{2\pi\phi_{\mathrm{slat}}}{180\ t_{\mathrm{deploy}}\eta_{\mathrm{LE}}} \\ \mathrm{PDU}_{TE} &= 2 \sum_{\mathrm{flap}=F1}^{\mathrm{flap}=Fn} M_{H_{\mathrm{flap}}} \frac{2\pi\phi_{\mathrm{flap}}}{180\ t_{\mathrm{deploy}}\eta_{\mathrm{TE}}} \end{aligned} \tag{2.23}$$

Chapter 3

A priori high–lift system sizing using industrial data

3.1 Actuation weight data

Section 2.2.2 outlined the key components of the high–lift actuation system.

3.1.1 Geared rotary actuators

Presented in Figure 3.1 is the mass, diameter and lengths of 25 different GRAs plotted against their designed peak output torque. These GRAs are all from the high–lift systems on various aircraft, predominantly Airbus and Boeing. For similar GRA architectures, the mass of a GRA depends on the torque requirement and the material properties (density and material strength). Buckingham π theorem states that the number of dimensionless groups, p, depend on the number of physical variables, n, minus the number of physical dimensions k: $p = n - k$ [56]. For the GRA mass, the dimensional analysis is shown below

$$\begin{array}{lll} m_{\mathrm{GRA}} & \text{depends on} & (\tau, \quad \sigma, \quad \rho) \\ M & & ([ML^2T^{-2}],[ML^{-1}T^{-2}],[ML^{-3}]) \end{array}$$

$$\begin{array}{lll} m_{\mathrm{GRA}} & \text{depends on} & \dfrac{\tau\rho}{\sigma} \\ M & & M \end{array}$$

The term ρ/σ is the ratio of the material strength to the material density. All GRAs are constructed from high strength hardened steel [57] so this quantity is fixed. GRA mass, m_{GRA} is therefore a linear function of design torque, τ. The volumetric space that GRAs occupy depend on their mass and the material density, so this quantity is also linearly dependent on τ.

Regression analysis was performed to fit lines of best fit of the form $y = ax + b$ (see Table 3.1), where x and y represent the independent (output torque) and dependent (mass or volume) variables respectively. The plot of torque against mass in Figure 3.1a shows two distinct groups of GRAs: a low torque and a high torque group. Separate lines of regression are used for each of these groups as seen. Parameters a and b are the fitting variables and represent the gradient and y-intercept of the line of best fit. The GRA mass fit have two of each a_1, a_2, b_1, b_2..

GRA mass and volume both show strong correlations to output torque. It can be seen that the GRA fitting has a positive non-zero y-intercept because there is some of the mass of the casing, shafts and other components that do not contribute directly

to the torque capability. In other words, a hypothetical zero-torque GRA would have a non-zero mass.

There is somewhat more scatter in the volume data which may be due to installation envelope or operating constraints that are not accessible to a simple dimensional analysis. These data have been provided by industrial partner Moog Aircraft Group for the commercial aircraft operating their actuation systems (including the Airbus A340, A350, A380, Boeing 787 and COMAC C919).

The computed values for a and b for each dependent variable are shown in Table 3.1 along with their respective R^2 values. The R^2 value gives the proportion of the variation in the dependent variable (GRA mass or installed volume) that is predictable from the dependent variable (peak design torque). These fitting values can then be used to estimate the mass of any GRA in a new high–lift system as discussed in the next section. The 'cross-over' value of torque from low to high is taken as 11900kNm, or about 0.22 on the normalised rated torque x-axis.

TABLE 3.1: Fitting values and goodness of fit for selected GRAs.

GRA Variable	Fitting value		R^2
	a	b	
Mass (Low torque, kg)	2.094e-3	3.525	0.6854
Mass (High torque, kg)	9.964e-4	16.659	0.8422
Volume (mm^3)	1.221	1.778e4	0.8126

3.1.2 Power drive units

The same linear scaling function as the GRAs has been used and demonstrates the expected relationship between power requirement and weight: PDU weight increases with increasing power demand. This relationship is shown in Figure 3.2.

Table 3.2 shows the fitting values a and b in the fitting equation $y = ax + b$ where y represents the PDU weight in kg and x is the peak demanded power output. Only three data points were available for Moog PDUs but the large R^2 suggests a strong linear correlation between the peak power demand and the mass for the three data points available, although with only three data points, the opportunity for a large spread of values (and a corresponding reduction in R^2) is reduced.

TABLE 3.2: Linear fitting values for PDUs.

PDU Variable	Fitting value		R^2
	a	b	
Mass (kg)	0.00114	12.38	0.9835

3.1.3 Other components

Although PDUs and GRAs together represent a majority of the actuation weight, the other components listed in Table 2.7 need to be accounted for. Based on information and design experience provided by Moog Aircraft Group, GRA and PDU weight makes up approximately 68% and 52% of the trailing edge and leading edge actuation weight respectively. One possible explanation for the smaller leading edge proportion is the higher number of leading edge slat panels than trailing edge flap panels. This means more UJs and angled gearboxes relative to GRAs and PDUs are required and a lower

proportion of total mass is therefore made up of GRAs and PDUs in the leading edge actuation subsystem.

A good estimate of total actuation weight can be made by multiplying the sum of the GRA and PDU weight for the leading edge system and trailing edge system by $1/0.52 = 1.91$ and $1/0.68 = 1.47$ respectively. This accounts for the additional weight of the other components in the actuation system including the torque shafts, UJs, angle gearboxes and electronics.

3.1.4 Actuation weight estimation method

Given a high–lift design that satisfies the field performance constraints outlined in 2.2.1 and 2.2.1, the stall speed in the landing configuration can be computed from the lift polar for the high–lift wing. The stall speed is used to calculate the flow condition that sizes the high–lift actuation system and is determined by certification requirements. This is described in more detail in 3.2.2. The hinge moments and track loads induced by the flow on each of the high–lift surfaces can be calculated using the method described in 2.2.2. The kinematic design of the high–lift wing affects the torque demanded of the GRAs, but within a limited range (as outlined in 2.2.2). The torque required of each GRA can therefore be estimated using Equation 2.22. The fitting variables given in Table 3.1 can then be used to make a weight estimate for each GRA based on torque demand. Separately, the hinge moment and minimum high–lift deployment time can be used to estimate the peak power demanded of the leading and trailing edge PDUs as outlined in 2.2.2. This power requirement can be used to estimate the PDU mass using the fitting variables from Table 3.2. Finally, the sum of the weight estimates of the GRAs and PDUs can be scaled up to provide an estimate for the all–up weight of the high–lift actuation system as described in 3.1.3.

This process is shown diagrammatically in Figure 3.3 and a preliminary validation and demonstration is undertaken here.

3.1.5 Quantification of uncertainty in actuation weight estimation

The distribution of points around the line–of–best–fit shown in Figure 3.1a means that there is inherent uncertainty in the mass of the GRAs. The predicted mass of an individual GRA, $m_{\mathrm{GRA},i}$, can be modeled by assuming that its value is normally–distributed random variable with mean μ_i and variance σ_i^2:

$$m_{\mathrm{GRA},i} \sim N\left(\mu_i(\tau_i),\ \sigma_i^2\right) \tag{3.1}$$

The mean, $\mu_i(\tau_i)$, takes a value on the line–of–best fit the line–of–best fit already described, and is a function of demanded torque, τ_i. Upper and lower bounds for the mass fit one standard deviation above and below the mean are shown in Figure 3.4.

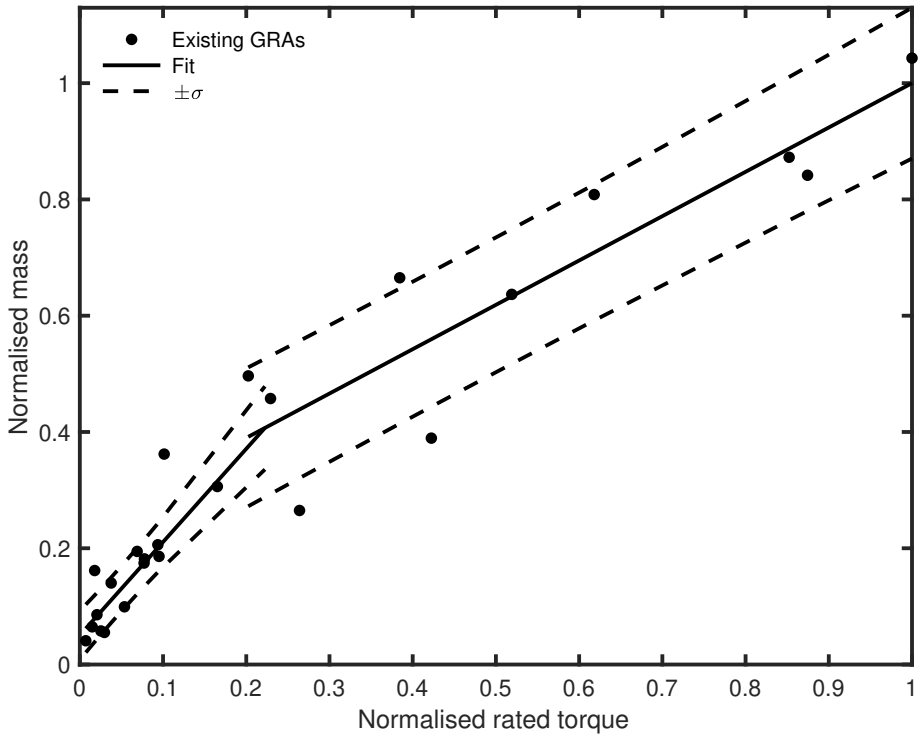

FIGURE 3.4: GRA mass fit with $\pm\sigma$ confidence intervals.

For an actuation system containing multiple GRAs, the total mass of the GRAs in the system is given by $\sum_i m_{\mathrm{GRA},i}$ and is also normally distributed such that:

$$\sum_i m_{\mathrm{GRA},i} \sim N\left(\sum_i \mu_i(\tau_i),\ \sum_i \sigma_i^2\right) \tag{3.2}$$

For a high lift system with n independently–sized GRAs, the total GRA mass, M, $\pm\sigma$ error bar values, M_{upper} and M_{lower} are given by Equation 3.3.

$$\begin{aligned} M &= \sum_{i=1}^{n} \mu_i \\ m_{\mathrm{GRA,lower}} &= \sum_i \mu_i(\tau_i) - \sqrt{\sum_i \sigma_i^2} \\ m_{\mathrm{GRA,upper}} &= \sum_i \mu_i(\tau_i) + \sqrt{\sum_i \sigma_i^2} \end{aligned} \tag{3.3}$$

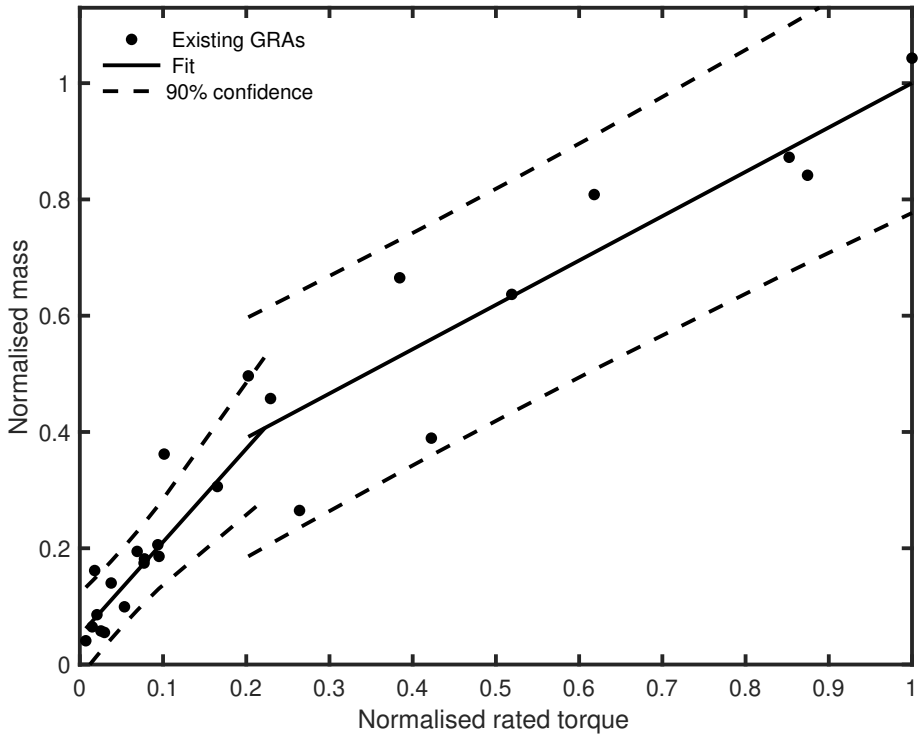

(A) Normalised rated output torque against normalised mass for Moog GRAs. Two lines of best fit are used; one for the low-torque (<11900kNm) GRAs and one for the high torque GRAs.

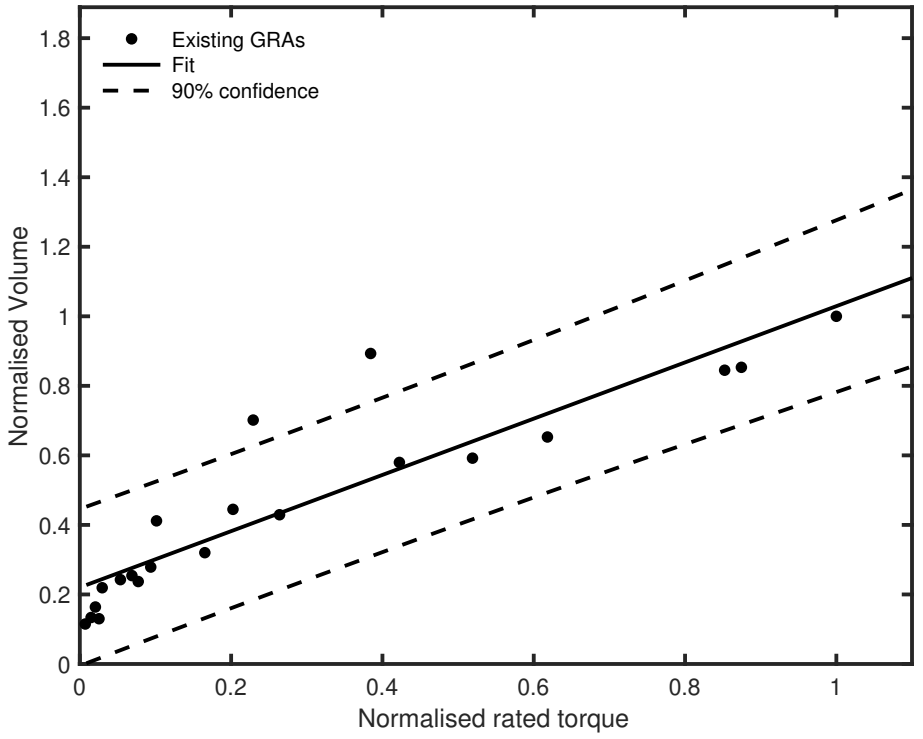

(B)

FIGURE 3.1: Plots showing normalised rated torque against normalised mass and volume. 90% confidence intervals are shown for each.

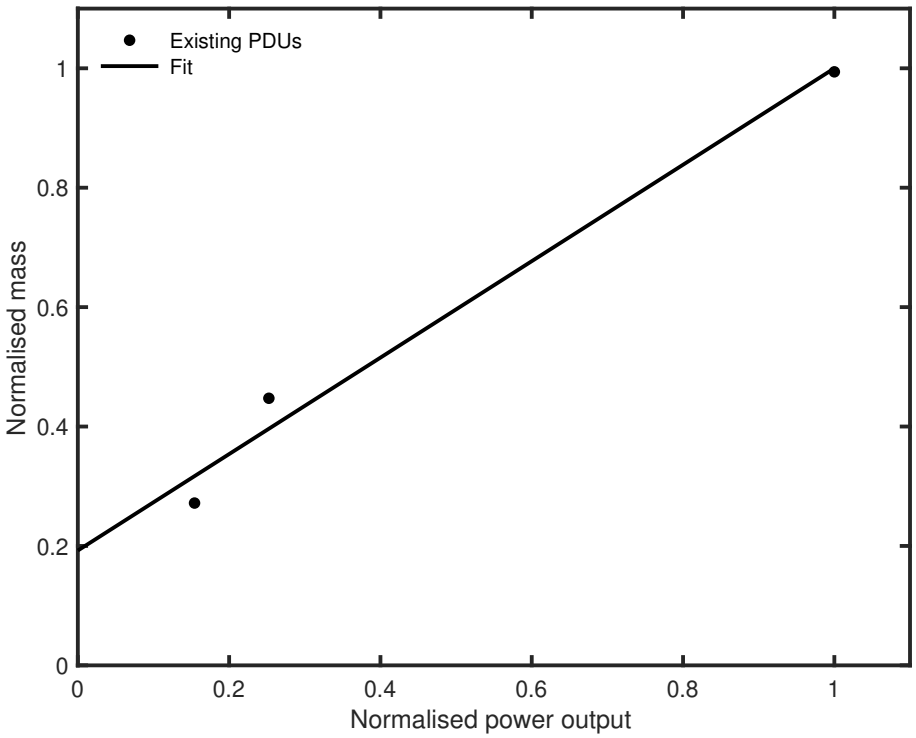

FIGURE 3.2: Linear fit correlating power requirement to mass for three PDUs.

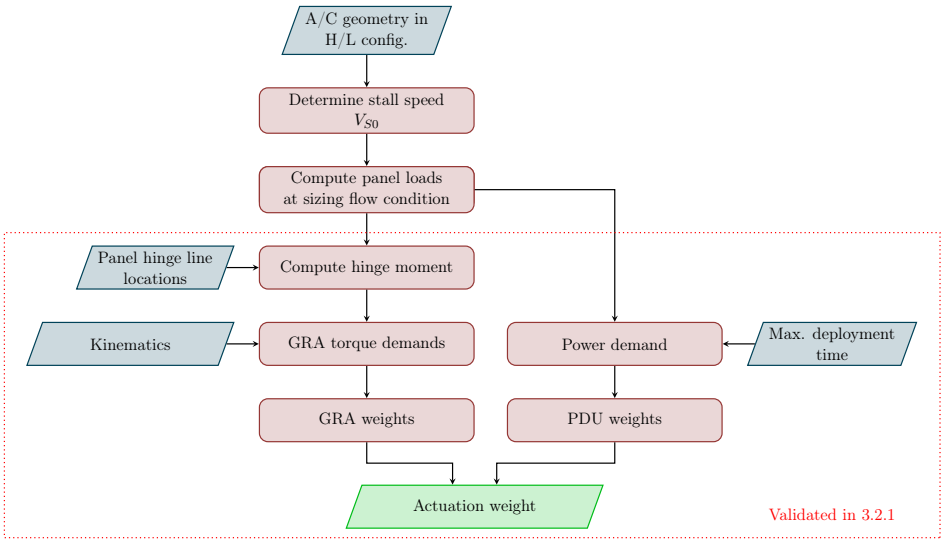

FIGURE 3.3: Actuation weight estimation workflow.

3.2 Comparison to representative aircraft

The mass and design data presented in Section 3.1 could be used to estimate the actuation weight earlier in the aircraft design cycle, when basic high-lift geometries are being investigated. However, this method requires validation to demonstrate its viability. Validation of the the high–lift actuation weight estimation method used airload data from a real aircraft to provide the inputs shown in Figure 3.1.4. The weight breakdown of the actuation system that was eventually installed in that aircraft was then compared with the estimates to assess the performance of the method. This validation takes place in Section 3.2.1.

Next, the loads estimation method was demonstrated, this time for an aircraft with readily available high-lift geometry. Verification of the CFD results was performed to increase confidence in the loads prediction. This is described further in Section 3.2.2.

3.2.1 Validation of the high-lift actuation method

FIGURE 3.5: The COMAC C919, a narrow-body twinjet airliner very similar to the Airbus A320 [58].

Using design hinge moment and mechanism data provided by Moog Aircraft Group for the under–development COMAC C919 aircraft, an estimate of the actuation weight was compared to the true value. This allowed for validation of the second half of the workflow in Figure 3.3, as shown in Figure 3.6.

The input data for the model is shown in Table 3.3, but moment values have been normalised here to protect sensitive industrial data. Though descriptions of each value are given in the table, the reader is referred to 2.2.2 for more information on their meaning. Moments were normalised against the single largest value and retain their relative sizes.

The weight estimate of the actuation system made using this method was within 10% of the true weights for both the leading and trailing edge systems. These results

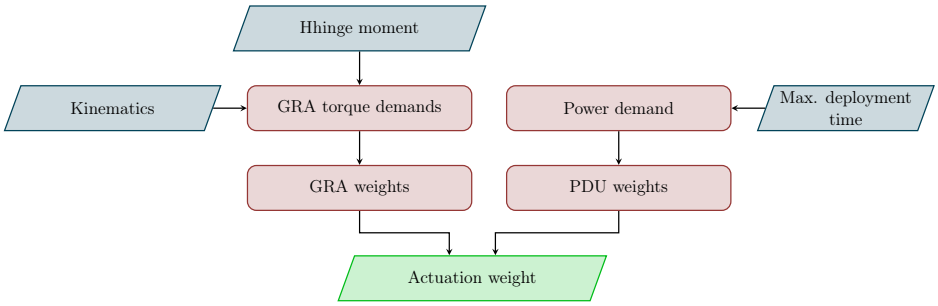

FIGURE 3.6: Actuation weight estimation workflow for C919 with panel hinge moments provided. This is a subset of the full process in Figure 3.3.

TABLE 3.3: Inputs and normalised forces used for C919.

Input	Value	Description
Flap moments	F1 – 0.67 F2 – 1.0	Normalised flap hinge moments
Flap force resultant	F1 – 0.81 F2 – 0.26	Proportion of panel moment on I/B track
	S1– 0.83 S2 – 0.54	
Slat moments	S3 – 0.4 S4 – 0.28	Normalised slat hinge moments
	S5 – 0.23	
	S1– 0.4 S2 –0.46	
Slat force resultant	S3 – 0.46 S4 – 0.45	Proportion of panel moment on I/B track
	S5 – 0.44	
Deployment time	19s	Time taken to fully deploy flaps/slats against airload
ϕ_{flap}	34°	Angle about which flap panel turns
ϕ_{slat}	9°	Angle about which slat panel turns
Flap mechanical advantages	F1 – 3.2 F2 –3.5	Eqn. 2.22
Slat mechanical advantages	S1 – 18.4 S2–S5 – 20	

are shown in Figure 3.7. The error bars represent one standard deviation of uncertainty for each of the leading edge, trailing edge, and total weight as estimated from the fitting uncertainty and were calculated using the method outlined in 3.1.5.

The small differences in mass between the in Figure 3.7 are likely due to the method failing to capture all necessary design considerations. Reasons for the small discrepancies seen include, but are not limited to:

- Poor accounting for frictional 'drag' of GRAs – the torque required to turn them under no load.
- Lack of PDU data points –only three were available.
- Incorrect assumptions on the scaling of the torque shafts and UJs.
- Impact of angled gearboxes on the total system weight and power requirement

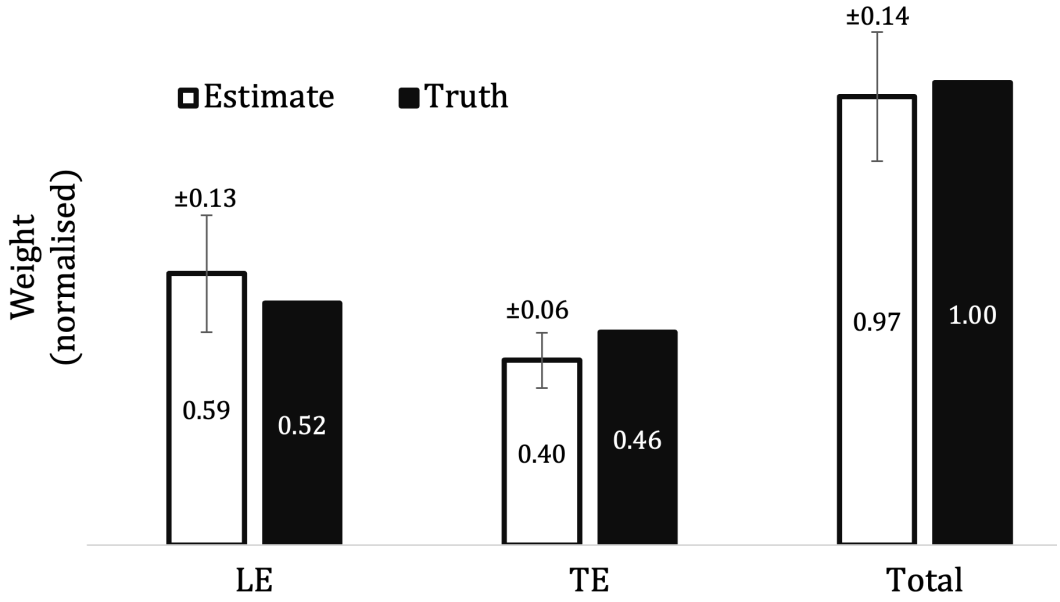

FIGURE 3.7: Validation of the high-lift actuation weight estimation method of the COMAC C919, with normalised data. Aerodynamic and hinge moment data was provided externally.

3.2.2 High–Lift Common Research Model

In 2017, NASA and the AIAA held the 3rd CFD High–Lift Prediction Workshop requesting participants to submit 3D simulation results of the CRM with the wing in a high–lift configuration [59]. The NASA Common Research Model (CRM) is a representative aerodynamic and structural model of a wide–body airliner [60]. This model provides the opportunity to test the estimation method on an open–source, full–sized aircraft using multi–fidelity CFD simulations that can be verified against the workshop results. The results shown in this section were computed using DLR-TAU on 64 cores using the University of Southampton's Iridis–4.

As can be seen in Figure 3.8, the HL-CRM has two flap panels and one slat panel. The slat and flap panels deploy to 30° and 37° respectively. A real aircraft of the CRM's size would certainly have more than one slat panel, and even small aircraft such as the A320 have five slat panels. However, the panel can be artificially broken into the desired number of panels and the forces on each virtual panel calculated individually (see Section 3.3.2). Reference parameters for the HL–CRM are given in Table 3.4. Where these were not available, values from the Boeing 777–200 – which is similar in size to the CRM model – were used.

3D–CFD verification

The computational grids were provided by the committee at the 3rd High Lift Prediction Workshop [62]. Course, medium, fine and extra fine grids were provided for the High Lift Prediction Workshop participants to use in lieu of their own grids. Participant results demonstrated that pressure coefficient profiles and force data did not change significantly using finer grids than the medium grid, and a 48 million cell unstructured hex–tet grid was used for the following analyses. For the present work, the CFD calculations were run using the DLR-TAU flow solver, a 2nd order unstructured CFD solver based on a finite-volume discretization scheme. The geometry of a configuration is mapped by a cell-vertex grid metric and stored via an edge-based data

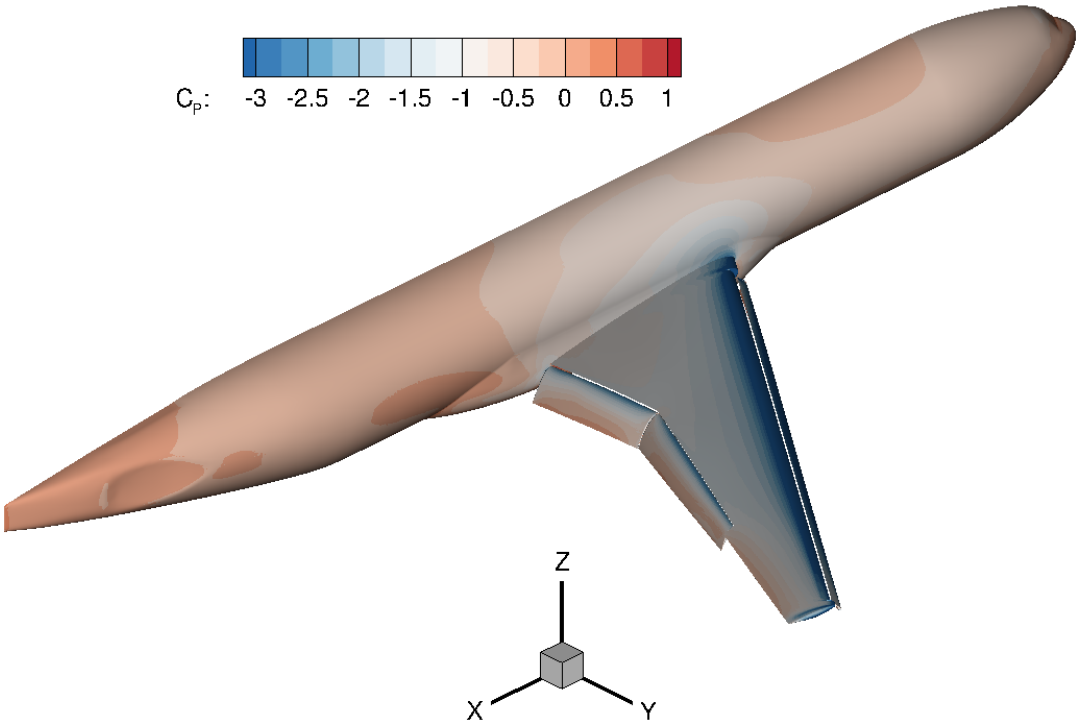

FIGURE 3.8: NASA Common Research Model in high–lift configuration. Flow conditions are M=0.2, α =16°, M = 0.2, $\rho = 1.125$kg m^{-3}, T = 288K

TABLE 3.4: Reference quantities for the high–lift configuration of the NASA Common Research Model

Parameter	**Value**	**Description**
MTOW (kg)[1]	229,510	Maximum takeoff weight [61]
MLW (kg)[1]	201,840	Maximum landing weight [61]
MZFW (kg)[1]	190,500	Maximum zero fuel weight [61]
b/2 (m)	29.4	Wing semi-span
$S_{\text{ref}}/2$ (m^2)	191.8	Wing semi-reference area
MAC (m)	7.01	Mean aerodynamic chord
MGC (m)	6.52	Mean geometric chord (S/b)
AR	9.0	Wing aspect ratio (b^2/S_{ref})
δ_s (°)	30.0	Maximum slat deflection angle
δ_s (°)	37.0	Maximum slat deflection angle

[1] Boeing 777-200 reference quantities used in lieu of unknown values for CRM.

structure. Multi–grid acceleration (4w) was turned on, and the Spalart–Allmaras turbulence model [63] with Edwards modification [64] was used. Reynolds number was 34.4 million based on a MAC of 7m. The CFL number used was 1.5. Achieved convergence for each case was between 10^{-4} and 10^{-5}. Table 3.5 shows the lift and drag coefficients at the two computed angles–of–attackfor the HL-CRM and demonstrate good agreement with other workshop participant results.

Surface pressure data at three spanwise locations (Figure 3.9) were extracted from the solution for comparison to those submitted by workshop participants. The flow conditions used were M = 0.2 and sea level conditions ($\rho = 1.125$kg m^{-3}, T = 288K).

TABLE 3.5: Aerodynamic coefficients computed using DLR-TAU at standard sea level conditions and M=0.2. Workshop results shown in parentheses [62]

	Coefficient		
	Present		
	(Workshop participant range)		
α	C_L	C_D	C_M
8°	1.79	0.171	−0.39
	(1.63 – 1.85)	(0.165 – 0.185)	(-0.45 – -0.3)
16°	2.41	0.275	−0.42
	(2.25 – 2.39)	(0.255 – 0.285)	(-0.45 – -0.2)

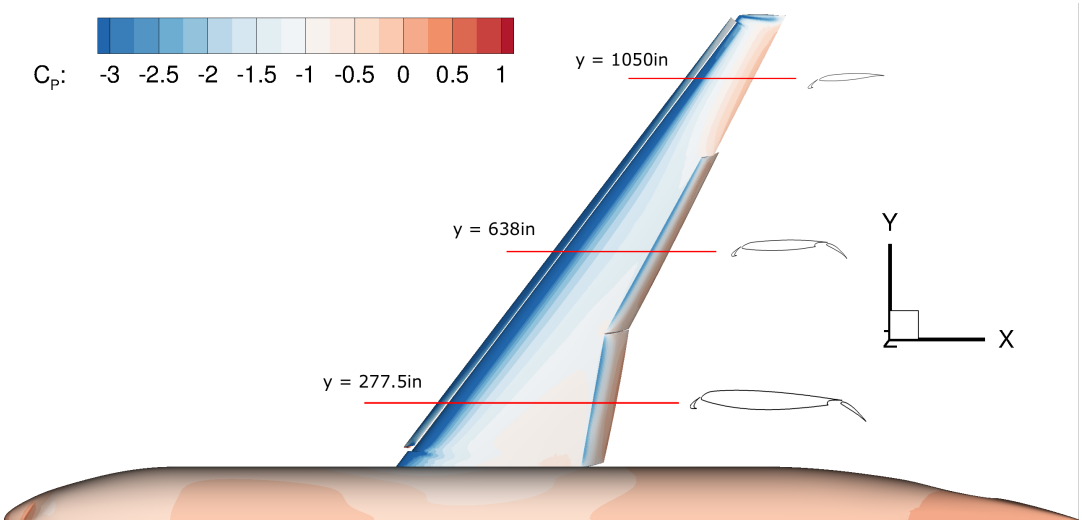

FIGURE 3.9: Slice locations for comparison to workshop results.

Surface pressure data from the computations performed here using DLR-TAU were compared to the workshop results and are shown in Figure 3.10. The good agreement demonstrated means the CFD surface pressure data can be trusted to provide force values required to estimate the hinge–moments on the high–lift surfaces.

Stall Characteristics

Section 25.335(e)(3) of the EASA Certification Specifications for Large Aeroplanes [65] states that the speed at which the wing flaps are deployed must not be less than $1.8\,V_{S0}$, with the aircraft at its maximum landing weight (MLW). The parameter V_{S0} represents the stall speed with high–lift surfaces fully deployed. The low–speed aerodynamic characteristics were calculated using CFD as source of the aerodynamic data.

The dependence of the lift coefficient on the angle of attack is shown in Figure 3.11a. Results were obtained at $M = 0.2$ and $Re = 3.4 \times 10^7$ based on mean aerodynamic chord. The wing stalls at an angle of attack of 17 degrees, reaching a maximum lift coefficient of 2.4. Stall can be seen progressing by inspecting the flow features on the wing as the C_L value moves through its maximum of 17°. Figure **??** shows C_F contours for two values of α, either side of $C_{L,\max}$. Separation can be seen occurring across a larger area inboard flap in the upper figure ($\alpha = 18°$), than in the lower figure ($\alpha = 15°$). Separation features can also be seen beginning at the very

outboard section for this α. A comparison to reference data for the low speed cases is not included here, but the reader is referred to [1] for a more comprehensive overview with comparison data. Lift coefficient, C_L, is calculated using Equation 3.4:

$$C_L = \frac{\text{Lift}}{0.5\,\rho\,V^2\,S_{\text{ref}}} \tag{3.4}$$

For an aircraft in steady descent, lift = MLW. The stall speed with high–lift surfaces deployed is determined from the equilibrium of vertical forces:

$$V_{S0} = \sqrt{\frac{\text{MLW}}{0.5\,\rho\,S\,C_{L,\,\max}}} \tag{3.5}$$

where the air density, ρ, is taken at sea level conditions of 1.225kg/m^3. One finds $V_{S0} = 59$m/s, and that the sizing lift coefficient for wing flaps deployment is:

$$C_{L,\,\text{sizing}} = \frac{\text{MLW}}{0.5\,\rho\,\left(1.8\,V_{S0}\right)^2\,S_{\text{ref}}} \tag{3.6}$$

providing $C_{L,\,\text{sizing}} = 0.74$. Using data in Figure 3.11a, the corresponding angle of attack is $-2.9°$. In summary, one finds that for the HL–CRM low–speed characteristics, the maximum speed for wing flaps to be deployed is $1.8\,V_{S0} = 107$m/s at sea level conditions. The relationship between the maximum deployable airspeed and the flow conditions relevant for sizing are discussed in Section 3.2.2.

Estimating the high-lift surface hinge line locations

Being a research model, the HL-CRM does not include any information on the location of the effective high-lift surface hinge line locations. Hinge lines are required to calculate the turning moment required to deploy the flaps against the air load. The position of the HL-CRM's high-lift hinge lines therefore need to be estimated which depend on the kinematics of the deployment system.

A number of mechanisms exist to deploy flaps and slats on fixed wing aircraft. To simplify the kinematic assumptions, the decision has been made to consider single–slotted trailing edge flaps and curved–track rack–and–pinion leading edge systems. As shown in Figure 2.2, these simpler mechanisms are increasingly the deployment system of choice for both Airbus and Boeing. An example of these mechanisms for a leading and trailing edge device are shown in Figure 3.12.

When deploying flaps and slats, the driving mechanism overcomes the loads acting on each element to rotate and translate the elements in their desired deployment setting. The magnitude of the torque required to overcome this load depends on two parameters:

1. The magnitude and direction of the resultant air load on the panel.
2. The placement of the effective hinge line about which the high–lift surface moves.

The placement of the instantaneous centre of rotation for each panel at a point in time during deployment depends on the kinematic design and the current deployment position, and cannot easily be determined without detailed design of the high–lift mechanisms. However, the mean hinge line, that is the vector about which the panel can be thought to rotate on average, can be synthesised from two known points: the retracted, and the fully deployed position. This is shown as three steps in Figure 3.13.

A similar approach to that shown in Figure 3.13 is used to compute the mean hinge point for the leading edge slat. Visual inspection of the curved track in Figure 3.12a reveals that it must have a centre located somewhere below and to the rear of the leading edge of the main wing. The torque required to rotate the panel against the airflow must therefore be about this point. To determine its exact location for the HL–CRM, planar sectional slices of the wing geometry were taken at the inboard and outboard extremes of each panel. Each planar section was orientated so that its normal aligned with the the sweep line of that panel, as shown in Figure 3.14.

The geometry for the HL–CRM includes the surfaces only in their fully deployed positions. Once a planar slice was taken of the inboard section of a high lift panel, the splines representing the surface of the high–lift panel were duplicated and then rotated though their deployment angle so that one copy was once again in the retracted position. Two lines adjoining the leading edges of the panel in both positions were connected and a perpendicular bisector drawn. The same was done for the trailing edge of the panel. The (x, y, z) location of the intersection of the two bisectors set the inboard location of the hinge line vector. This is shown in Figure 3.15. The same process is repeated at the outboard extremity of the panel with a new plane, and the vector joining the two points forms the hinge line for that panel.

Table 3.6 shows the estimated locations and directions of the effective hinge lines for the NASA HL-CRM.

TABLE 3.6: Table of estimated effective hinge line locations and directions.

	Hinge start (x,y,z) [m]	**Hinge end (x,y,z) [m]**
Flap 1	$(35.59, 3.63, 2.62)$	$(37.08, 11.00, 3.99)$
Flap 2	$(37.40, 11..89, 4.24)$	$(42.65, 20.82, 5.41)$
Slat	$(27.10, 3.76, 3.68)$	$(45.47, 28.65, 5.91)$

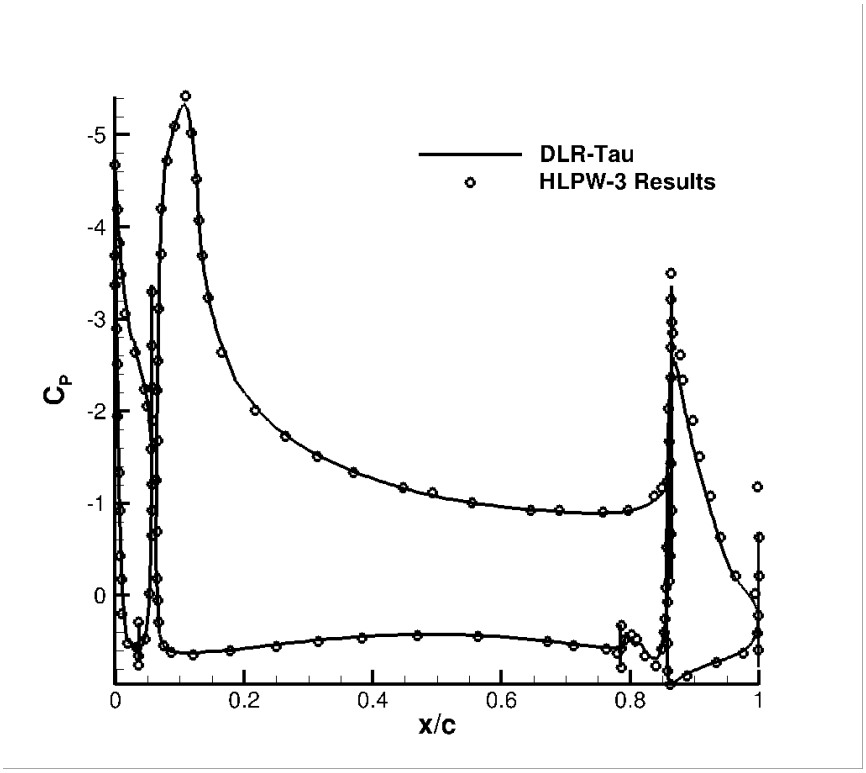

(A) y = 277.5in ($\eta = 0.240$)

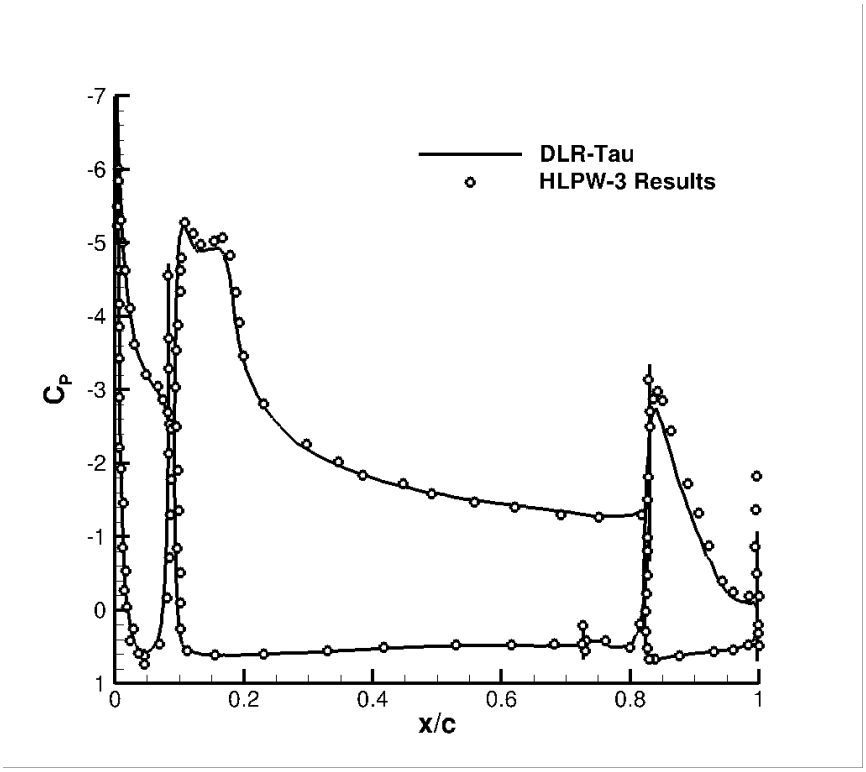

(B) y = 638in ($\eta = 0.552$)

FIGURE 3.10: Selected HL-CRM C_P profiles for comparison between Southampton simulations (DLR–Tau) and high–lift prediction workshop results (HLPW-3) at $\alpha = 16°$ [62].

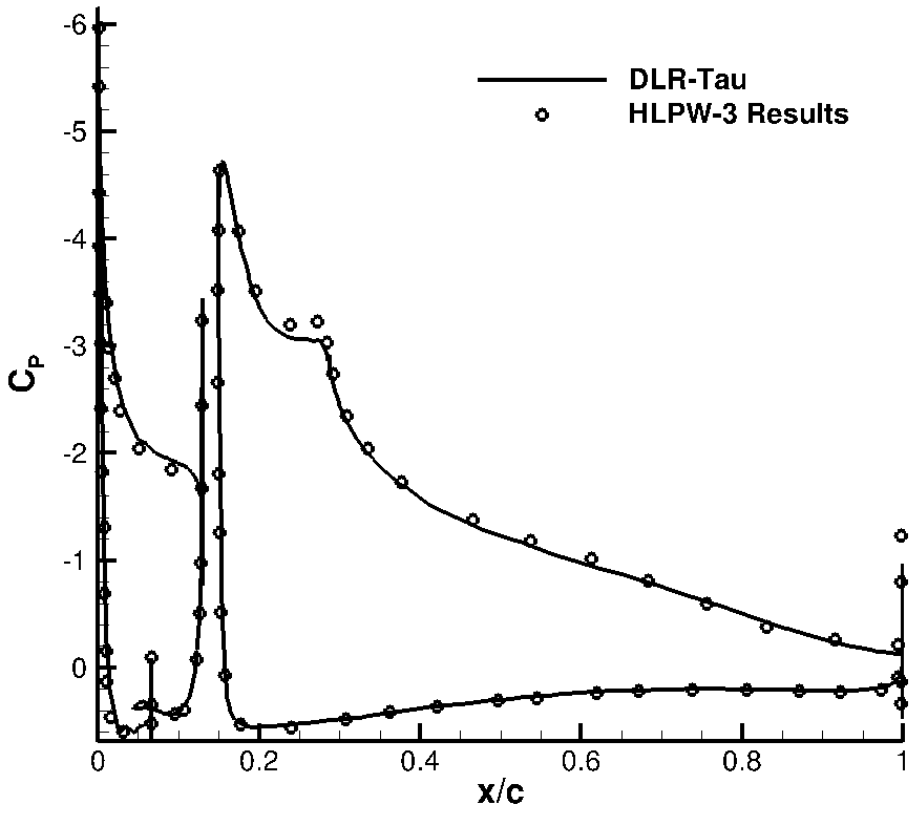

(c) y = 1050in ($\eta = 0.908$)

FIGURE 3.10: Selected HL-CRM C_P profiles for comparison between Southampton simulations (DLR–Tau) and high–lift prediction workshop results (HLPW-3) at $\alpha = 16°$ [62].

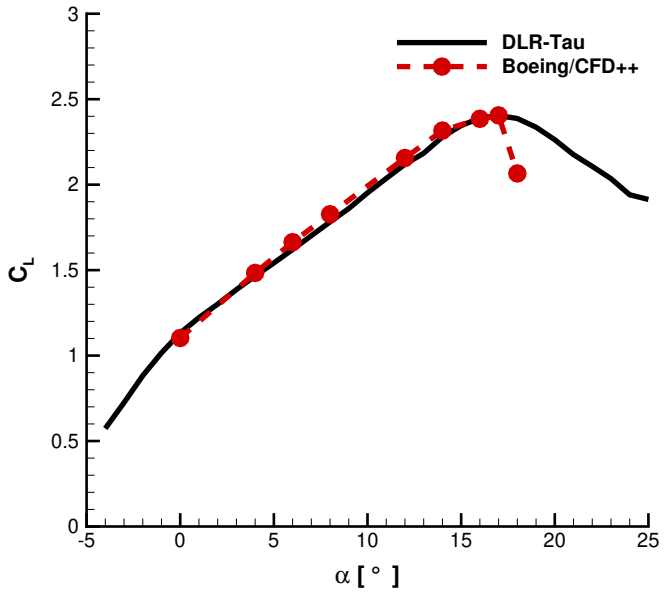

(A) Lift coefficient dependence on angle of attack verified against [66].

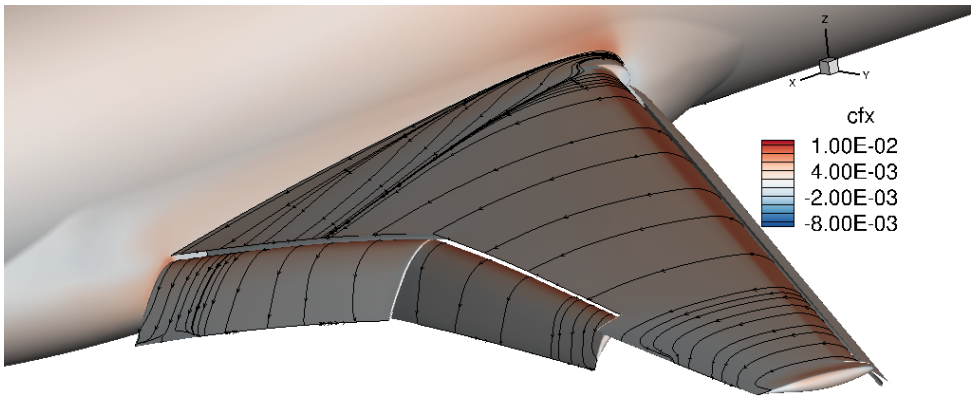

(B) Contour plot of C_F for $\alpha = 16°$.

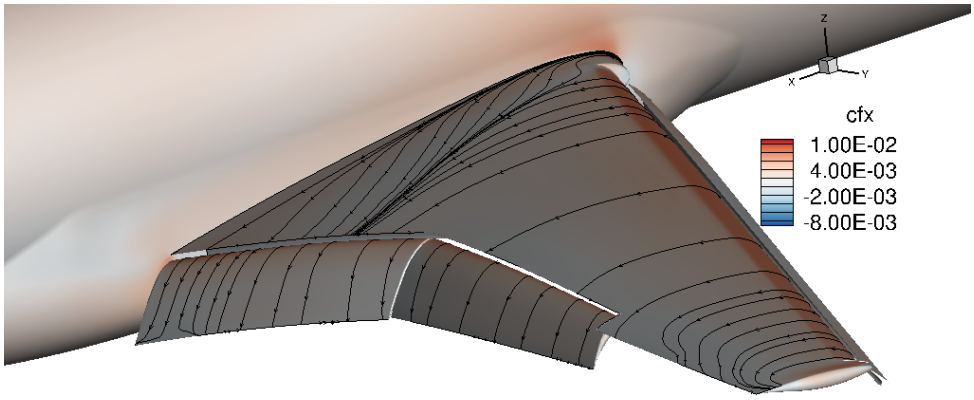

(C) Contour plot of C_F for $\alpha = 18°$.

FIGURE 3.11: Low speed characteristics of the HL–CRM ($M = 0.2$ and $Re = 3.4 \times 10^7$ based on mean aerodynamic chord).

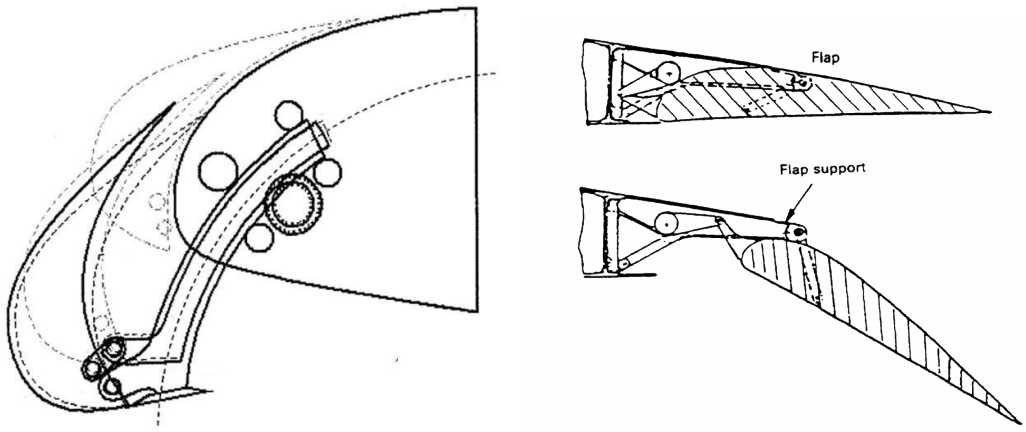

(A) Curved track, rack–and–pinion leading edge mechanism [67]

(B) Single-slotted Fowler flap trailing edge mechanism [68]

FIGURE 3.12: Selected leading and trailing edge high–lift deployment mechanisms

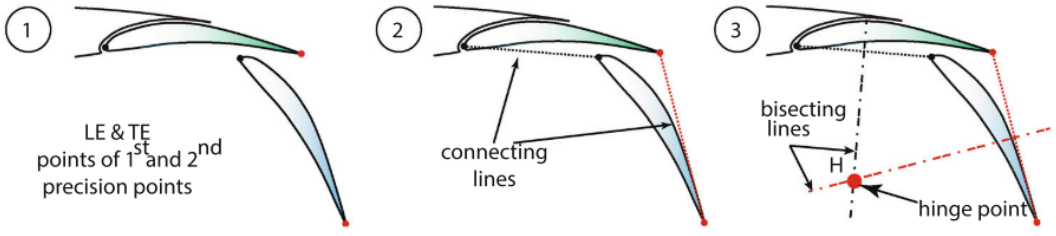

FIGURE 3.13: Synthesis of panel hinge point in 2D [55]

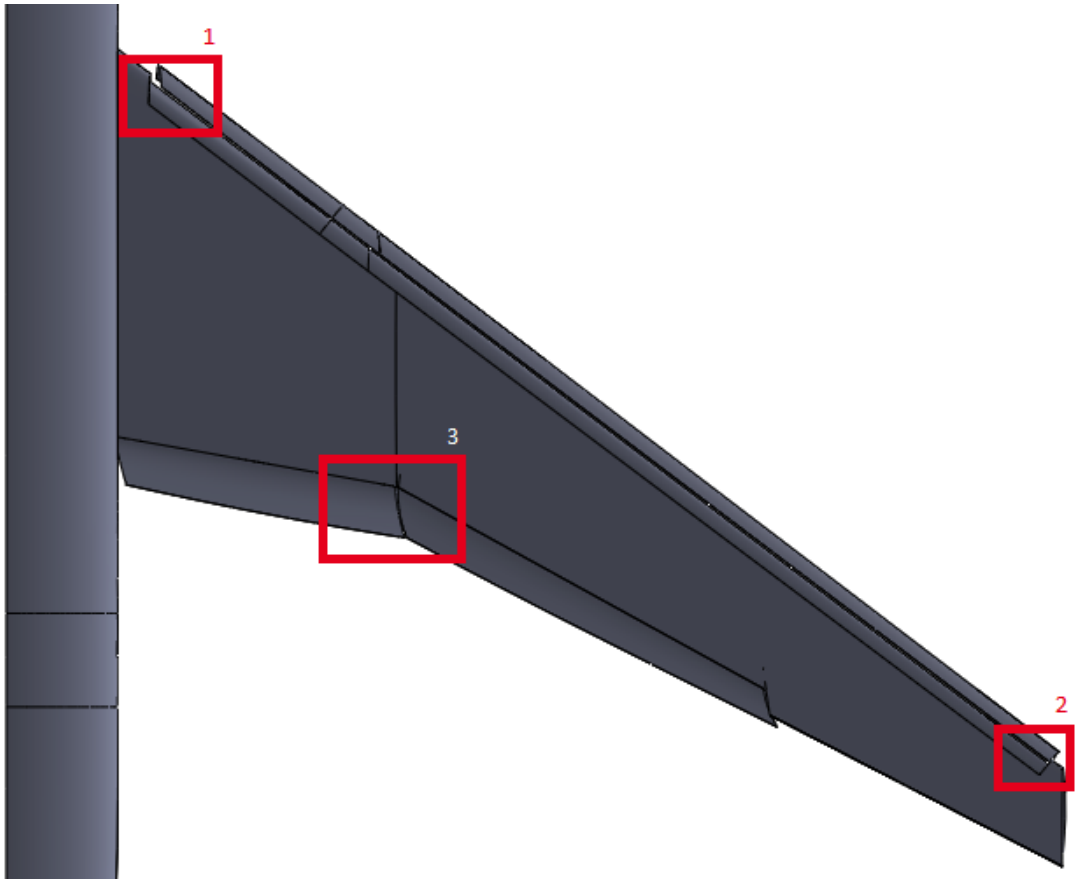

(A) CRM wing showing locations of insets.

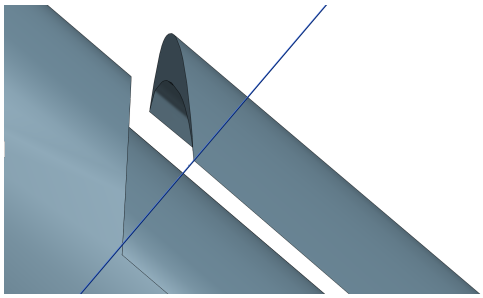

(B) Inboard section of slat panel (1).

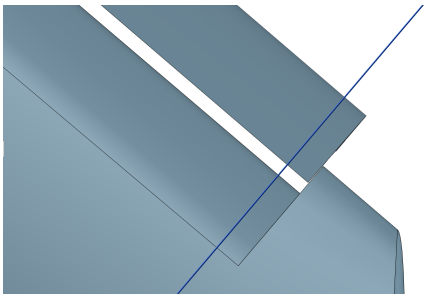

(C) Outboard section of slat panel (2).

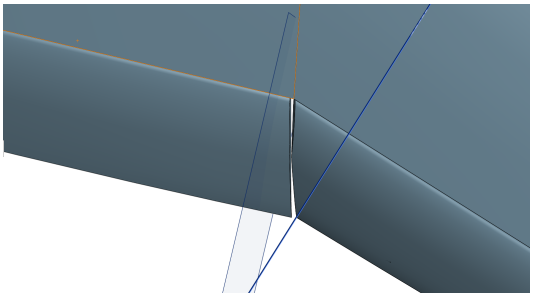

(D) Outboard section of Flap 1 and inboard section of Flap 2 (3).

FIGURE 3.14: CAD screenshots showing the some of the planar slices used for determining the effective hinge line location on each panel

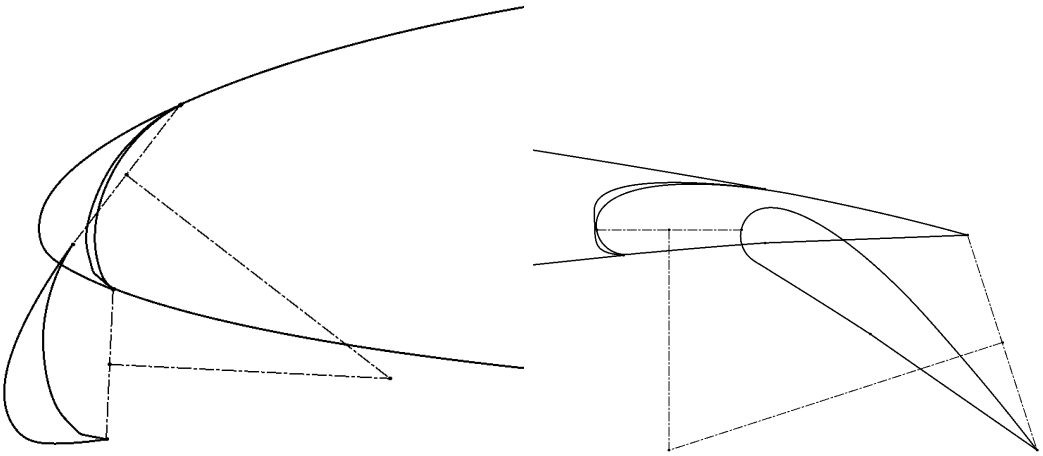

(A) Slat hinge point. (B) Flap hinge point.

FIGURE 3.15: Geometry of two planar sections of the HL–CRM wing showing the effective hinge line placement in one plane of the slat and a flap panel for the HL–CRM.

High-lift panel hinge moment estimation

In Section 3.2.2, the flow condition for sizing was taken as sea–level standard atmosphere, with angle–of–attack = $-2.9°$ and $V_a = 107$m/s. The CRM must therefore be able to deploy high–lift surfaces in all flow velocities from the stall speed up to and including $1.8V_{S0}$. To estimate the sizing flow condition, a range of V - α pairs were selected for 3D simulation within DLR-Tau. The chosen values are given in Table 3.7. The V range is first selected, corresponding to the range of V in the CRM's deployment envelope: $V_{S0} \leq V \leq 1.8\,V_{S0}$. Corresponding C_L values are calculated using Equation 3.4. These α values are then interpolated from Figure 3.11a.

Table 3.7: Table showing V - α pairs and the corresponding C_L for the HL-CRM for standard sea level conditions when MLW = 201,840gN. A concentration of points around $\alpha = 9°$ was chosen to resolve the peak slat hinge moment which occurs here. Values of $\alpha < 1.93°$ did not converge.

V [m/s **]**	59.2	61.6	64.4	65.7	66.0	66.4	66.7	67.0	67.3	67.5	67.7	68.0	71.2	75.5	80.7
α[°]	16.9	13.4	11.0	10.0	9.8	9.6	9.4	9.2	9	8.9	8.8	8.5	6.5	4.2	1.93
$\mathbf{C_L}$	2.40	2.22	2.03	1.95	1.93	1.91	1.90	1.88	1.86	1.85	1.84	1.82	1.66	1.48	1.30

In reality, the critical deployment speeds are likely to be at the higher end of this range of deployment airspeeds. Larger velocities come with reduced angle–of–attack, and vise versa, assuming a fixed landing weight and a non-accelerating flight condition typical of final approach. A plot of flight speed V and lift coefficient C_L against angle of attack α for the entire fully-deployed flight envelope at sea level conditions was made and is shown in Figure 3.16. This envelope is specifically for the case where the aircraft is at its maximum landing weight. The dotted line represents a segment of the lift polar in Figure 3.16. The solid line gives the corresponding velocity. If the dashed C_L curve is assumed to be approximately linear, the solid V curve will be a reciprocal quadratic shape, as lift coefficient proportional to $1/V^2$. Each V has a corresponding C_L, and therefore α for a fixed lift condition at the MLW. The two critical sizing cases found from Figure 3.17 are plotted as pairs of points on the two curves.

The sizing flow condition for each panel is whichever V - α pair within the deployment envelope produces the largest hinge moment. The calculations at each flow condition consisted of steady 3D simulation of the HL–CRM with a 48m cell grid provided for the 3rd High Lift Prediction Workshop [62]. This grid contained a total of 282k surface elements on the three panels. Figure 3.17 shows the hinge moments calculated for the three panels on the HL–CRM for each value of α. Each value of α was paired with a corresponding velocity that would provide lift equal to the MLW. As each α maps one-to-one with a free-stream velocity, a similar set of curves could be generated with the x-axis labels replaced by the corresponding free-stream velocity.

Solutions for $\alpha < 1.5°$ did not converge, likely due to large areas of separated flow at very low and negative angles–of–attack. There is therefore some degree of uncertainty about the true value at this angle–of–attack. As hinge moments on the two trailing edge flaps monotonically increased with decreasing angle–of–attack, curves were fitted to the data and the hinge moment value at $\alpha = -2.9°$ was estimated by extrapolation. This value corresponds to the most extreme deployment conditions of $V = 1.8\,V_{S0}$. Fitting curve equations, peak moments, and α values are given in Table 3.8. The hinge moment for the slat panel showed the surprising result of peaking at $\alpha = 9°$ and not at the flight condition corresponding to the highest dynamic pressure ($\alpha = -2.9$) as was the case with the two flap panels.

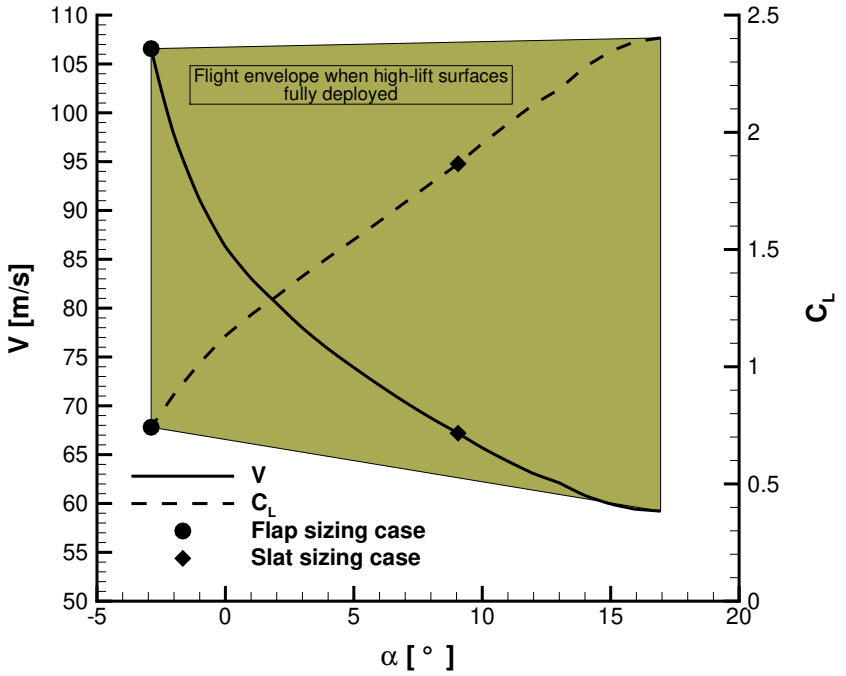

FIGURE 3.16: Range of α, V, and C_L on the HL–CRM within the fully-deployed high–lift flight envelope. The V curve is read from the left; the C_L curve is read from the left. The sizing cases for: 1) the flaps, and 2) the slat, are shown.

TABLE 3.8: Peak hinge moment values for each panel from CFD data.

Surface	**Fitting equation**	**Peak hinge moment value (kN)**	**α [°] at peak hinge moment**
Flap 1	$HM = 49.72\alpha^2 - 2283\alpha + 4.138\text{e}4$	484.4 (1.30× max converged value)	−2.9
Flap 2	$HM = 55.12\alpha^2 - 2004\alpha + 3.161\text{e}4$	38.1 (1.36× max converged value)	−2.9
Slat	$HM = 12.66\alpha^3 - 739.5\alpha^2 + 1\text{e}4\alpha - 1.428\text{e}4$	24.9 (Fully converged solution)	9.0

Because the peak moments on the two flap panels appear to occur at values for which the CFD computations did not converge, there is some considerable uncertainty about their true value. It is relatively certain that the hinge moment at this flow condition ($\alpha = -2.9°$ and $V = 107$m/s) will be the largest, as the dynamic pressure is highest and unlike the slat panel, the flaps are fairly simple. Their planar shape makes unusual non-linear effects seen on the leading edge less likely. The estimated hinge moments for Flap 1 and 2 was only ≈30% more than the largest converged value, making this extrapolation reasonable. Non-linear effects could disrupt the goodness of fit of the curve used to make this estimate and further work is required to determine this. For the purposes of the actuation weight estimation for the NASA CRM, this extrapolated value has been assumed correct and uncertainty here has not been included in the error bars for the actuation weight analysed in the next section.

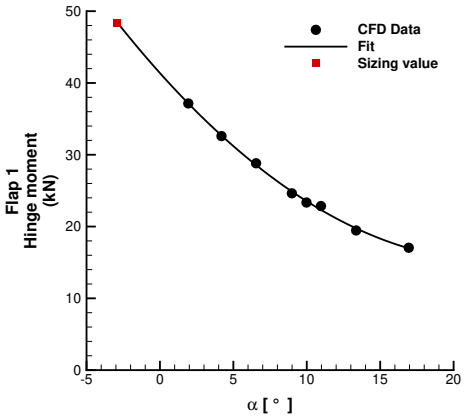

(A) Flap 1 hinge moment variation with α

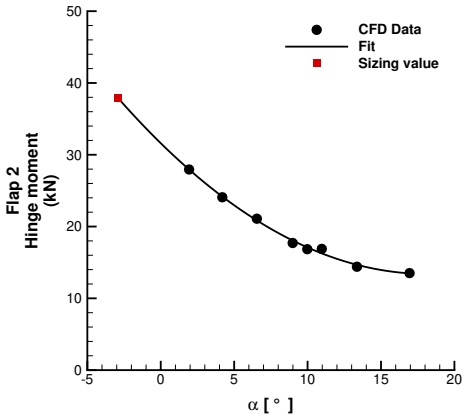

(B) Flap 2 hinge moment variation with α

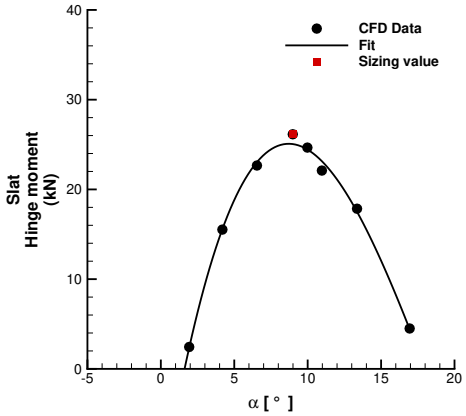

(C) Slat hinge moment variation with α

FIGURE 3.17: Variation of hinge moments with α for the three high–lift surfaces on the HL–CRM within the fully-deployed flight envelope

Actuation weight estimation

The airload data for the sizing flow condition used in the previous subsection makes it possible to estimate the weight of the high–lift actuation system on the CRM in the current configuration of one long slat panel and two flap panels. As the loads data has now been found, estimating the actuation weight of the NASA CRM becomes equivalent to estimating the actuation weight of the COMAC aircraft and the approach proceeds as outlined in Figure 3.6. The breakdown of the actuation weight for the HL-CRM is given in Table 3.9. The actuation all-up weight estimate of 411kg is on the small side for an aircraft as large as the NASA HL-CRM, though the single slat panel is unrealistic for an aircraft of this size; 6-8 is a more realistic number. Other reasons for unrealistically small estimates of the actuation system in the NASA Common Research Model could include a lack of consideration for design margins in overcoming the airload.

TABLE 3.9: Estimated actuation weight of NASA CRM based on M=0.2 condition. *The leading edge GRAs have been sized for the maximum load that they see ($\alpha = -9.0°$)

*Design point α	Actuation weight (kg)												
	Flap 1 (per wing)		Flap 2 (per wing)		TE PDU	Anc.	TE Total	Slat (per wing)		LE PDU	Anc.	LE Total	**Act. Total**
	I/B	O/B	I/B	O/B				I/B	O/B				
$-2.9°$	19.7	22.4	15.3	16.7	31.7	86.3	266	6.0	5.6	22.2	41.4	86.8	**411**

3.3 Industrial application of high–lift actuation weight estimation: Low cost vs. Low mass trade–off

3.3.1 COMAC C919

One potential application of this weight estimation method for an aircraft designer is the ability to quickly investigate design trade–offs. One example is a 'weight vs. cost' analysis on the leading edge system. On this particular aircraft, the manufacturer has opted for the all of inboard leading edge actuators to be identical, similarly with the outboard leading edge actuators. Inspection of the 'slat moments' row in Table 3.3 shows that there is almost a factor of 4 difference between the hinge moment on panel S1 (inboard) and on S5 (outboard). Sizing all leading edge actuators for the greatest load that any single one of them will experience is cost–effective from the perspective of design, testing and manufacturing because it drastically reduces the system complexity, part–count and certification overhead. However, it comes with a significant weight penalty.

By comparing the weight of a system with common leading edge actuators ('low cost') with that of one where the leading edge actuators are perfectly sized to their station loads allows an estimate of the weight penalty to be made. Figure 3.18 shows the estimated difference this makes to the weight of the actuation system (>10%) as computed by the actuation estimation method.

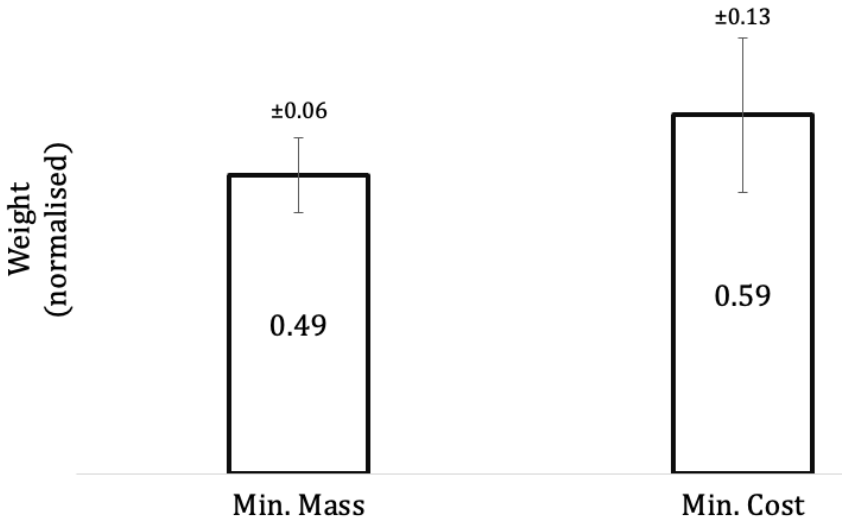

FIGURE 3.18: Normalised weight comparison for minimum mass and minimum cost leading edge systems.

As the size of the error bars scales with the total mass of GRAs, the proportional size of the error bars does not change. This weight saving represents approximately

0.25% of the wing weight of an A320-sized aircraft which has a wing structure weight of over 18,000kg [29].

3.3.2 NASA HL-CRM

The HL-CRM in its current configuration has one large slat panel running the entire length of the leading edge of the wing. In reality, this would be impractical, as the slat panel would have to be extremely heavy to be able to span the wing unsupported in the middle. There also must be breaks in the slat panel to allow for the engine nacelle, and wing flexing especially in modern, high aspect-ratio wings makes a single slat panel impossible. For comparison, the Airbus A330 and Boeing 767 have a total of 7 and 6 slat panels respectively. The Boeing 747-400 holds the record for any commercial airliner with 13 slat panels in three separate groups [49]. For this study, a maximum of five slat panels is considered. The schematic of the Boeing 777 in Figure 3.19, which is similar in size and configuration to the CRM, has a total of two flap panels and seven slat panels.

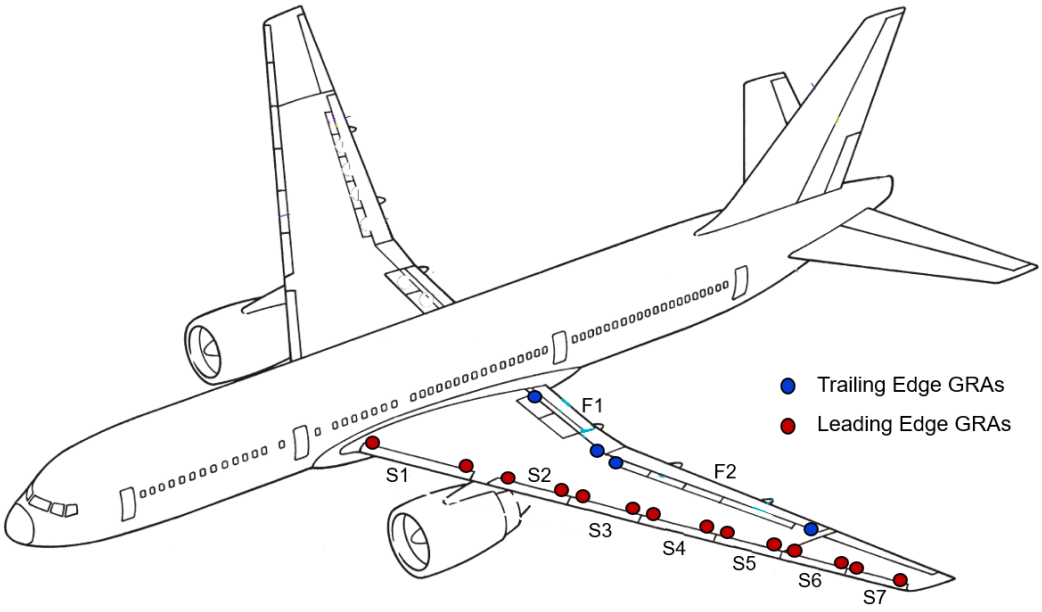

FIGURE 3.19: Schematic of high–lift surfaces on the Boeing 777 and the locations of each GRA

A slat panel design trade–off calculation can also be carried out with the HL-CRM, whereby the weight of the slat system with varying numbers of slats is evaluated for both 'low mass' and 'low cost' configurations (as described for the C919 in 3.2.1) at the sizing flow condition. Figure 3.20 shows the effect of increasing the number of panels on the force on each slat. In each case, the long slat is divided into N (≤ 8) equally sized panels but the force vectors on each diagram demonstrate that greater forces are experienced by the inboard panels. The magnitude of the difference between the two design philosophies was not as large as was seen with the COMAC C919 leading edge actuation, possibly due to the already low estimate of the actuation weight. Further industrial data is required to verify both the hinge moments and the actuation mass for a 777-sized aircraft.

As is expected, the number of slat panels increases the total leading edge actuation weight. The weight benefit of using precisely sized actuators at every track, rather

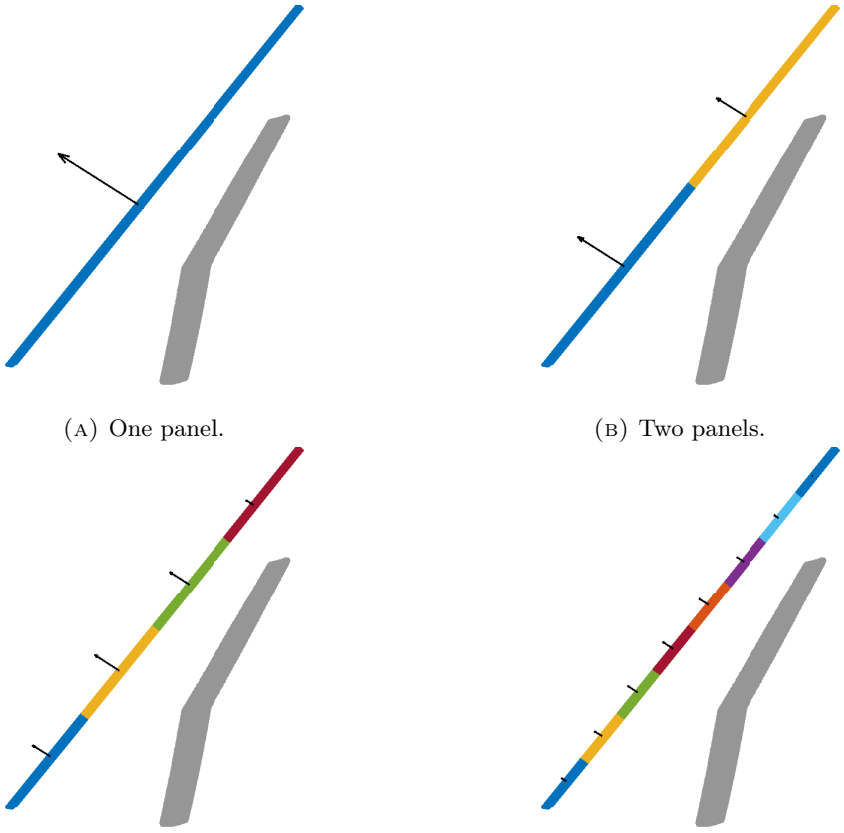

(A) One panel.

(B) Two panels.

(C) Four panels.

(D) Eight panels.

FIGURE 3.20: Visualisation of the effect of number of slat panels on panel forces. The location of the arrow on the panel indicates the resultant force location. Note the different resultant forces between each panel particularly noticeable in 3.20c and 3.20d. The summation of the smaller forces on the multi-panel leading edges add up to the single panel force in the top left.

than common I/B and common O/B actuators increases with number of panels. This effect can be seen in Figure 3.21.

For this study, the one long slat panel on the NASA HL-CRM was divided equally into N slat panels and the airloads and actuation weight for each panel calculated separately. The 'low cost' and 'low mass' comparison was then made for these equal length panels.

One of the interesting potential applications is to vary the length each panel on a multi-slat wing so that the track loads are all the same; inboard slat panels would be shorter and slat panel length would increase towards the wing tip. This would make the low cost and low mass configurations the same, and potentially saving both cost and weight. Actuation designers such as Moog generally design to a load specification provided by the customer (the aircraft manufacturer) after the slat panel sizes have been set. The actuation designers, while able to design low cost or low mass options for the customer, to not get to be part of the leading edge design process. This precludes the possibility of adjusting the size of the slat panels within the existing constraints to bring the leading edge actuation design closer to this simultaneous low cost/low mass point.

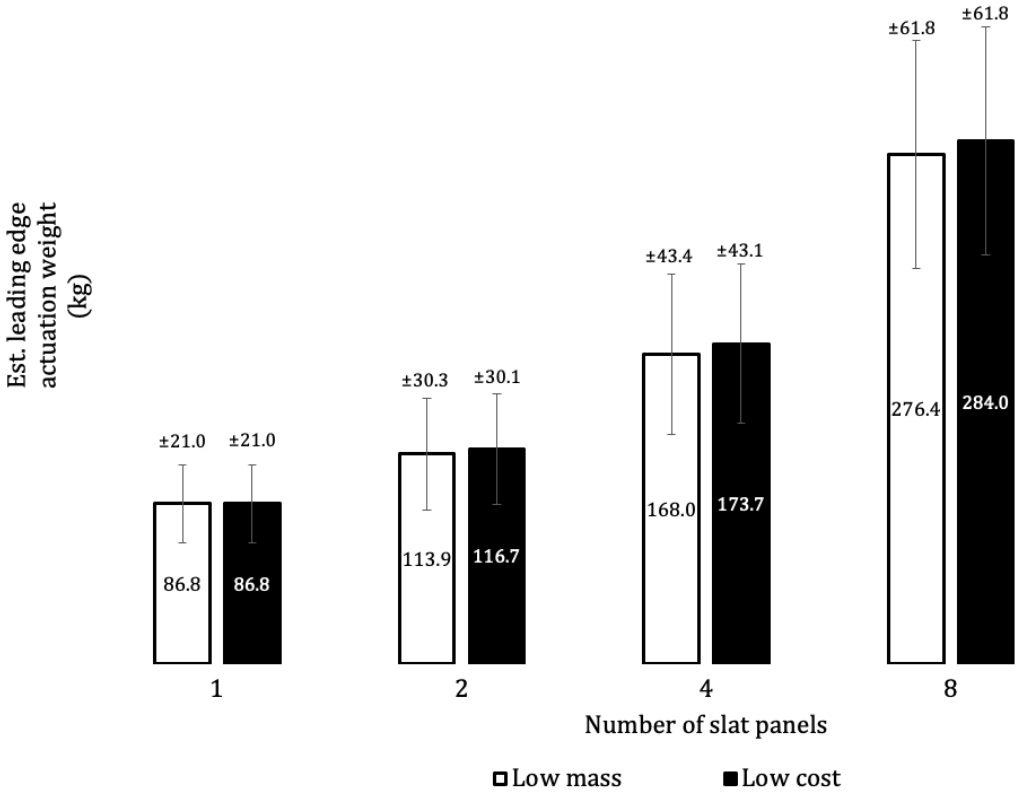

FIGURE 3.21: Effect of design case and number of slat panels on total leading edge actuation weight for the NASA HL-CRM.

3.4 Summary

This chapter has outlined the methodology developed for estimating the mass of the high–lift system. The relationship between aerodynamics and high–lift actuation design was detailed, including how the airloads that size the actuation system can be determined. Finally, the shortcomings in present methodology for estimating secondary wing weight has also been discussed.

Chapter 4

Mesh generation for 2D multi–element aerofoils

The Southampton multi–fidelity solver can speed up loads calculations on swept wings by up to two orders of magnitude compared to 3D RANS (depending on the case) and with greater accuracy than the VLM, as viscous effects are still captured [69]. Much of the expertise for its development and use is in–house at the University of Southampton [70] [71].

The 2D viscous lift polars required for the alpha-coupling loop of the Southampton multi–fidelity solver require high-quality grids, stable over a large range of angles of attack. Before this work was undertaken, lift polars generated for multi-element were of poor quality and demonstrated discontinuities in C_L regardless of the mesh fineness. An example of such a polar is given in Figure 4.1.

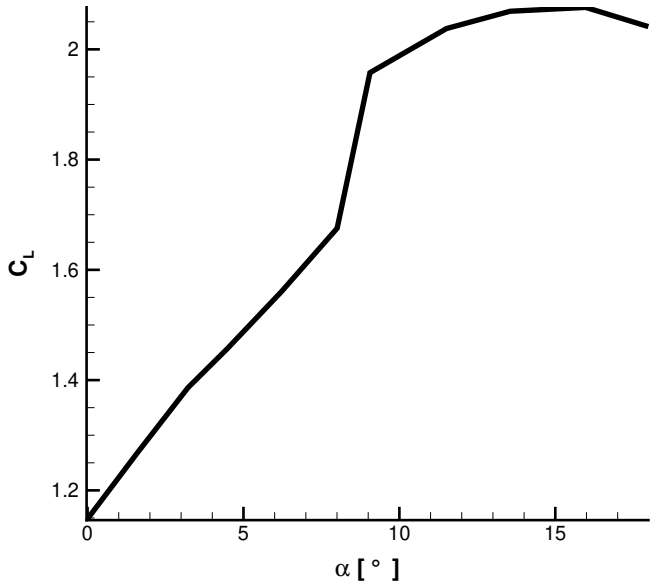

FIGURE 4.1: Non-physical C_L discontinuity seen in this section of the NASA CRM for a non-robust, pre-mesh optimisation.

To this end, an investigation on the impact of cell type, stretching ratio normal to the wall and edge length on convergence rate, computational efficiency and accuracy of the results was undertaken. Software package Pointwise [72] is used to create and modify structured, unstructured, and hybrid meshes. The anisotropic tetrahedral extrusion (T-Rex) technique for generation of boundary layer–resolving hybrid meshes

is particularly useful for investigating the effect of varying stretching ratio normal to the wall. As well as the capability of creating meshes with desired mesh parameters, Pointwise can quantify relevant aspects of mesh quality metrics such as aspect ratio, area ratio, and maximum included angle post–generation. For each mesh characteristic, a family of meshes – each with one varying mesh parameter – will be generated to create a statistically viable sample space. This will facilitate accurate conclusions about the impact of each mesh parameter, within quantifiable statistical bounds.

4.1 Geometry and flow conditions

A 2D chordwise section of the NASA high–lift Common Research Model (CRM) aircraft [66] was used as the geometry for the multi-element aerofoil meshing investigation. The flaps and slats are deployed, respectively, to 30° and 37°, and a schematic of the geometry is shown in Figure 4.2.

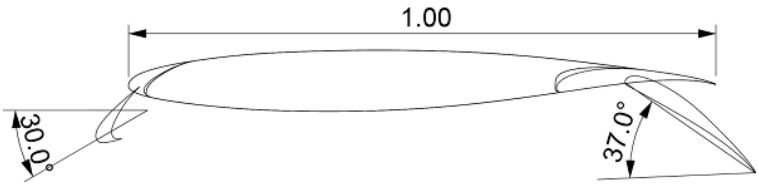

FIGURE 4.2: Schematic of a high-lift CRM wing cross–section [66].

The flow conditions used for all simulations are shown in Table 4.1.

TABLE 4.1: Flow conditions for all simulations.

Parameter	**Value**
Mach	0.2
α[°]	-2 to 24 in intervals of 2
Re	1.5×10^6
c [m]	1
T [K]	272.1
ν [kg· m^{-2}]	1.71×10^{-5}
Pr	0.72
Pr_t	0.9
γ	1.4
R [J kg^{-1} K^{-1}]	287.058
Freestream $\hat{\nu}/\nu$	3
Wall boundary condition	Adiabatic
Farfield boundary condition	Riemann Invariant
Farfield Distance	1000 c (ex. Generation 4)

4.2 Investigation Parameters

Seven different mesh parameters were investigated to assess their impact on the convergence, computational cost (CPU core hours) and solution accuracy for the multi–element aerofoil. These seven mesh parameters formed five separate mesh "families", or generations. Each of these generations contained between 12 and 15 different

meshes in which the chosen parameter or parameters under investigation in that generation were varied. Investigation parameters are outlined in more detail in the following paragraphs.

Generation 0: Mesh topology and cell type

Mesh generation took advantage of the various automation tools within Pointwise. Pointwise's anisotropic tetrahedral extrusion (T-Rex) algorithm allows user-specified growth rates of cells from the aerofoil surface, terminating when the cells approach a unity aspect ratio. These cells can be either triangles or quadrilaterals. After the T-rex algorithm has terminated – usually within one chord-length of the aerofoil surface – the remainder of the mesh to the farfield can be either triangles or quadrilaterals and be generated using one of the following methods:

- Delaunay – a point insertion technique that begins by triangulating the domain using only the boundary points. Additional points are then added to the mesh based on various quality criteria of the triangulation.
- Advancing Front (AF) – starts from the boundary discretization without triangles, and inserts points in a manner such that new layers of triangles are advanced from the boundaries to the interior of the mesh. The location of inserted points is based on cell quality, spacing between layers, and other criteria.
- Advancing Front Ortho – similar to the advancing front method, but tends to populate the domain with right-angled triangles while traditional Advancing Front and Delaunay methods tend to use equilateral triangles.

The effect of each topology algorithm for a triangular cell shape is shown in Figure 4.3.

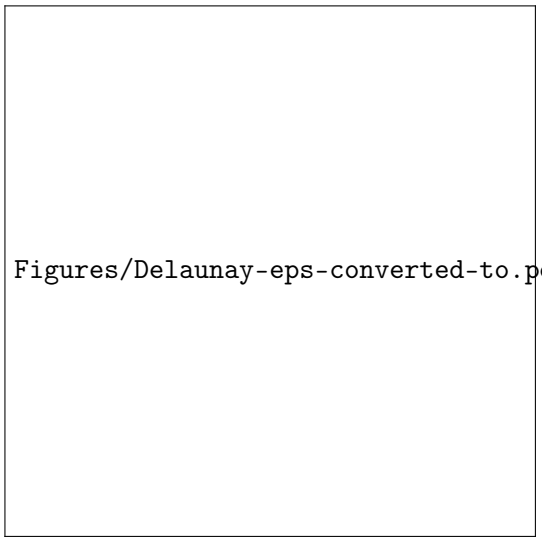

(A) Delaunay.

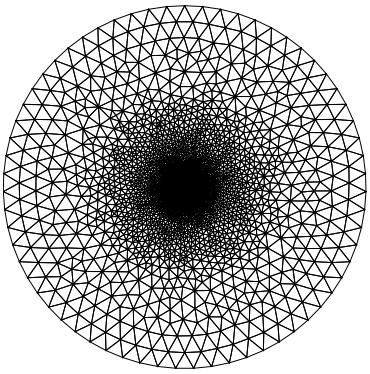

(B) Advancing front.

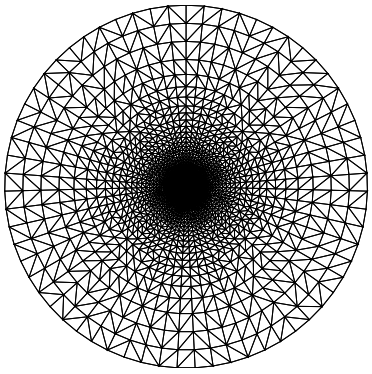

(C) Advancing front ortho.

FIGURE 4.3: The effect of three mesh topology algorithms [73].

The two T-rex cell shapes (Tri/Quad) along with the two post–T-rex cell shapes (Tri/Quad) and three algorithms (Delaunay/AF/AF ortho) create 12 possible combinations of mesh topology. These formed the initial mesh family and are given in Table 4.2.

Table 4.2: Parameter variations for generation M_00.

Mesh ID	**T-rex cell shape**	**Post–T-rex cell shape**	**Algorithm**	**Total cell count**
M_00.02	Quad	Tri	Delaunay	85,635
M_00.03	Tri	Tri	Delaunay	107,760
M_00.04	Quad	Quad	Delaunay	58,093
M_00.05	Tri	Quad	Delaunay	82,410
M_00.06	Quad	Tri	AF	76,979
M_00.07	Quad	Quad	AF	54,021
M_00.08	Quad	Tri	AF	68,065
M_00.09	Quad	Quad	AF	46,929
M_00.10	Tri	Tri	AF ortho	101,296
M_00.11	Tri	Quad	AF ortho	78,334
M_00.12	Tri	Tri	AF ortho	92,382
M_00.13	Tri	Quad	AF ortho	71,248

Generation 1: Edge length

Surface mesh average edge length was the second mesh parameter to be investigated, keeping fixed the mesh topology selected from generation 0. The average edge length value is determined for each wing element by the quantity of points on its surface and is inversely proportional to this value. The number of surface points greatly influences the total number of cells in the mesh, and consequently the computational cost. However, reducing the number of points too far compromises convergence performance and numerical stability. This generation therefore sought both the optimal number of surface mesh points and the ratio of points between the wing elements.

Edge length for each aerofoil element was determined by selecting a value for the number of points on the upper surface of that element and distributing those points between the leading and trailing edges according to a hyperbolic tangent function. The leading and trailing edge spacings took their baseline values of 9×10^{-4}m and the blunt trailing edges on each element contained three points (see Figure 4.4c). The lower surface of each element contained the same number of points as the upper surface and the flap housing always contained half as many points as the upper surface of the main element (see Figure 4.4a and 4.4b).

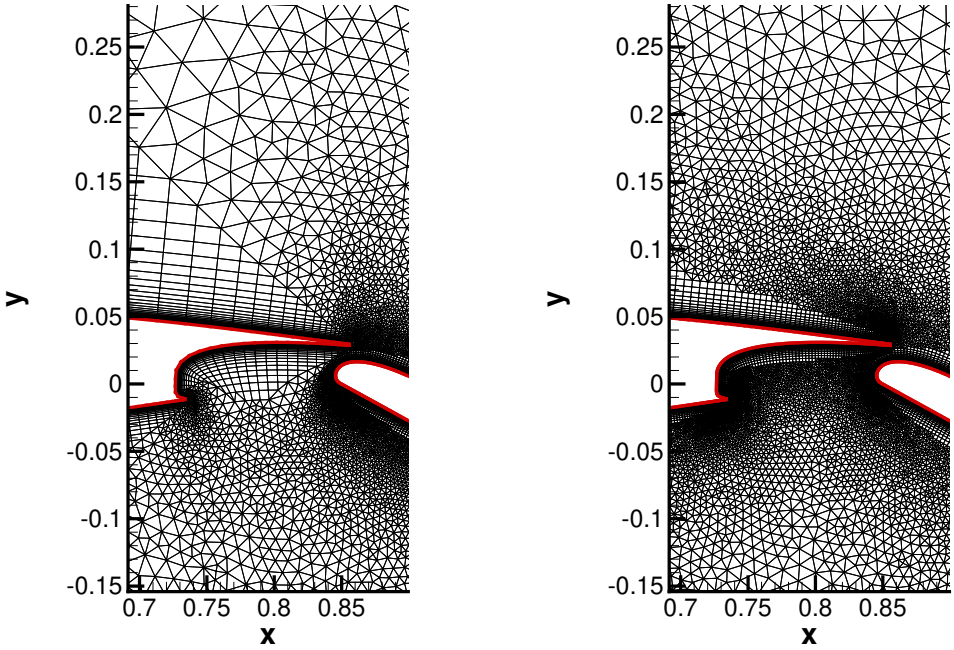

(A) Mesh M_01.12 with 58 surface points on the main element.

(B) Mesh M_01.06 with 177 surface points on the main element.

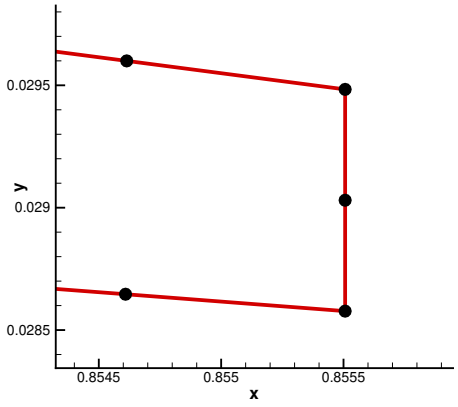

(C) Blunt trailing edge with three points.

FIGURE 4.4: Generation 1 with varying surface spacing. The flap housing always contained half as many points as the main element upper surface.

The number of points on each element could therefore be determined using Equation (4.1).

$$\begin{aligned}\text{Points on element } &= 2 \times \text{Upper surface points} \\ &\quad + \text{number of blunt TEs } + \ 0.5 \times \text{Upper surface points}^{*}\end{aligned} \tag{4.1}$$

*The last term is only relevant for the main element.

The number of points on the upper surface of each element was selected using a Latin hypercube sampling technique so that the broadest possible distribution of slat, wing and flap points were chosen. The final surface point totals for the Generation 1 mesh are given in Table 4.3.

Table 4.3: Parameter variations for generation M_01.

Mesh ID	**# surface points**			**Average surface spacing**			**Total cell count**
	Slat	Spar	Flap	Slat	Spar	Flap	
M_01.01	232	295	117	1.22×10^{-3}	5.40×10^{-3}	4.93×10^{-3}	70,180
M_01.02	122	432	315	2.36×10^{-3}	3.67×10^{-3}	1.80×10^{-3}	89,047
M_01.03	80	275	201	3.66×10^{-3}	5.81×10^{-3}	2.84×10^{-3}	63,388
M_01.04	110	405	257	2.62×10^{-3}	3.92×10^{-3}	2.21×10^{-3}	81,057
M_01.05	50	172	349	6.04×10^{-3}	9.38×10^{-3}	1.63×10^{-3}	64,175
M_01.06	154	445	223	1.85×10^{-3}	3.56×10^{-3}	2.56×10^{-3}	85,255
M_01.07	86	180	73	3.39×10^{-3}	8.96×10^{-3}	8.04×10^{-3}	44,328
M_01.08	164	375	265	1.74×10^{-3}	4.24×10^{-3}	2.15×10^{-3}	83,782
M_01.09	220	232	331	1.29×10^{-3}	6.90×10^{-3}	1.72×10^{-3}	81,723
M_01.10	204	332	155	1.39×10^{-3}	4.79×10^{-3}	3.70×10^{-3}	74,384
M_01.11	132	237	207	2.17×10^{-3}	6.75×10^{-3}	2.76×10^{-3}	65,002
M_01.12	146	147	293	1.96×10^{-3}	1.10×10^{-2}	1.94×10^{-3}	65,637
M_01.13	202	197	173	1.41×10^{-3}	8.16×10^{-3}	3.31×10^{-3}	64,365
M_01.14	188	357	83	1.51×10^{-3}	4.45×10^{-3}	7.03×10^{-3}	68,704
M_01.15	60	317	125	4.97×10^{-3}	5.02×10^{-3}	4.61×10^{-3}	58,554

Generation 2: Leading/Trailing edge spacing

High gradient areas of flow occur at the leading edge (LE) and trailing edges (TE) and concentrating points at these locations is therefore good practice. Generation 2 used the superior mesh topology and edge length values from Generations 0 and 1, respectively. Generations 0 and 1 used a baseline value of 9×10^{-4}. Six different LE/TE spacings were used: 1×10^{-4}, 3.0×10^{-4}, 5.0×10^{-4}, 7×10^{-4}, 1.1×10^{-3} and 1.3×10^{-3}. The leading edge spacing was always the same as the trailing edge spacing.

Once again, the combinations of these that made up each mesh came from Latin hypercube sampling and are summarised in Table 4.4.

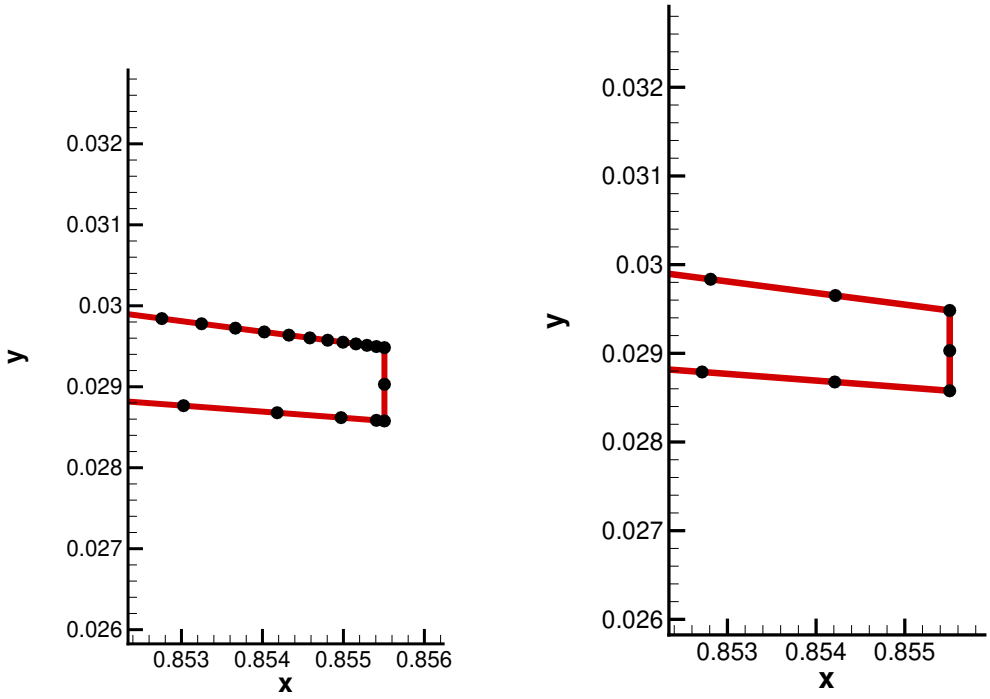

(A) Mesh M_02.01: TE spacing = $\mathbf{1 \times 10^{-4}}$m.

(B) Mesh M_02.10: TE spacing = $\mathbf{1.3 \times 10^{-3}}$.

FIGURE 4.5: Trailing edge of main element of two meshes of the M_02 family.

TABLE 4.4: Parameter variations for generation M_02.

Mesh ID	LE/TE spacing			Total cell count
	Slat	Spar	Flap	
M_02.01	1.00×10^{-4}	1.00×10^{-4}	1.00×10^{-4}	81,541
M_02.02	3.00×10^{-4}	3.00×10^{-4}	3.00×10^{-4}	81,669
M_02.03	5.00×10^{-4}	5.00×10^{-4}	5.00×10^{-4}	81,262
M_02.04	7.00×10^{-4}	7.00×10^{-4}	7.00×10^{-4}	81,517
M_02.05	1.10×10^{-3}	1.10×10^{-3}	1.10×10^{-3}	81,716
M_02.06	1.30×10^{-3}	1.30×10^{-3}	1.30×10^{-3}	81,732
M_02.07	3.00×10^{-4}	5.00×10^{-4}	1.30×10^{-3}	81,678
M_02.08	1.00×10^{-4}	3.00×10^{-4}	5.00×10^{-4}	81,692
M_02.09	7.00×10^{-4}	1.00×10^{-4}	1.10×10^{-3}	81,183
M_02.10	1.00×10^{-4}	1.30×10^{-3}	1.00×10^{-4}	81,648
M_02.11	5.00×10^{-4}	1.30×10^{-3}	1.10×10^{-3}	81,623
M_02.12	1.10×10^{-3}	3.00×10^{-4}	3.00×10^{-4}	81,427
M_02.13	5.00×10^{-4}	7.00×10^{-4}	7.00×10^{-4}	81,552
M_02.14	1.10×10^{-3}	1.10×10^{-3}	3.00×10^{-4}	81,733
M_02.15	1.30×10^{-3}	5.00×10^{-4}	1.10×10^{-3}	81,316

Generation 3: Number of constant height surface cells and initial growth rate normal to wall

For all meshes excluding the M_03 family, a growth rate (or cell stretching ratio normal to the wall) of 1.2 was chosen, with initial cell height at the wall, $y = 6 \times$

10^{-6}m. This corresponded to a y^+ value for the first cell of close to 1, calculated using Equations (4.2) and (4.3). More information can be found in [74] and [75].

$$y = \frac{y^+ \mu}{\rho u_*}, \tag{4.2}$$

where

$$u_* = \sqrt{\frac{C_f \cdot \frac{1}{2}U^2}{\rho}}, \qquad \text{and} \qquad C_f \approx [2log_{10}(Re) - 0.65]^{-2.3} \text{ for } Re < 10^9 \tag{4.3}$$

The values of Re and μ are given directly in Table 4.1, while ρ and U can be calculated indirectly from the Reynolds and Mach numbers, respectively.

Proper boundary layer resolution is essential for accurate solutions. At the same time, dense boundary layer-resolving cells near the surface have a large effect on the total number of cells in a mesh, and therefore adversely affect computational cost. Generations 0, 1, 2, and 4 used a single layer of surface cells of thickness y^+, as calculated using Equation (4.2). The cells then grew outwards from the surface at a rate of 1.2 with each subsequent cell layer 20% taller than the previous. Pointwise's T-rex algorithm would terminate the growth once unity aspect ratio was reached by all cells.

Faster growth rates mean a smaller number of cell layers until unity aspect ratio, but compromise solution accuracy and convergence if too large. It was hypothesized that preventing the cells from growing for a fixed number of layers might allow a larger growth rate afterwards and produce an overall more efficient mesh. In this generation, the effect of keeping cell height fixed for 15, 20, 40 and 50 layers each with subsequent growth rates of 1.1, 1.2 and 1.3 was investigated as shown in Table 4.5.

Table 4.5: Parameter variations for generation M_03.

Mesh ID	**# const. height surface cells**	**Growth rate**	**Total cell count**
M_03.01	15	1.1	108,973
M_03.02	20	1.1	112,531
M_03.03	40	1.1	127,800
M_03.04	50	1.1	135,293
M_03.05	15	1.2	92,848
M_03.06	20	1.2	96,531
M_03.07	40	1.2	111,606
M_03.08	50	1.2	119,137
M_03.09	15	1.3	87,548
M_03.10	20	1.3	91,155
M_03.11	40	1.3	106,291
M_03.12	50	1.3	113,790

A visual comparison of mesh M_03.01 with mesh M_03.09 is shown in Figure 4.6. The aerofoil surface is indicated by a thick red line and the constant height layers can be seen above it. The effect of the different growth rates are extremely apparent in the height of the last layer of cells at the top of the subfigures.

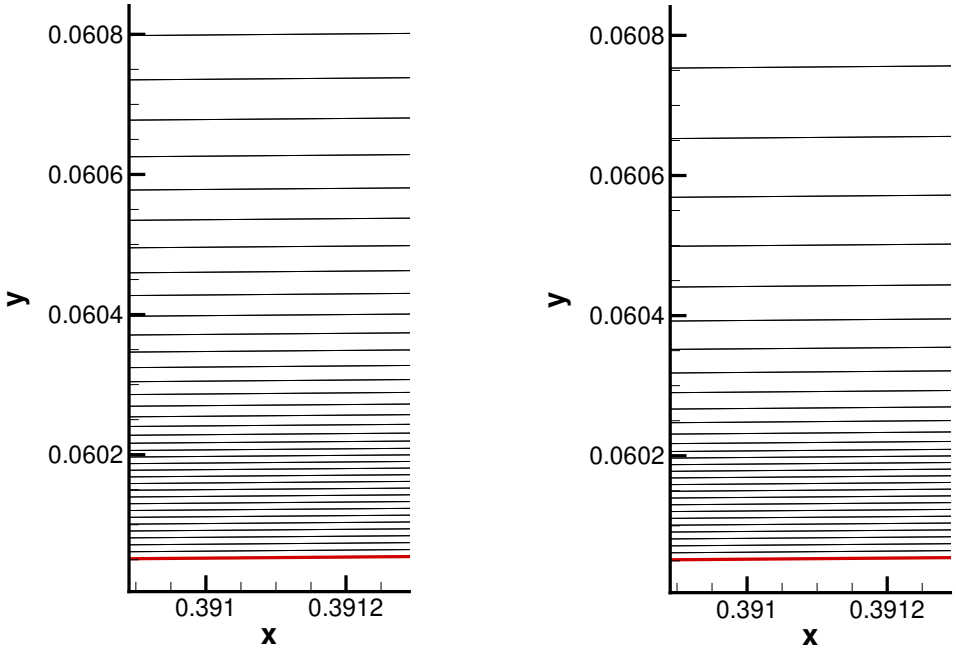

(A) Mesh M_03.01: Number constant height surface cells = 15. Growth rate = 1.1.

(B) Mesh M_03.09: Number constant height surface cells = 15. Growth rate = 1.3.

FIGURE 4.6: Aerofoil surface showing 15 constant–height cells and subsequent growth rates of 1.1, 1.3.

Generation 4: Effect of farfield distance

With the exception of the farfield boundary distance investigation (M_04), the farfield boundary for all of the meshes was set at 1000c, as recommended in the call for papers. All meshes had 64 equally spaced points at the farfield boundary. In Generation 4, the farfield distance was varied to quantify its effect on the results. For the farfield boundary investigation in Generation 4, 12 different boundary distances were used as given in Table 4.6.

TABLE 4.6: Parameter variations for generation M_04.

Mesh ID	**Farfield distance**	**Total cell count**
M_04.01	800c	80,927
M_04.02	600c	80,089
M_04.03	400c	79,499
M_04.04	200c	77,933
M_04.05	100c	76,453
M_04.06	80c	75,815
M_04.07	60c	75,299
M_04.08	40c	74,395
M_04.09	20c	72,865
M_04.10	10c	71,047
M_04.11	5c	69,303

4.3 Mesh Performance Assessment

Each subsequent generation kept fixed those parameters from the best performing mesh of the previous generation, with only the parameter/s under investigation in latest generation allowed to vary. This is somewhat similar to a genetic algorithm, although traditional genetic algorithms can vary any and all of the investigation parameters being studied. Proper assessment of the best–performing mesh from each family was therefore required. Superior performance of a mesh at one angle–of–attack was not sufficient, with convergence and computational performance for the entire α–sweep being assessed. This ensured selection of a robust mesh, instead of one which outperformed only at selected α's.

Selection of the mesh was first done by comparing the convergence performance of each mesh in that generation across a range of angles of attack. An example of the convergence plot for one of generation M_02 is shown in Figure 4.7. Each mesh was used to run 15 different angles–of–attack from -2 to 24° in increments of 2°. The first 10 angles (-2 - 16°) of each polar were used to create a box–and–whisker plot of the number of iterations it took to reach the convergence criterion or the iteration limit, whichever came first. In this box plot, the median number of iterations taken to reach convergence for the pre–stall angles–of–attack are given by the red line, all but the highest and lowest iteration iteration values fit in range indicated by the blue box (the interquartile range). The highest and lowest convergence values are indicated by the tails.

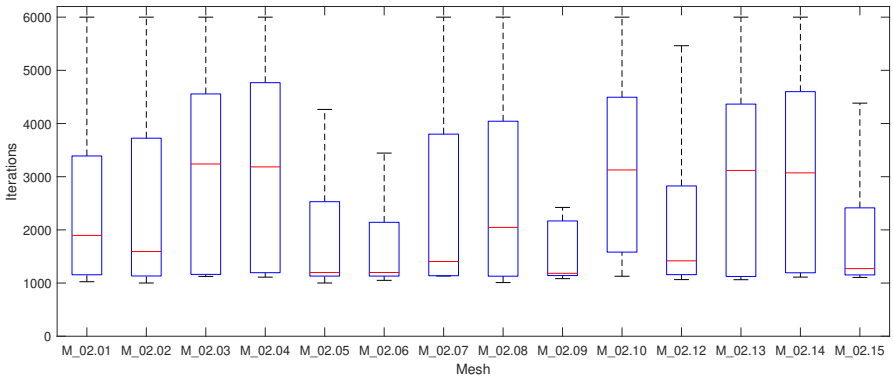

FIGURE 4.7: Convergence performance for the M_02 mesh family for angles of attack varying from $-2°$ to $16°$.

The maximum number of iterations was set to 6,000, and meshes which reached Cauchy convergence criterion of 1×10^{-7} in all of the pre–stall α ($< 18°$) were given a "Green" convergence rating. Those meshes which had at least one pre–stall angle fail to reach the convergence criteria before the iteration limit were rated "Amber" and those which demonstrated numerical instability (producing NaNs) for any angle–of–attack were rated "Red". Figure 4.7 shows nine Amber meshes with a tail on the 6,000 iteration line (M_02.01–04, M_02.07–08, M_02.10, M_02.13–14), five Green meshes for which convergence was reach for all angles $< 18°$ (M_02.05-06, M_02.09, M_02.12, M_02.15). One mesh (M_02.11) failed to converge and was rated Red. As they failed to converge, these meshes to not feature in either the convergence nor computational box–and–whisker plots.

The Green–rated meshes were then compared based on computational performance. If the family did not produce any Green meshes, the Amber meshes were compared instead. A mesh which requires few iterations to converge may not outperform others if each iteration is more computationally expensive. A computational cost comparison was made by multiplying the wall clock convergence time for single angle of attack took by the number of cores used. This quantity of interest is shown in Figure 4.8. This time, all angles (-2 - $24°$) were used to make each box. Mesh M_02.09 has the smallest median, maximum and interquartile range of computational time and was therefore deemed the superior performing mesh for this family.

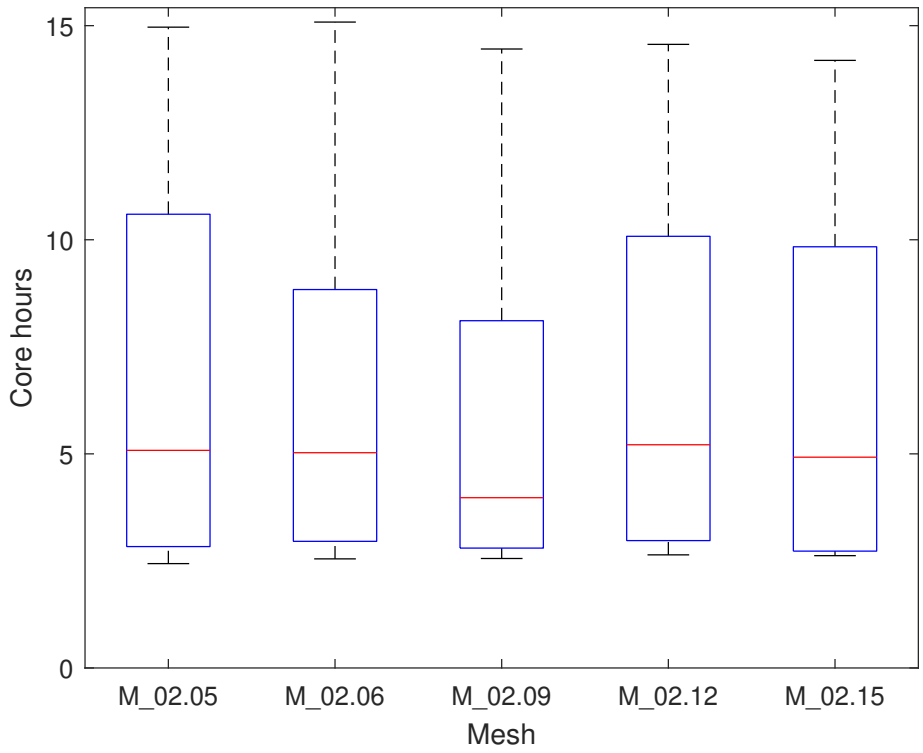

FIGURE 4.8: Computational performance over the entire polar for the M_02 mesh family.

4.4 Results

The Green, Amber and Red ratings for each mesh across the generations is summarized in Figure 4.9. The curly braces indicate which mesh was used to create the next family. Although it was the best performing mesh from generation M_03, M_03.05 did not outperform M_02.09. M_02.09 therefore was used to make both the M_03 and M_04 mesh families. The top-level results are presented here, and the results for each mesh family are outlined in more detail in Sections 4.4.1-4.4.5.

Meshes M_00.02, M_01.09, M_02.09, M_03.05 and M_04.07 were the best performing meshes from their respective families as assessed using the selection criteria outlined in Section 4.3. Figure 4.10 shows the convergence and computational performance for these meshes. The number of iterations taken to reach convergence did not improve on average, and even got worse. However, computational performance improved dramatically through the study. Median core hours taken for each simulation to reach the convergence criteria convergence limit went reduced by nearly a factor of 4, as seen in . Robustness, as determined by the variation in number of iterations to reach convergence (length of box) also reduced dramatically.

The lift polar and separation location for the main element are shown in Figure 4.11. Separation location is determined by locating the position where the skin friction coefficient, c_f, becomes 0.

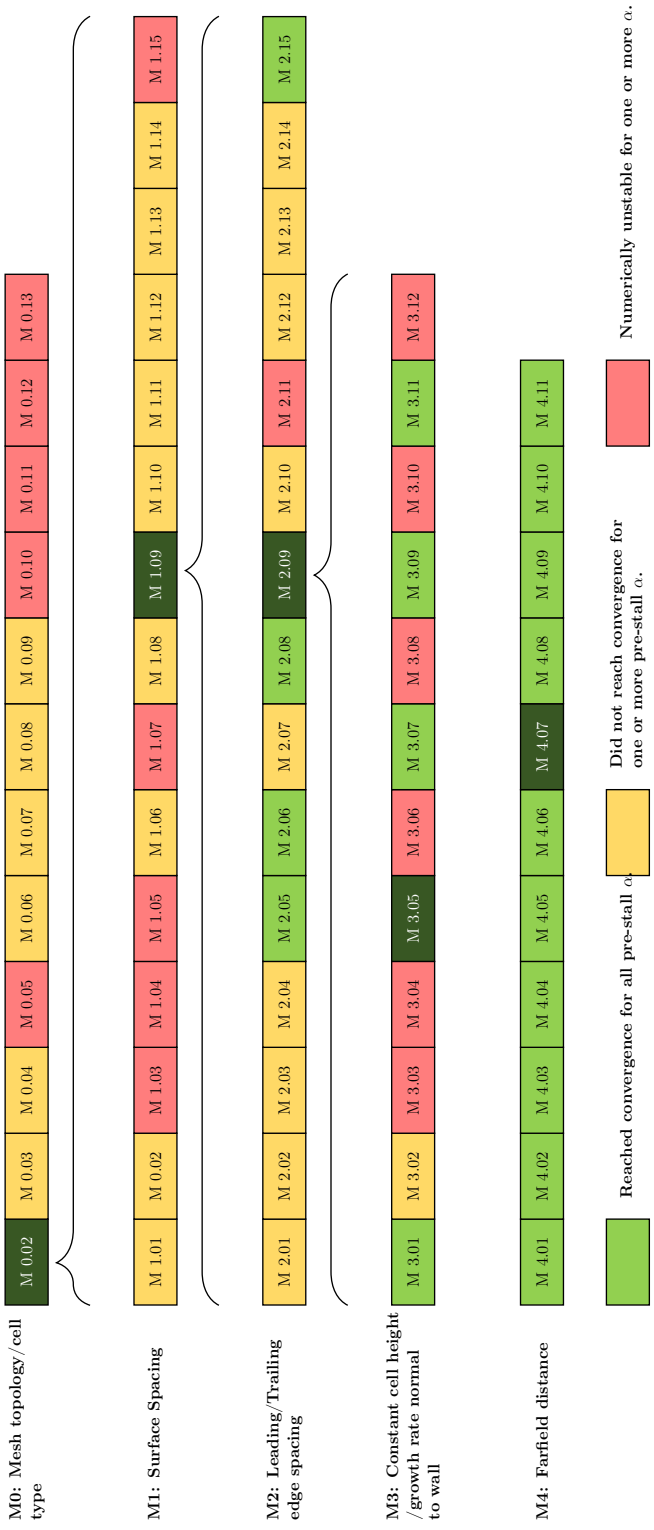

FIGURE 4.9: Mesh performance summary using the colour code outlined in Section 4.3.

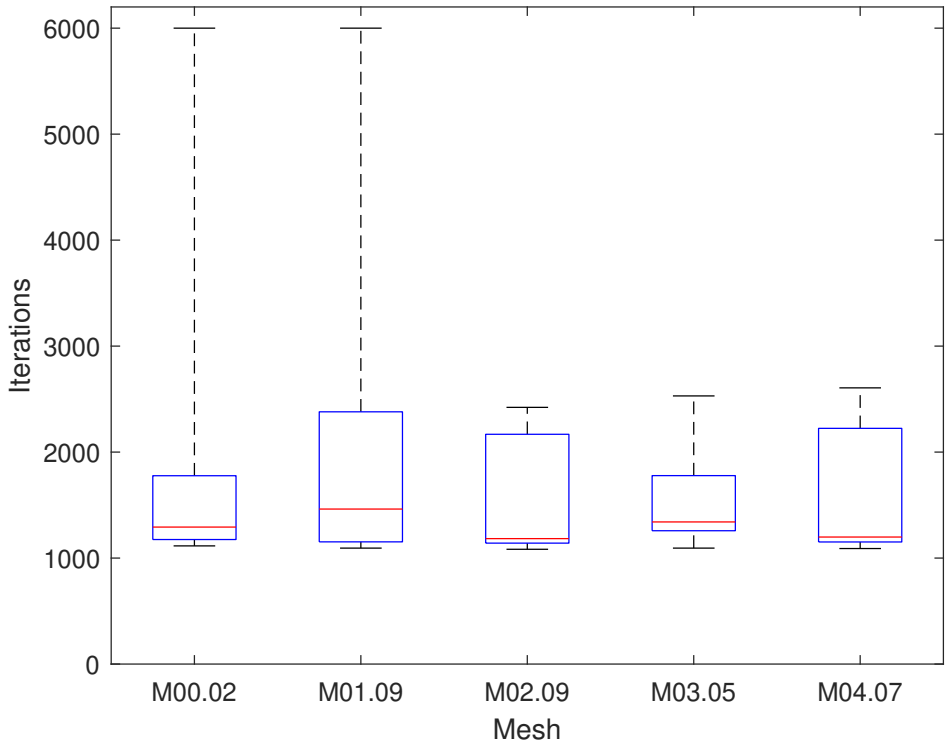

(A) Convergence scores.

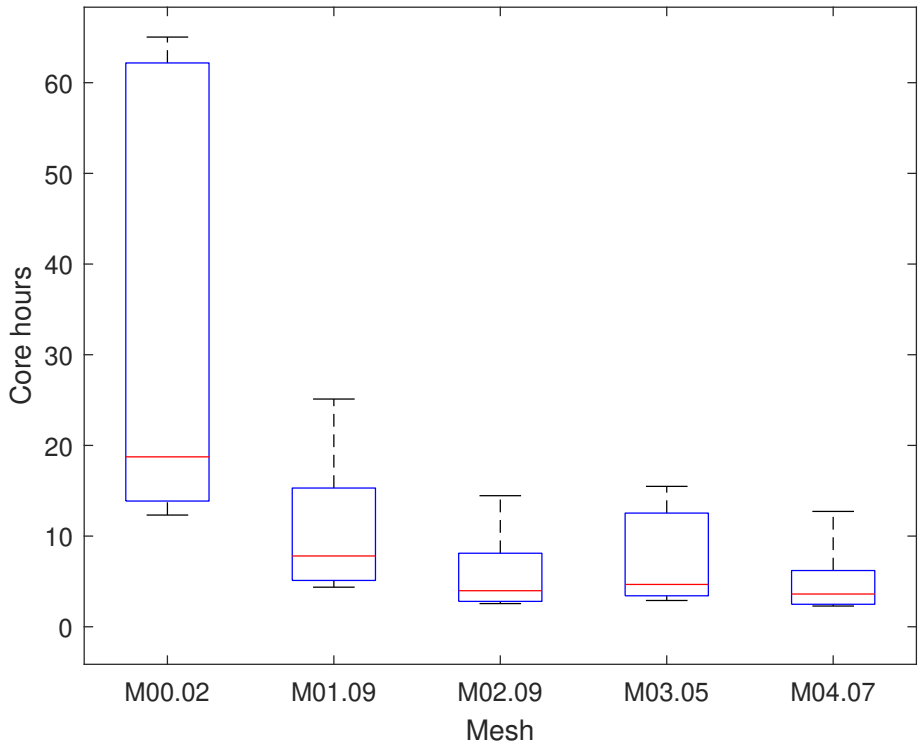

(B) Computational performance.

FIGURE 4.10: Comparison of convergence score and computational cost for the best mesh of each generation.

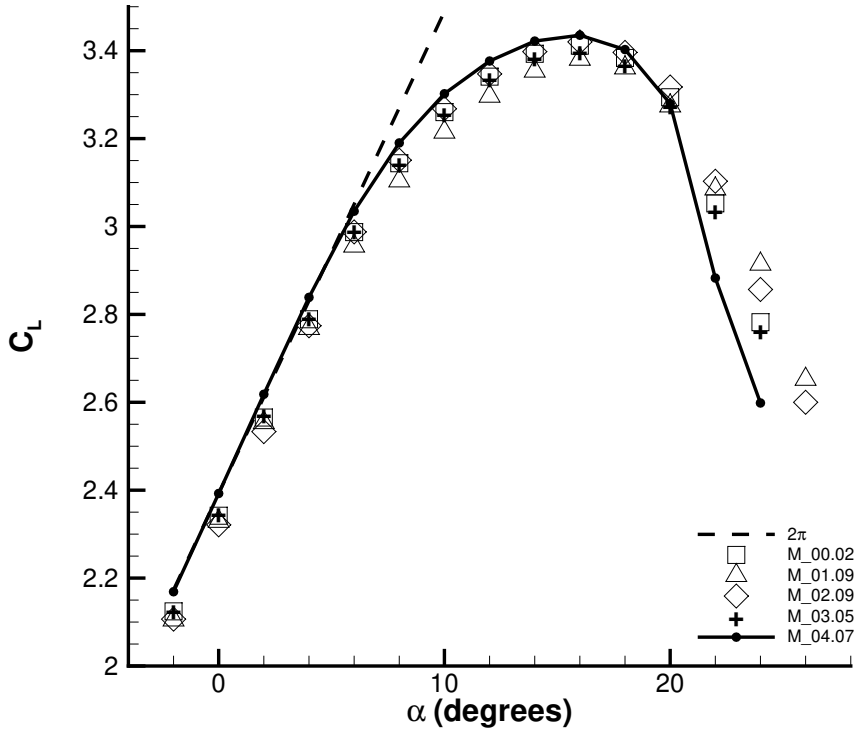

(A) Lift coefficient

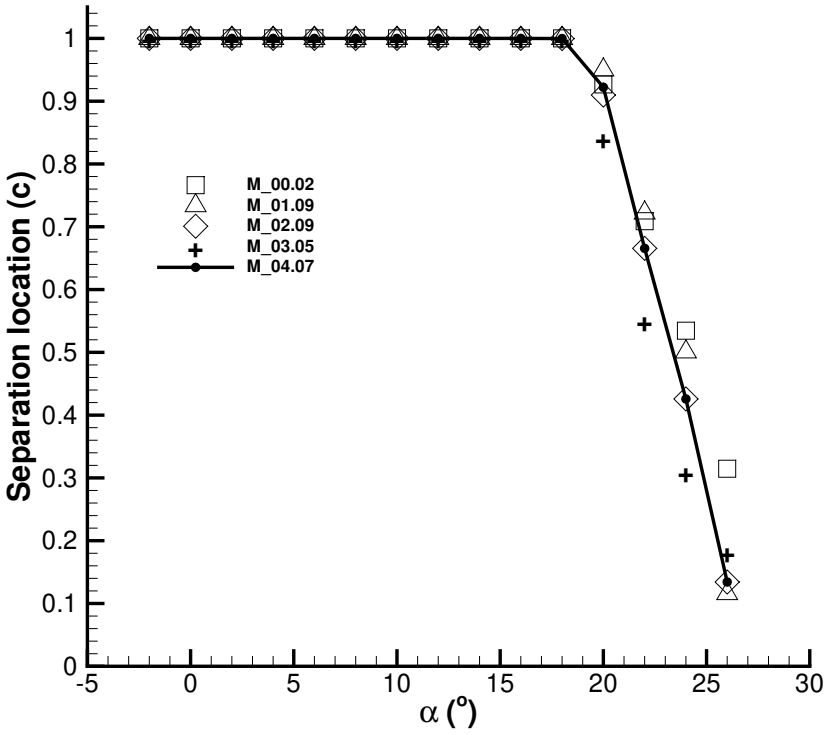

(B) Separation point

FIGURE 4.11: Lift polar and separation location variation with angle–of–attack for the best meshes from each generation.

4.4.1 Generation 0: Mesh topology and cell type

None of the polars from the M_0 generation were rated green because none of the meshes had all ten pre-stall α's reach the convergence criterion before the iteration limit. Instead the box–and–whisker plot for convergence was performed on the first nine angles ($-2°$ to $14°$) and M_00.02 and M_00.08 were found to be the most robust (see Figure 4.12). The computational comparison was therefore performed on the Amber meshes. Mesh M_00.02 was selected. It had a a quadrilateral T-rex surface mesh and a Delaunay triangle outer mesh as summarised in Table 4.7, from the M_00 reference data in 4.2.

TABLE 4.7: M_00.02: Best-performing mesh from the M_00 family.

Mesh ID	T-rex cell shape	Post–T-rex cell shape	Algorithm	Total cell count
M_00.02	Quad	Tri	Delaunay	85,635

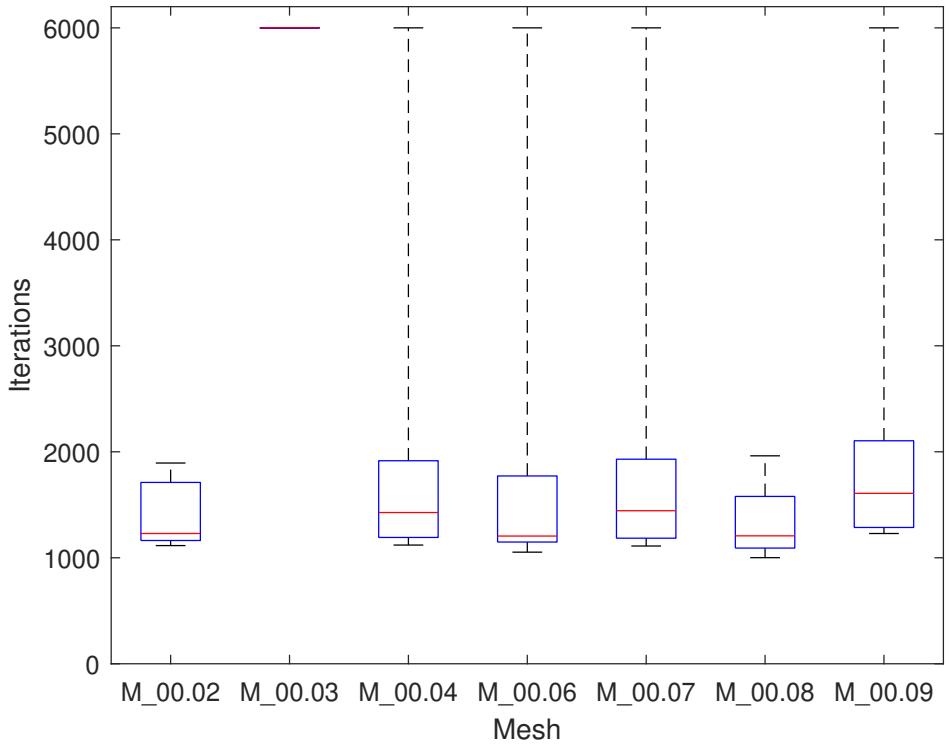

FIGURE 4.12: Comparison of convergence score for the M_00 mesh family (first 9 polar angles only).

The lift polars for the M_00 family contain a significant spread for $\alpha >= 6°$, especially post-stall. This is shown in Figure 4.13. The spread was reduced considerably in following generations.

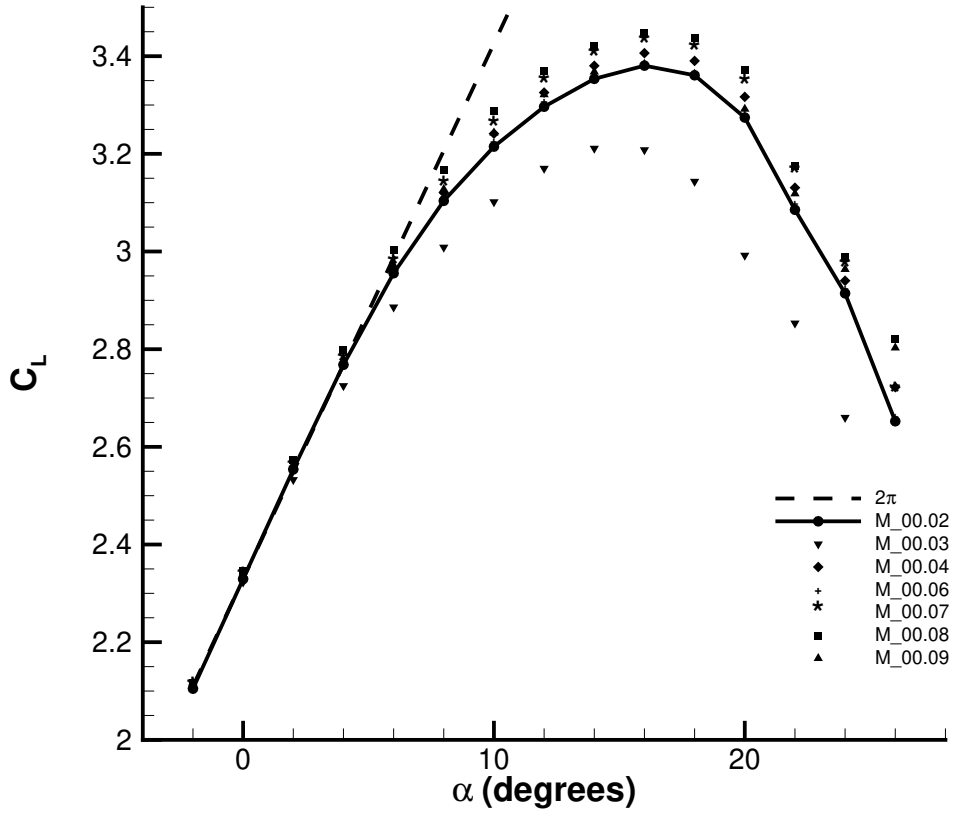

FIGURE 4.13: Polar for the M_00 mesh family. The solid line forms the polar of the superior mesh.

4.4.2 Generation 1: Edge length

Like the M_00 mesh family, M_01 did not have any meshes meet the Green convergence standard. The convergence box–and–whisker plot is shown in Figure 4.14a. The computational cost comparison was performed on these Amber meshes. M_01.09 was the best converging mesh with a median iteration number at convergence of ≈ 1500, significantly lower than the other meshes. M_01.09 was also the superior mesh in terms of computational performance with the lowest median core hours to reach convergence criterion or iteration limit. M_01.09 had a significant number of mesh points on the surface of all of the wing elements compared to the other meshes, with the largest number on the flap. This is summarised in Table 4.8, from the M_01 reference data in Table 4.3.

TABLE 4.8: M_01.09: Best-performing mesh from the M_01 family.

Mesh ID	**# surface points**			**Average surface spacing**			**Total cell count**
	Slat	Spar	Flap	Slat	Spar	Flap	
M_01.09	220	232	331	1.29×10^{-3}	6.90×10^{-3}	1.72×10^{-3}	81,723

The lift polars for the M_01 family are shown in Figure 4.15. These also contain a significant degree of spread, but not until about $\alpha >= 10°$.

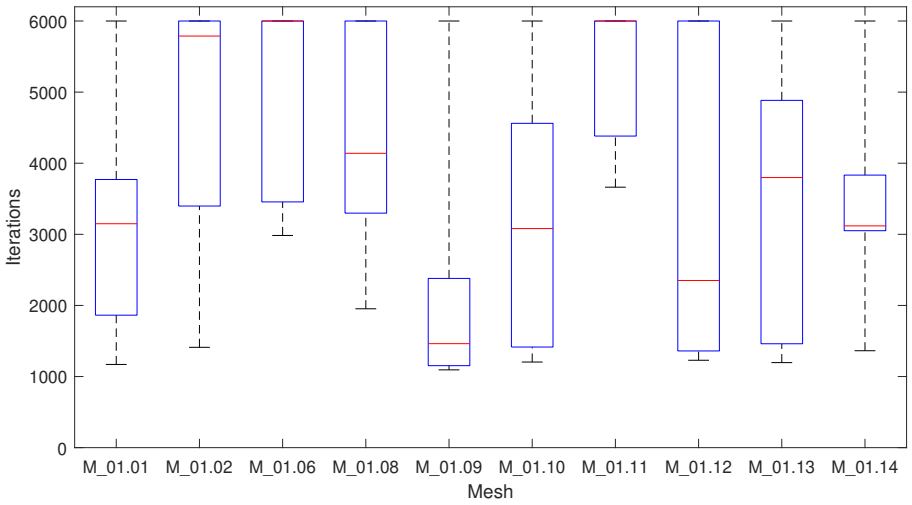

(A) Convergence scores.

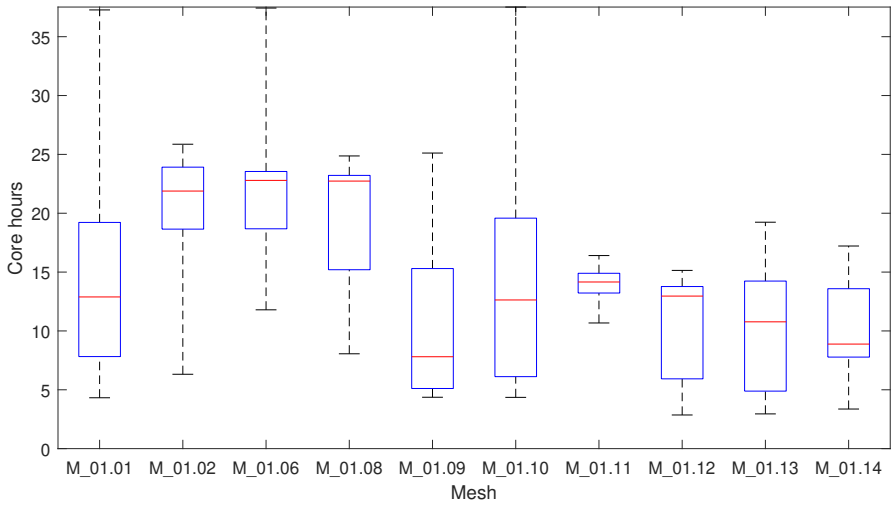

(B) Computational performance.

FIGURE 4.14: Comparison of convergence score and computational cost for the M_01 mesh family.

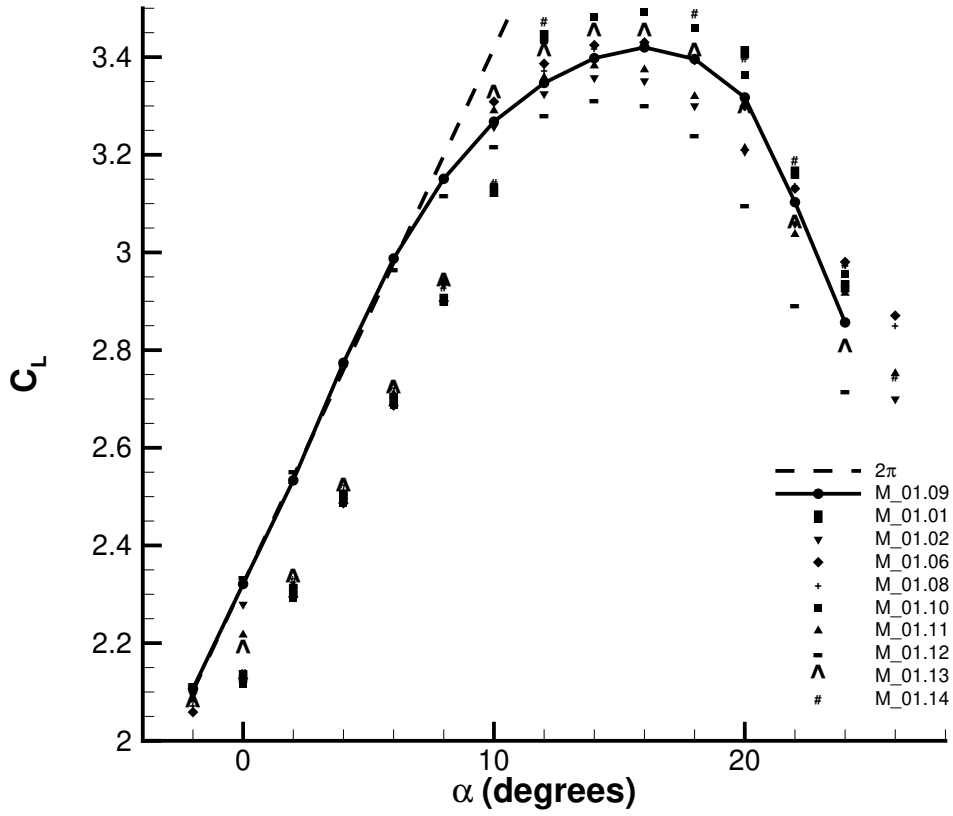

FIGURE 4.15: C_L polars for the M_01 mesh family. The solid line forms the polar of the superior mesh.

4.4.3 Generation 2: Leading/Trailing edge spacing

The M_02 mesh family had five Green convergence–standard meshes: M_02.05-06, M_02.09, M_02.12, M_02.15. The convergence box–and–whisker plot is shown in Figure 4.16. The computational cost comparison is shown in Figure 4.17. M_02.09 was the best converging mesh with a median iteration number at convergence of ≈ 1500. M_02 .09 was also the superior mesh in terms of computational performance with the lowest median core hours to reach convergence criterion or iteration limit. M_02.09 had a fairly large leading and trailing edge spacing on the slat and flap, but a small spacing for the main element. This is summarised in Table 4.9, from the M_02 reference data in Table 4.4.

TABLE 4.9: M_02.09: Best-performing mesh from the M_02 family.

Mesh ID	**LE/TE spacing**			**Total cell count**
	Slat	**Spar**	**Flap**	
M_02.09	7.00×10^{-4}	1.00×10^{-4}	1.10×10^{-3}	81,183

With the exception of some outlier points in the lower angles–of–attack, the M_02 polars shown in Figure 4.18 demonstrate much better agreement with each other than the earlier two generations, especially post–stall.

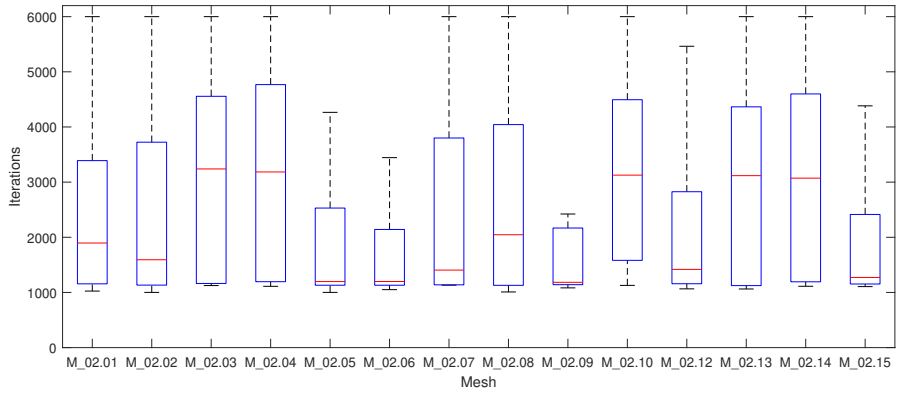

FIGURE 4.16: Convergence performance for the M_02 mesh family for angles of attack varying from $-\mathbf{2}^\circ$ to $\mathbf{16}^\circ$.

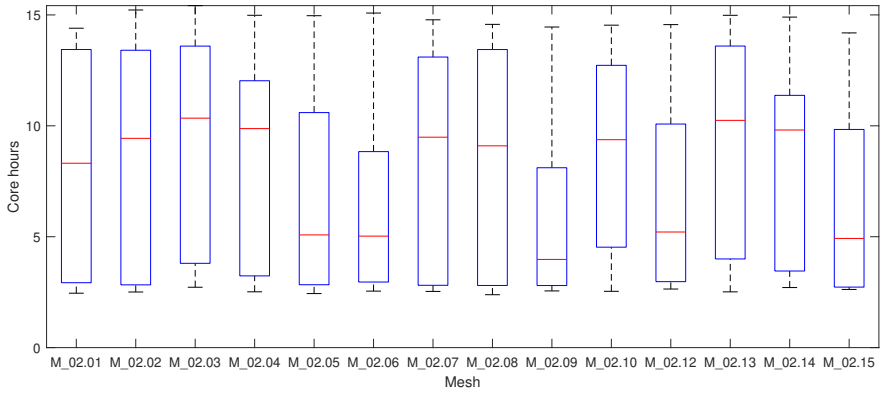

FIGURE 4.17: Computation performance for the entire polar of the best–converging meshes of the M_02 family.

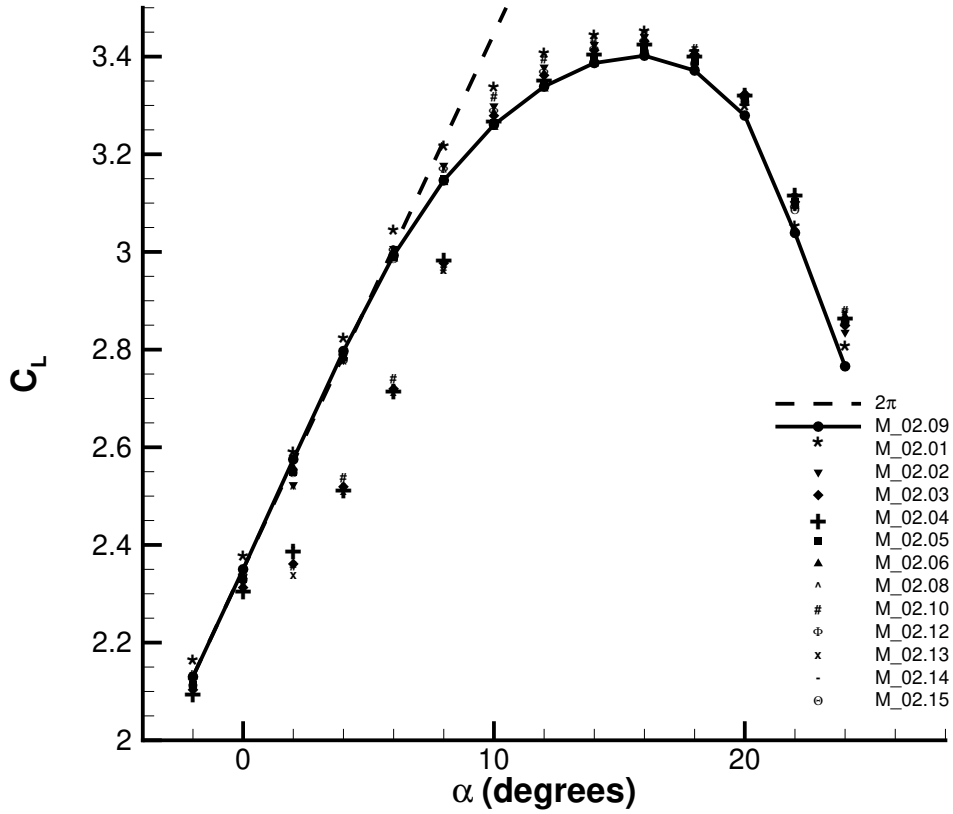

FIGURE 4.18: C_L polars for the M_02 mesh family. The solid line forms the polar of the superior mesh.

4.4.4 Generation 3: Number of constant height surface cells and initial growth rate normal to wall

The M_03 mesh family had five Green convergence–standard meshes: M_03.01-02, M_03.05, M_03.07, M_03.11. The convergence box–and–whisker plot is shown in Figure 4.19a. The computational cost comparison is shown in Figure 4.19b. M_03.05

was the best converging mesh with a median iteration number at convergence of ≈ 1400. M_03.05 was also the superior mesh in terms of computational performance with the lowest median core hours to reach convergence criterion or iteration limit. M_03.05 had 15 constant–height cells at the wall and a growth rate of 1.2. Table 4.10 provides the mesh data for this mesh, and is taken from the M_03 reference in Table 4.5.

TABLE 4.10: M_03.05: Best-performing mesh from the M_03 family.

Mesh ID	**# const. height surface cells**	**Growth rate**	**Total cell count**
M_03.05	15	1.2	92,848

It is not unexpected that the lift polars for the farfield boundary were almost superimposed on top of each other, with the only outliers being from the meshes with extremely small farfield distances. This polar is shown in Figure 4.22.

With the exception of the post-stall region, the polars from the M_03 family of meshes showed good agreement with each other. This can been seen in Figure 4.20.

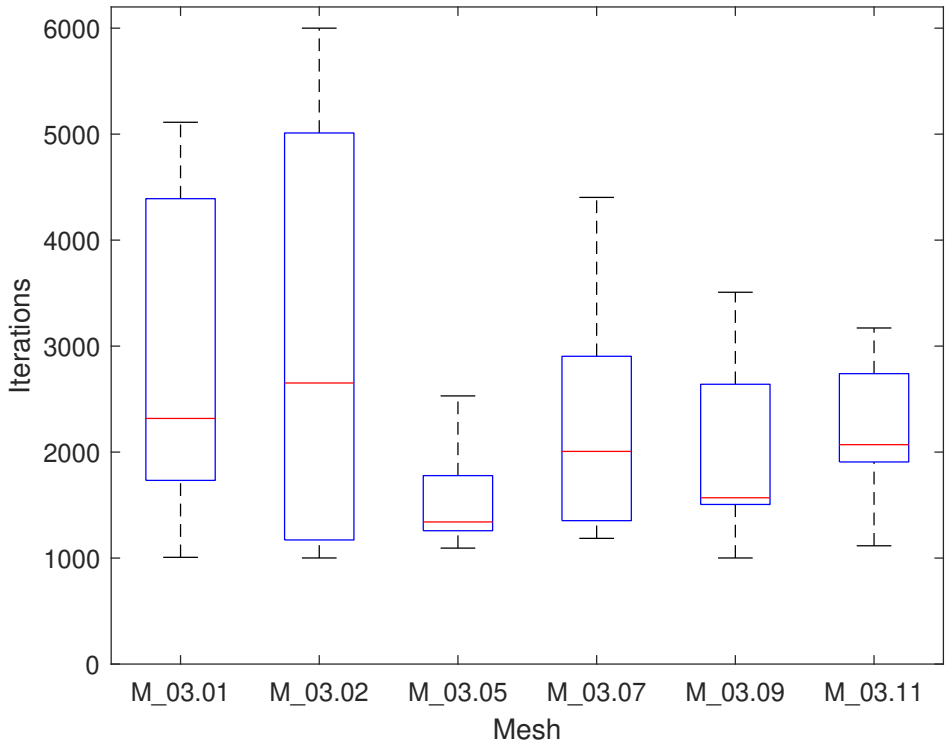

(A) Convergence scores.

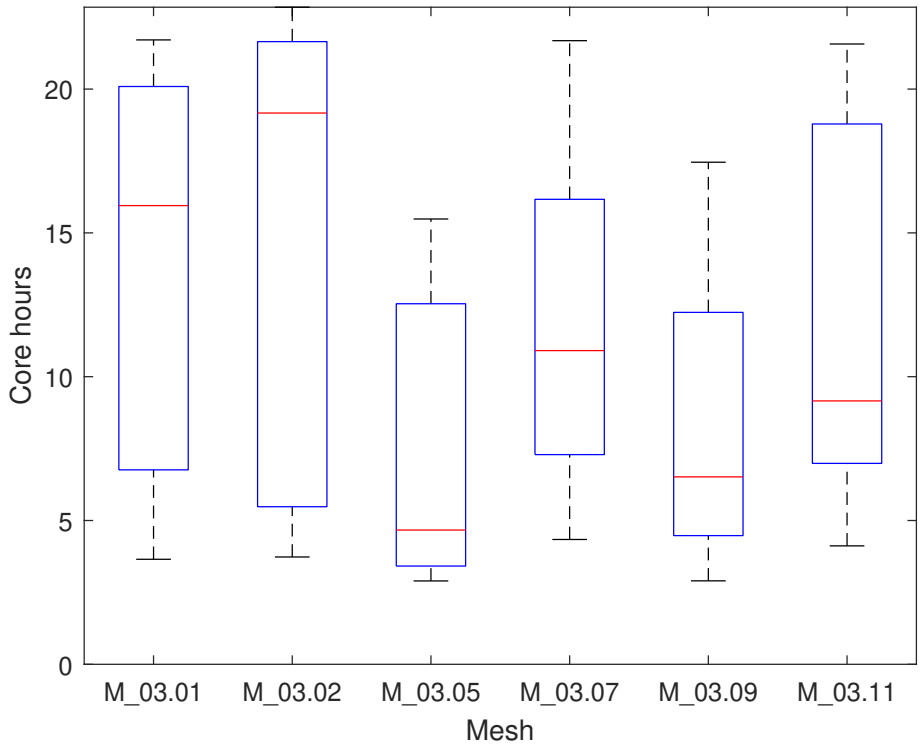

(B) Computational performance.

FIGURE 4.19: Comparison of convergence score and computational cost for the M_03 mesh family.

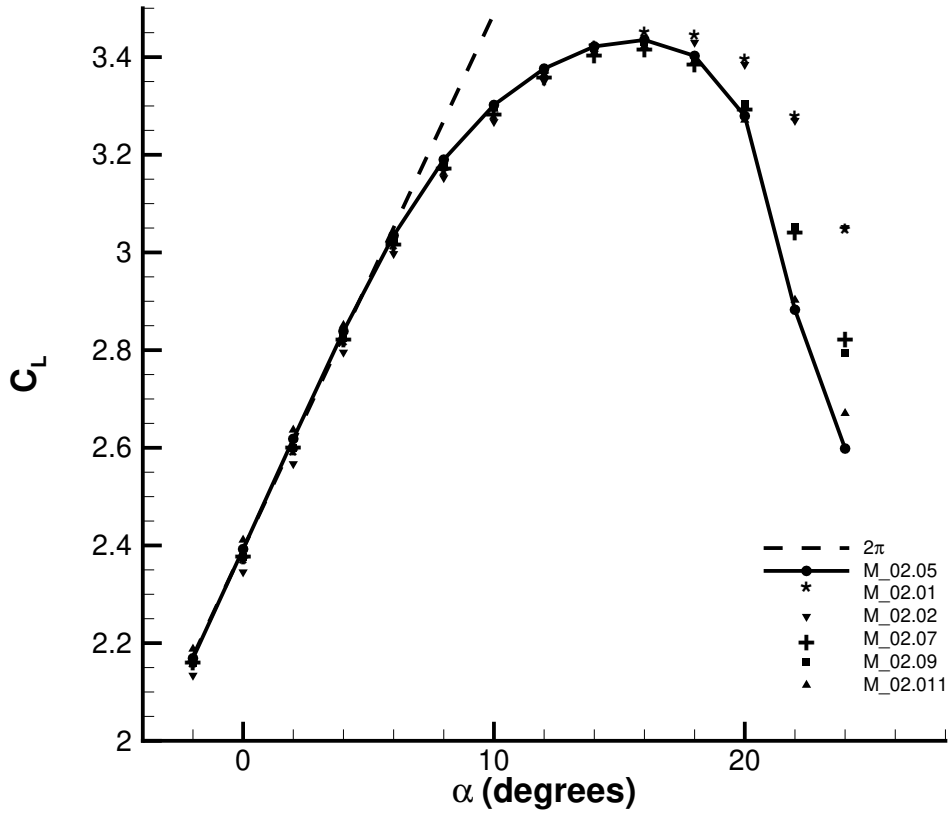

FIGURE 4.20: C_L polars for the M_03 mesh family. The solid line forms the polar of the superior mesh.

4.4.5 Generation 4: Effect of farfield distance

Figure 4.10b shows that the computational performance of M_03.05 was not as good as that of M_02.09. M_02.09 was therefore used to generate the M_04 mesh family. The 11 meshes of the M_04 family all converged adequately to produce 11 Green convergence–standard meshes. The convergence box–and–whisker plot is shown in Figure 4.21a. The computational cost comparison is shown in Figure 4.21b. Almost all of the M_04 meshes took approximately 1200 iterations to reach the convergence criterion. M_04.07 performed the best computationally, with the lowest median core hours to reach convergence criterion or iteration limit. M_04.07 had a fairly large leading and trailing edge spacing on the slat and flap, but a small spacing for the main element. This is summarised in Table 4.11, from the M_04 reference in Table 4.6.

Table 4.11: Parameter variations for generation M_04.

Mesh ID	**Farfield distance**	**Total cell count**
M_04.07	60c	75,299

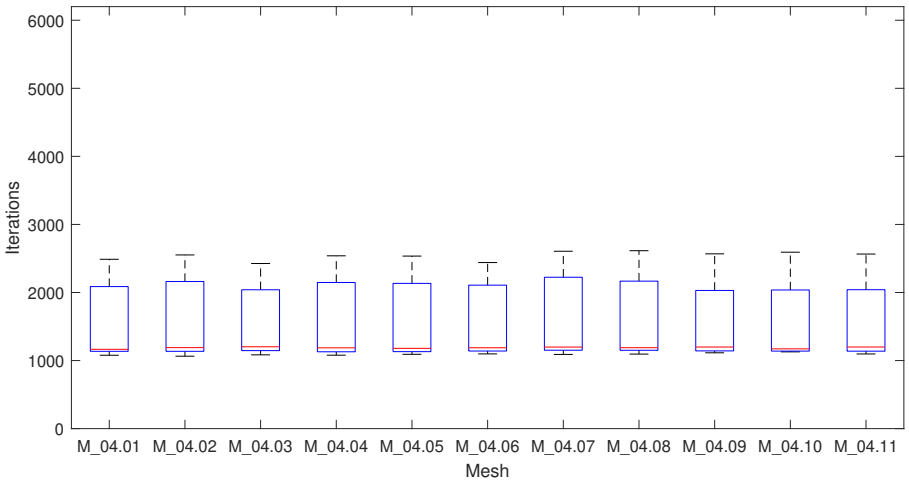

(A) Convergence scores.

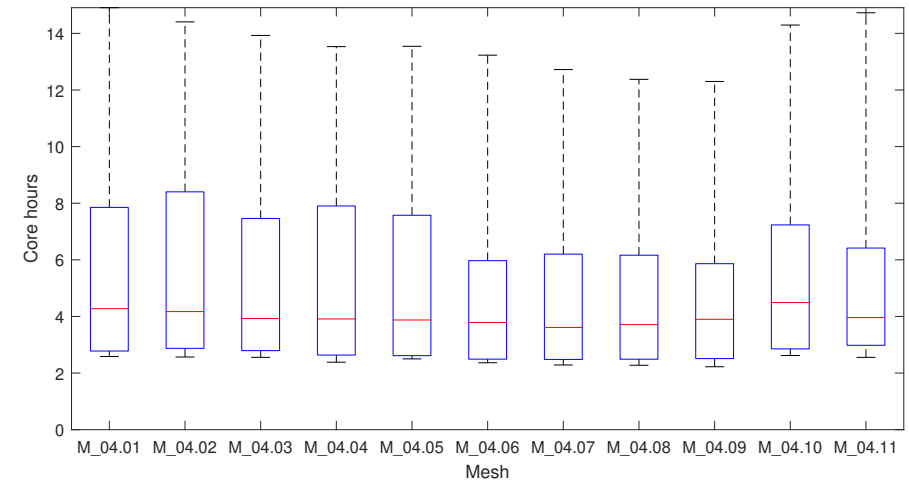

(B) Computational performance.

FIGURE 4.21: Comparison of convergence score and computational cost for the M_04 mesh family.

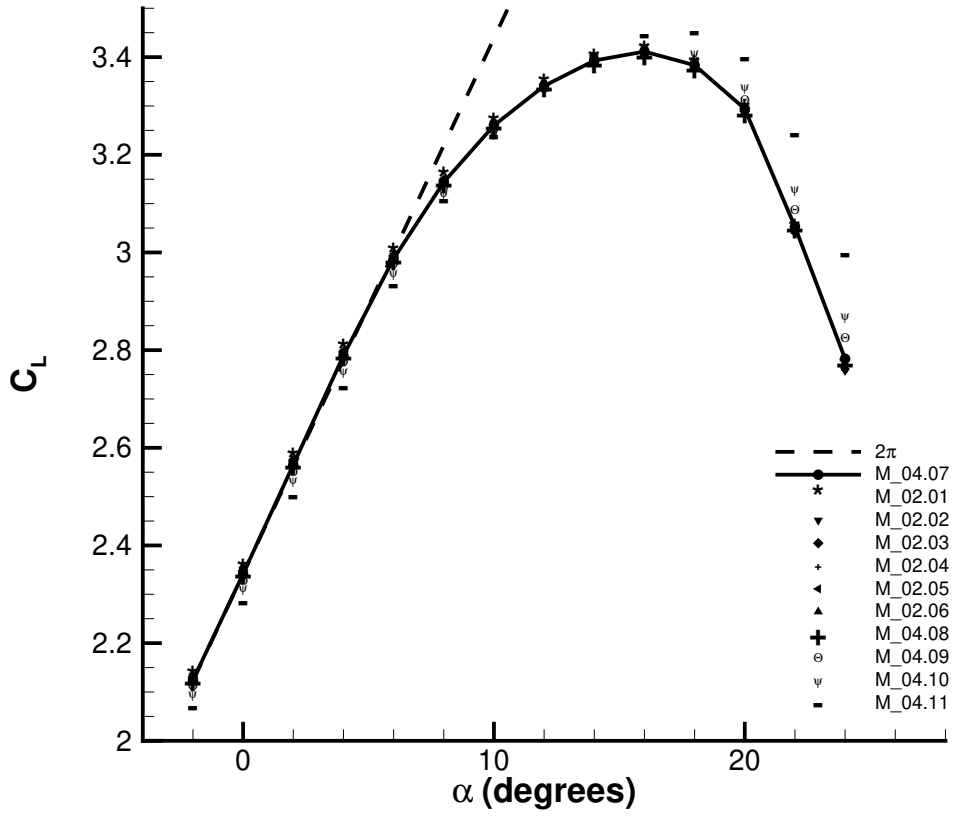

FIGURE 4.22: C_L polars for the M_04 mesh family. The solid line forms the polar of the superior mesh.

4.4.6 Mesh independence verification

A mesh independence study was run on the M_04.07 mesh, the results of which are shown in Figure 4.23. Mesh independence was achieved with a refinement factor of 2. Further refinement had no impact on the integrated coefficients.

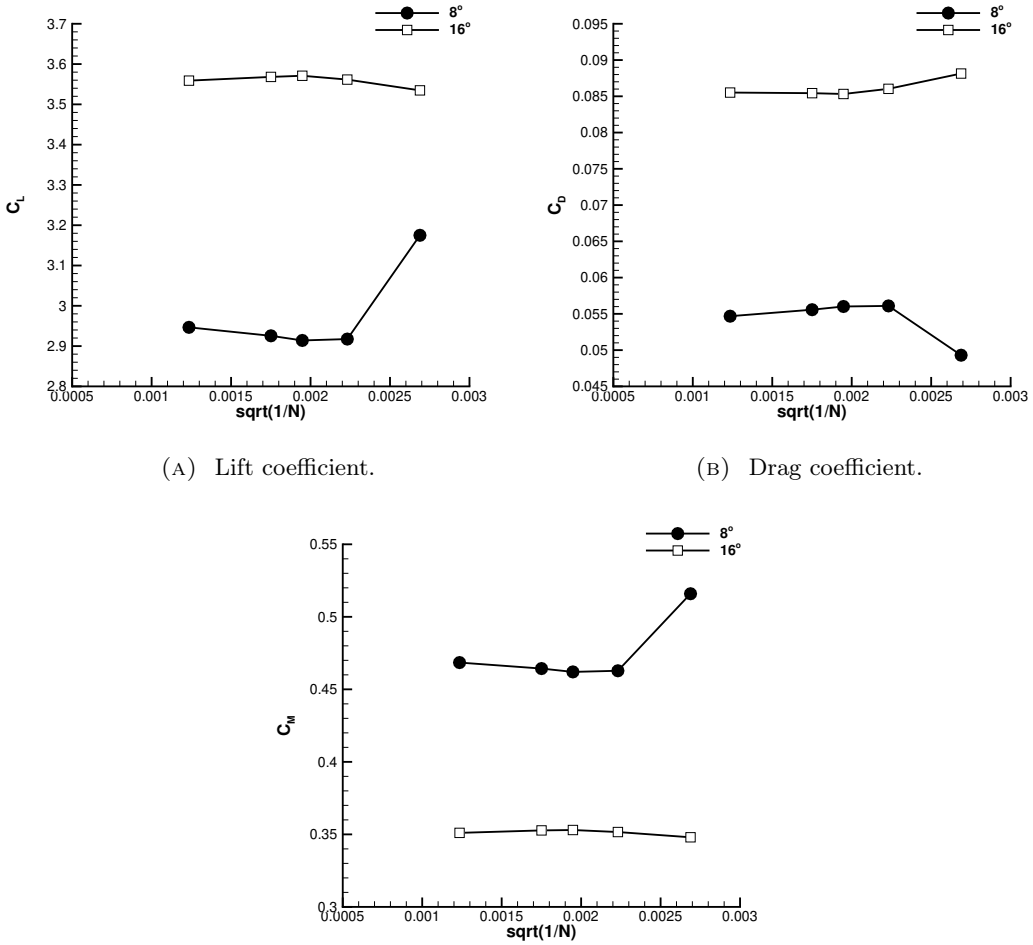

(A) Lift coefficient.

(B) Drag coefficient.

(C) Moment coefficient.

FIGURE 4.23: Mesh independence verification for M_04.07.

4.5 Best practice mesh

The reliability of CFD calculations have a strong dependence on grid topology. Four different families of meshes were produced to simulate the flow around a multi–element aerfoil at subsonic conditions over a range of angles–of–attack. In this study, 793 separate flow analyses were performed, using over one year of CPU time. Mesh topology parameters studied were cell type, aerofoil surface spacing, leading and trailing edge spacing, number of constant surface cell height layers, growth rate normal to the wall and farfield distance. Angles–of–attack in the range $-2°$ to $26°$ were used to compare the convergence rate and computation performance of each mesh. Superior meshes from each mesh family were used to generate the next family of meshes for a parametric study.

Our study has indicated that leading and trailing edges lengths are the most important single parameter for a multi-element aerofoil simulation, in particular leading edge/trailing edge length on the main element. It was in this mesh family that the biggest improvements on simulation time and convergence rate were made.

Recommendations:

1. Trianglular mesh topology produces better convergence across a wider range of angles–of–attack than quadrilateral cells.

2. The leading and trailing edge spacing of the main element should be no less than 7.00×10^{-4}c. Leading and trailing edge lengths on the slat and the flap should not be more than 1×10^{-3}c

3. Growth rate normal to the wall was found to be reliable at 1.2 but not beyond this value.

4. Number of constant cell height layers on the aerofoil wall has a limited positive or detrimental effect on the convergence rate and so is not advised being more than one.

5. Farfield distance was not found to affect the integrated flow coefficients for when farfield distance was greater than $\approx$ 40c. Choosing a farfield distance of 100c reduces the computational cost by a small degree compared to a small distance with no effect on the flow field and a farfield distance between 40c and 80c is reccommended.

6. The slat and the main element should have approximately the same number of surface points, while the flap should have at least 50% more.

Chapter 5

High-lift panel loads estimation using low-cost methods

A novel approach to sizing the high–lift actuation system was outlined in Chapter 3. This used results from 3D CFD to estimate the loads and stall conditions of the NASA CRM. A true multi-fidelity approach requires a fast method for high–lift panel loads estimation, and this chapter outlines the tool that is going to be used to do this: the Southampton multi–fidelity solver. The Southampton multi–fidelity solver was developed by Khalamov, et. al. and presented in [69]. This chapter details its application to loads estimation and to multi-element wings.

5.1 Southampton multi–fidelity solver

5.1.1 Background

Key to any aircraft design is the ability to assess the aerodynamic performance of a given aircraft configuration. The solution of the Navier–Stokes equations is recognised as a prerequisite for realistic flow applications, but the associated computational costs of the 3D problem can become prohibitive when confronted with the number of cases involved in some optimisation problems. Rapid CFD methods currently employed by academia and industry combine Prandtl's lifting line theory or the vortex lattice method (VLM) – linear 3D aerodynamic methods – with a 2D solution of the Navier–Stokes equations. The resulting aerodynamic predictive tool, often referred to as the quasi–3D method, is nonlinear because sectional flow nonlinearities are obtained from a 2D CFD analysis but inexpensive, as the overall cost of a quasi–3D analysis is comparable to that of a 2D CFD analysis.

The three main advantages of the quasi–3D method compared to full 3D RANS are:

1. No detailed 3D geometry information is needed; only planform and known aerofoil sections are required.

2. Computational requirements are reduced by one or two orders of magnitude.

3. Ease of multi–physics considerations such as icing or control sizing.

The Southampton multi–fidelity solver makes use of the α–based correction method, first proposed by Tseng and Lan [76] in 1988. In the Southampton multi–fidelity solver, two fidelity levels of aerodynamic flow prediction are used to obtain rapid estimations of aerodynamic loads in subsonic and transonic flight regimes: low–fidelity three–dimensional effects are modelled via a 3D linear steady and unsteady vortex lattice method solver, while a high–fidelity infinite swept wing RANS/URANS solver (DLR-Tau) is used to capture sectional viscous flow effects [69]. The background to

these two solvers is outlined in the next two subsections, and their interaction with each other is via a coupling algorithm, discussed further in Section 5.1.4.

5.1.2 Vortex Lattice Method

The steady and unsteady vortex lattice method solver implementation follows the description given by Katz and Plotkin [21]. At the end of each time step, a new row of wake panels is shed with a vortex strength equal to its circulation of the trailing edge panel (Figure 5.1). The induced velocities are calculated with the Bio–Savart law and incorporated in the aerodynamic influence matrix. The influence of the wake is added to the right–hand side vector, $\mathbf{R}$, which represents the non–circulatory velocity vector at each wing–bound collation point. The linear system of equations solved for each collocation point at every time step is given by:

$$\mathbf{A} \cdot \mathbf{\Gamma} = \mathbf{R}\,(\alpha) \tag{5.1}$$

Where $\mathbf{A}$ is the aerodynamic influence matrix and $\mathbf{\Gamma}$ is the global vector of circulation intensities of wing bounded VLM panels which has to be solved. The α–based coupling algorithm corrects the freestream angle of attack, α_∞, acting on the collocation point of the k-th wing–bounded VLM panel,α_n. This enables the local inviscid lift force coefficient, $C_{L,inv}$, to be manipulated using an angle of attack correction for each panel, $\Delta\alpha_n$, as described in Equation 5.2.

$$\alpha_n = \alpha_\infty + \Delta\alpha_n \qquad n = 0, 1, 2, ..., N-1 \tag{5.2}$$

Where N is the total amount of wing–bounded VLM panels ($N = N_x \times N_y$), and α_n is the total freestream angle of attack at the collocation point of the n-th wing–bounded vortex ring. The freestream angle of attack at the particular collocation point of a n-th wing bounded VLM panel, α_n, the freestream velocity vector is rotated in the form:

$$\mathbf{V}_{\infty,n} = |V_\infty| \cdot \mathbf{Rot}_y\,(\Delta\alpha_n) \tag{5.3}$$

Where $|V_\infty|$ is the freestream velocity magnitude and $\mathbf{Rot}_y\,(\Delta\alpha_n)$ is a (3×3) rotation matrix around the y-axis. This is represented diagramatically in Figure 5.1.

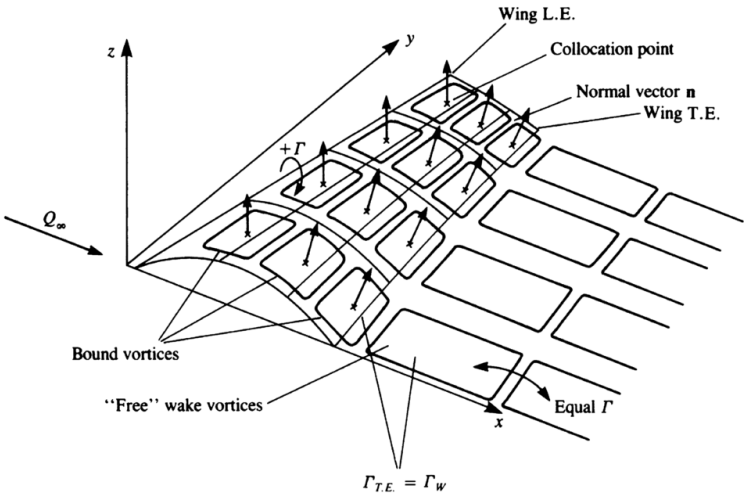

FIGURE 5.1: Vortex representation of thin lifting surfaces [21].

A single element of $\mathbf{R}$, R_n, can be given by Equation 5.4.

$$R_n = -\mathbf{n}_n \cdot (\mathbf{V}_{\infty,n} + \mathbf{\Delta V}_{w,n}) \tag{5.4}$$

Where $\mathbf{n}_n$ is the normal vector of the n-th vortex–ring element and $\mathbf{V}_{\infty,n}$ is the freestream velocity vector corrected by the current angle of attack correction, $\Delta\alpha_n$. The aerodynamic forces on the lattice can the be computed by applying the Kutta–Joukowski theorum [77]:

$$\mathbf{F}_n = \rho \mathbf{V}_n \times \mathbf{\Gamma}_n \tag{5.5}$$

5.1.3 Infinite swept wing solver

DLR–Tau [78] is a finite volume–based CFD flow solver used by a number of aerospace industries across Europe, including Airbus. The flow solver contains an efficient algorithm known as the 2.5D+ method, that can solve flows around an infinite swept wing at the computational cost of a 2D RANS simulation [70].

The influence of the wing sweep angle within the context of a purely 2D grid stencil is dealt with by imposing appropriate boundary conditions at the far–field, namely that the derivatives of the wing cross–flow properties, $\partial(\cdot)/\partial y'$, are set to zero. The $'$ indicates that coordinates have undergone a transformation as shown in Figure 5.2.

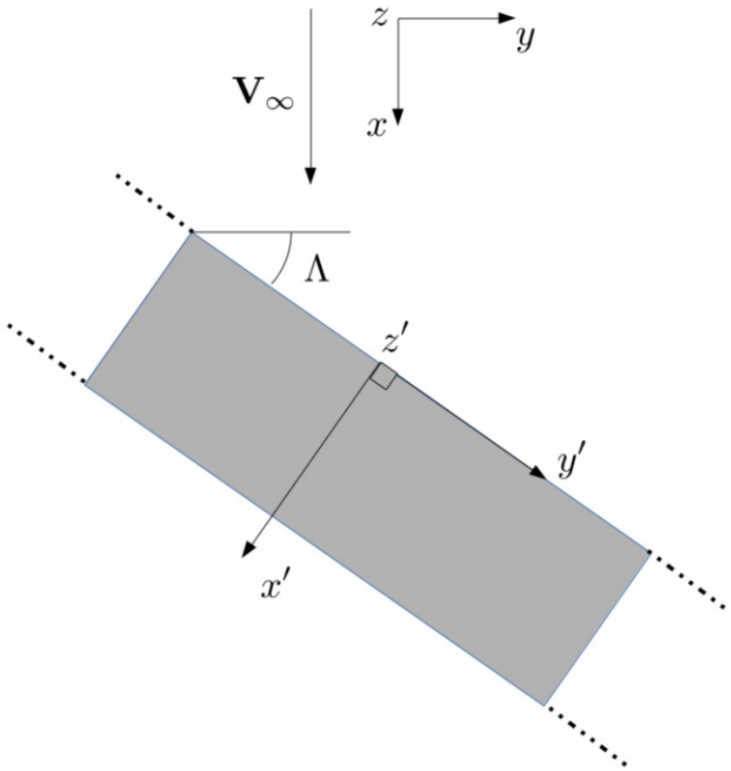

Figure 5.2: Schematic of a infinite swept wing; flow from top to bottom.

The 2.5D+ solver is a key capability as it can account for the cross–flow effects required by the multi–fidelity solver without requiring an expensive 3D grid stencil.

5.1.4 The alpha–coupling loop

Both the VLM and the 2.5D+ method are coupled together in the multi–fidelity solver using an α–coupling loop. The span–wise position and number of RANS sections is at the discretion of the user. Figure 5.3 contains two such sections and demonstrates graphically how the two solvers are coupled together in the computational domain to produce the 3D wing represented in the physical domain.

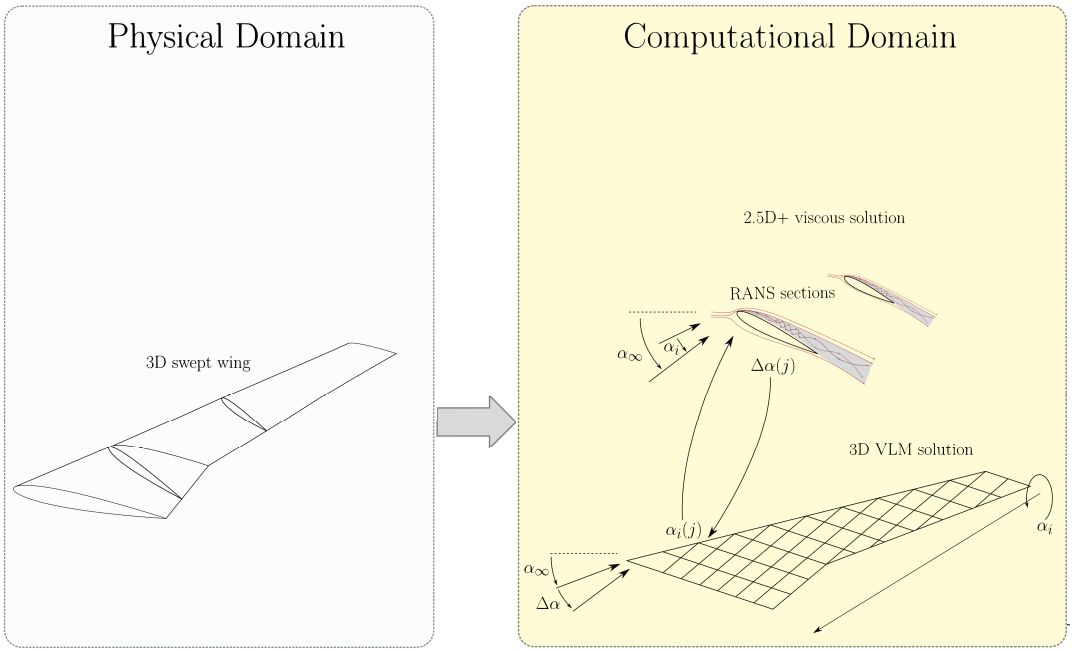

FIGURE 5.3: Diagram showing the multi–fidelity solver.

The following describes how the multi–fidelity solver converges on a solution at one particular span–wise location.

Computation of lift–polar

The first step that has to take place before the alpha–coupling loop can be set to run is the computation of the viscous lift polar for each 2D section. This involves computing the lift at the desired flow conditions at a range of angle–of–attacks, usually in $\sim 1^\circ$ intervals. The

Coupling algorithm

The free steam has angle–of–attack α_∞. The inviscid lift distribution, $C_{L,inv}$, along the entire wing for this farfield angles–of–attackis initially found by solving Eqn. 5.1 for $\alpha(j) = \alpha_\infty$. The angle–of–attack at the j-th span–wise panel, $\alpha(j)$, is equal to the farfield value for the first iteration only. The inviscid solution includes an estimate of the lift distribution along the wing (and therefore the lift coefficient, $C_{L,inv}$) and the induced angle–of–attack, $\alpha_i(j)$, at each span–wise location. The induced angle–of–attack is caused by the wing-tip vortices and is a 3D effect that is passed to the 2D viscous solver via an 'effective' angles–of–attackvalue, α_e.

$$\alpha_e(j) = \alpha_\infty - \alpha_i(j) \tag{5.6}$$

The effective angle–of–attack at the RANS section is passed to the viscous solver to compute the viscous lift coefficient, $C_{L,vis}(j)$ at that span–wise position. $C_{L,vis}(j)$ and $C_{L,inv}(j)$ will differ in the first few iterations of the loop. This ΔC_L is turned into $\Delta\alpha$ using the following equation:

$$\begin{aligned} \Delta C_L =& C_{L,vis}(j) - C_{L,inv} \\ \Delta\alpha_n =& \nu \frac{\Delta C_L}{2\pi} + \Delta\alpha_{n-1} \end{aligned} \tag{5.7}$$

where ν is a relaxation factor to stabilise the convergence. For the second loop:

$$\Delta\alpha_2(j) = \nu \frac{C_{L,vis}(j) - C_{L,inv}}{2\pi} + \cancelto{0}{\Delta\alpha_1(j)} \tag{5.8}$$

This $\Delta\alpha$ term forms an angle–of–attack correction distribution along the wing. The inviscid equations are solved again, including these corrections, and a new local lift coefficient $\Delta C_{L,vis}(j)$ is computed for each span–wise position. The process is then repeated, but this time $\alpha \neq \alpha_\infty$. The algorithm continues until the largest ΔC_L is less than a user-specified value:

$$\Delta C_L = C_{L,vis} - C_{L,inv} < \epsilon \tag{5.9}$$

If the user selects more than one URANS section, linear interpolations of $\Delta\alpha$ are performed across the span. The iterative loop continues until convergence of the lift coefficient is achieved. Advancing of the solution includes shedding of the wake carpet behind the wing and incrementing the physical time of both the UVLM and URANS solvers. Lastly, the computation is finalized, and memory is deallocated. The full process is shown in Figure 5.5.

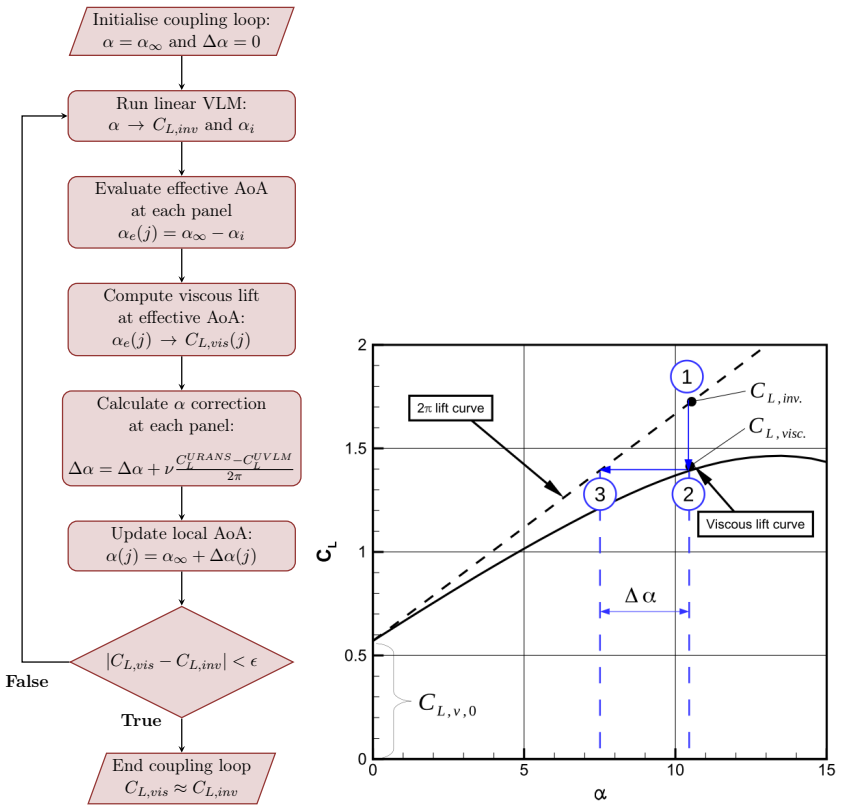

FIGURE 5.4: Alpha–coupling algorithm. [71]

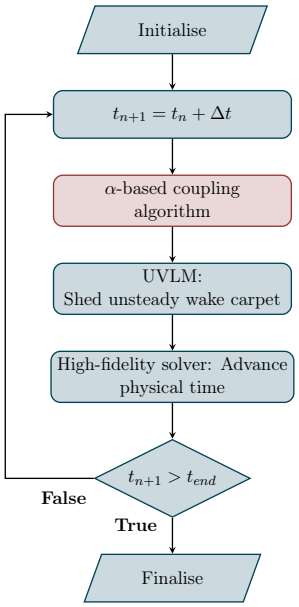

FIGURE 5.5: Unsteady multi–fidelity solver algorithm. [79]

The coupling algorithm, which synchronizes the execution of the VLM and RANS solvers, is written in Python. By using the Python C–API, data is continuously exchanged between Python and C subroutines of the VLM code. A Python wrapper of the DLR-TAU code is also employed, which allows subroutines calls of the RANS solver directly from the main framework and exchange data over shared memory.

5.2 High–lift panel loads estimation proceedure

The speed and accuracy of the Southampton multi–fidelity solver outlined in Section 5.1 was combined with the meshing procedure developed in Chapter 4 for producing high-quality meshes with good convergence performance across a wide range of angles–of–attack. This provides the potential for a rapid high-lift panel loads estimation tool. A demonstration of this novel approach is described in this section, and what follows is a preliminary proof–of–concept. The process has a significant number of descrete steps (as illustrated in Figure 5.6) but none are computationally expensive, unlike the process used to estimate the loads in Chapter 3.

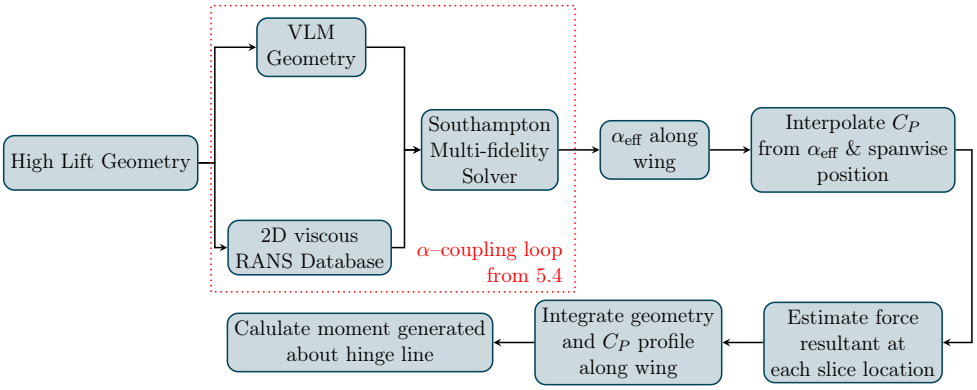

FIGURE 5.6: Steps required to produce a low computational cost estimate of high-lift surface hinge moment using the Southampton multi–fidelity solver.

5.2.1 Viscous lift sections

As discussed in Section 5.1, the Southampton multi–fidelity solver requires 2D viscous lift polars to provide estimates of C_L using the local angle of attack calculated from the combination of the freestream and induced angle–of–attack. For a wing such as the HL-CRM with complex geometry, the location of the sections used to generate the viscous polars needs to be considered carefully. Each section is computed as an infinite swept wing, as described in Section 5.1.3. To faithfully represent the wing with as few viscous sections as possible, the aerofoil section needs to vary as little as possible in shape in the spanwise direction between sections. The chord length reduction that takes place with the tapering of the wing can be accounted for and is decribed later. To assist with the choice of placement of these viscous sections, the wing planform has been divided into three zones which have similar chordwise shapes across their span. These are illustrated in Figure 5.7 and summarised below:

- Zone 1 - The region immediately outboard of the fuselage body including starting at the inboard portion of the slat and including the entire of Flap 1.
- Zone 2 - The portion of wing from the kink at the start of Flap 2 to the end of Flap 2.
- Zone 3 - The outboard portion of the wing starting just outboard of Flap 2 and enclosing the outboard portion of the slat panel. This zone does not enclose any part of the flap panel.

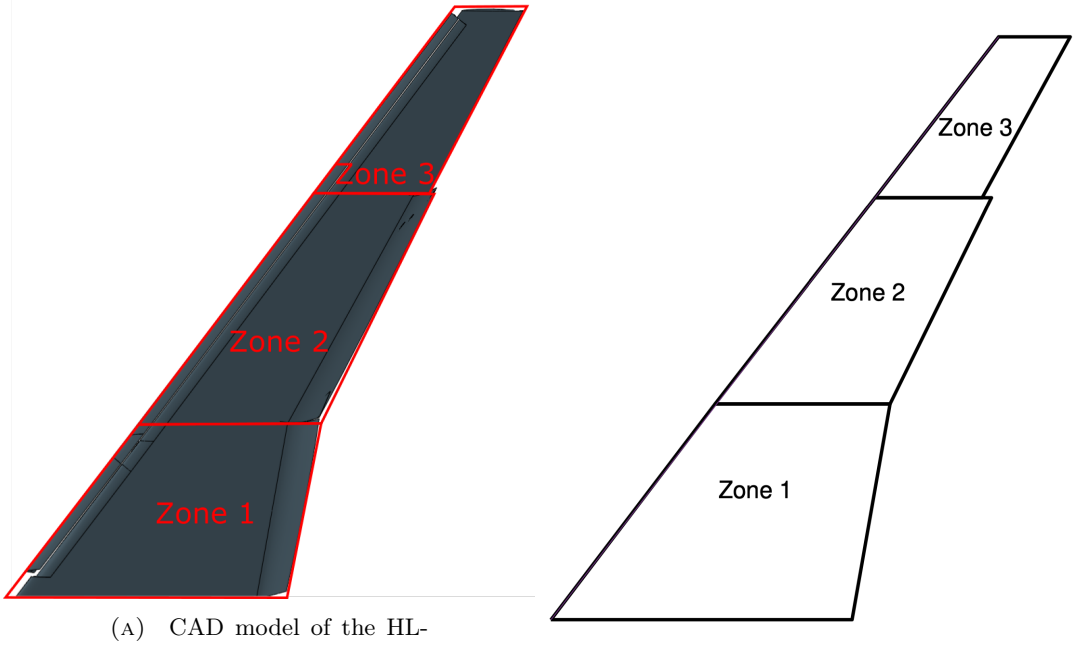

(A) CAD model of the HL-CRM wing showing the three zones.

(B) Diagrammatic representation of HL-CRM planform.

FIGURE 5.7: HL-CRM zones.

2D streawise intersection curves were taken at the start and end of each zone to generate the aerofoil geometries. The non-dimensional spanwise positions of these sections is given in Table 5.2. The precise relative positions on the wing are indicated in Figure 5.8. This placement of viscous sections was made for two main reasons:

1. The distance between sections containing a discontinuity (ie. zone boundaries) was kept to a minimum, meaning interpolation of forces is valid for the majority of the wing area.

2. Viscous lift data is approximately uniformally distributed along the wing, occurring at four key positions on the wing: inboard, outboard, and at each zone boundary.

Adding further sections increases the computational cost with little benefit to accuracy. Intermediate positions in the middle of the zones, where additional sections would be placed, do not have vastly different geometries to those at the start and the end of the zone. They therefore do not produce sufficiently different lift polars to affect the calculation.

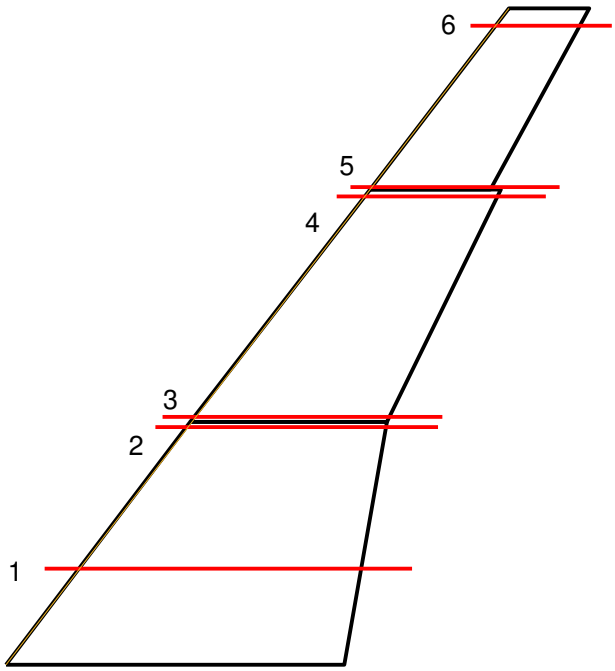

FIGURE 5.8: Diagrammatic representation of the HL-CRM wing showing the locations of each 2D section used to generate the viscous data.

The meshing best practice outlined in Chapter 4 was then used to create six corresponding grids as shown in Figure 5.9. Though appearing identical, Sections 2 and 3 are not the same and differ slightly in twist. This accounts for the small difference seen in the lift polar of the two sections in Figure 5.10. DLR-TAU calculates chord length automatically, and the method used causes an overestimate in chord length when multi-element sections have overlapping surfaces [20], causing a corresponding underestimate in C_L. Each 2D streamwise wing section was therefore scaled in size manually to unity, and the reference area set explicitly to 1m^2.

The 2D CFD computation was performed with DLR-TAU at the same flow conditions described in Figure 3.8. Alpha-sweeps for each section were performed with increments of $1°$. The lift coefficients for the angles–of–attack which converged fully were plotted. The polars for each of the six sections shown in Figure 5.10, and to the

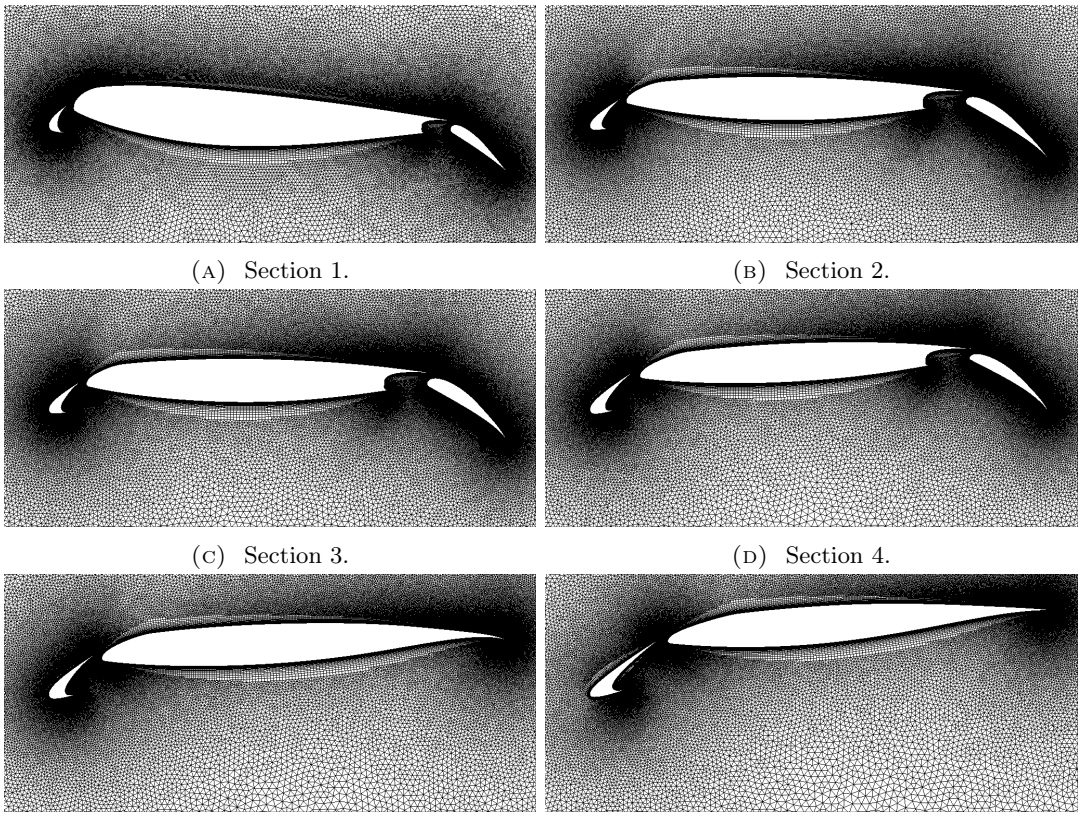

(A) Section 1. (B) Section 2.

(C) Section 3. (D) Section 4.

(E) Section 5. (F) Section 6.

FIGURE 5.9: Sections 1-6 grids. Geometric twist becomes increasingly negative with distance from the wing root, information which is preserved in the grid.

full 3D lift polar (originally shown in Figure 3.11a) is included for comparison. As expected, the inboard four sections with positive twist and large camber (due to the presence of a trailing edge flap), have a larger C_L at every value of α_∞than the overall wing. The outboard two sections have lower C_L values.

Vortex lattice

The 3D effects on the viscous sections are computed using the vortex lattice method on a grid shaped like the silhouette of the wing planform with the high-lift surfaces deployed as shown in Figure 5.11.

Comparison of results for the Southampton Multi–fidelity solver

The viscous lift data from the six sectional positions and the vortex lattice grid were then used as inputs for the hybrid Southampton multi–fidelity solver. A lift polar was produced and compared to the 3D polar from Figure 3.11a. This comparison is shown in Figure 5.12 and good agreement is seen between the 3D CFD and the Southampton multi–fidelity solver up until stall. Converged results for the hybrid method were not possible in this non-linear region because the angles–of–attack measured were.

As discussed in Section 3.2.2 in further detail, one of the first steps in estimating the high-lift surface hinge loads is to compute the sizing flow conditions relevant to actuation sizing. This is done from from the peak value of α, $\alpha_{\max}$, the maximum landing weight and certification requirements. An estimate of the $\alpha_{\max}$ was made

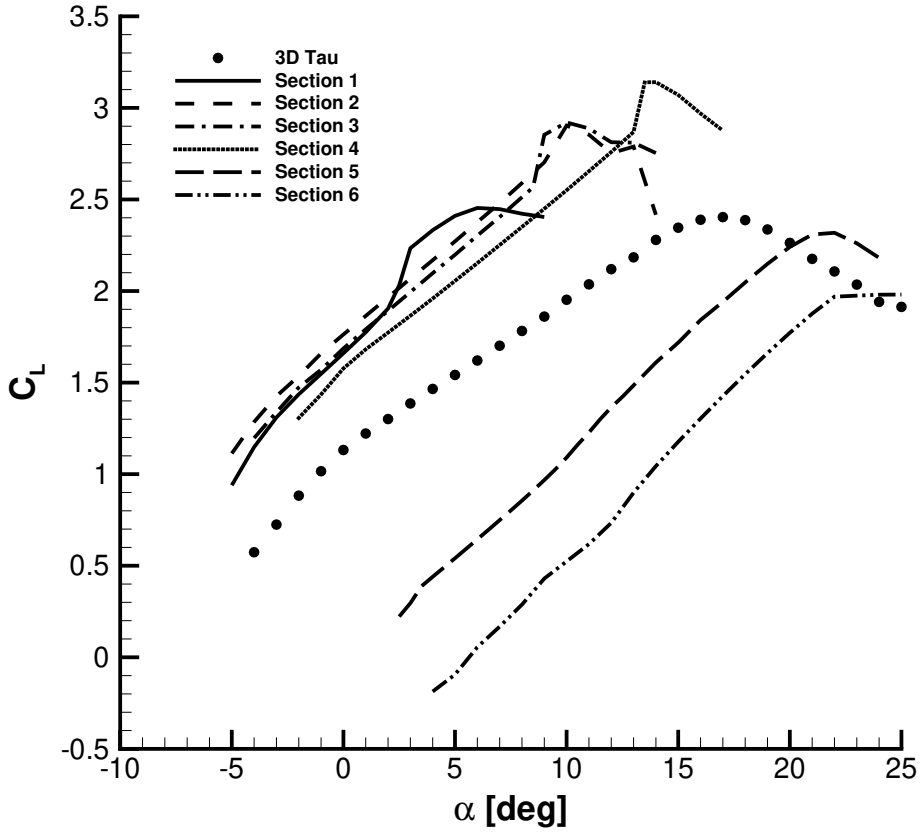

FIGURE 5.10: Viscous lift coefficients for each 2D section as compared to the 3D lift polar for the HL-CRM. These lift polars form the viscous database that is coupled to the VLM grid. The increasingly negative geometric twist accounts for the rightwards displacement of the outboard sections.

using the Southampton multi–fidelity solver by making the assumption that the highest converged value was equal to $\alpha_{\max}$. This assumption is based on the fact that the flow becomes highly non-linear and poorly converged beyond stall, and that the Southampton multi–fidelity solver is therefore sensitive to this flight regime. The parameter estimates for the sizing flow condition in Table 5.1 were computed in this way, and are extremely close to the values estimated using computationally expensive 3D CFD.

TABLE 5.1: Estimates for the sizing flow condition made using full 3D CFD simulations with DLR-TAU, and with the computationally inexpensive Southampton Multifidelity Solver.

Parameter Estimate	**3D Tau**	**Southampton Multi-fidelity Solver**
$C_{L,\max}$	2.40	2.47
V_{S0} [m/s]	59.0	58.4
$C_{L,\text{sizing}}$	0.74	0.76
$\alpha_{\infty,\text{sizing}}$ [°]	-2.9	-2.5

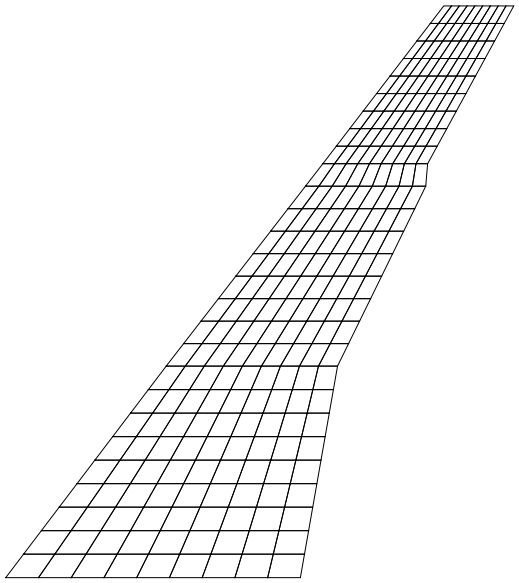

FIGURE 5.11: Vortex lattice grid of the HL-CRM planform used by the Southampton multi–fidelity solver for rapid loads estimation.

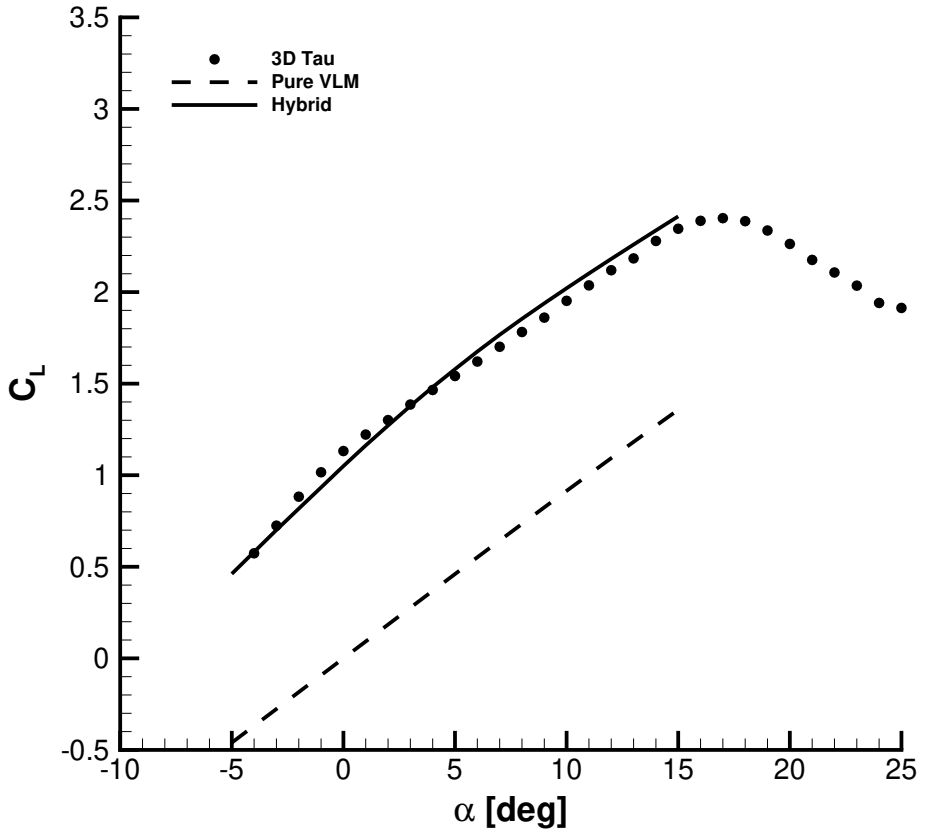

FIGURE 5.12: Comparison of lift polars for the Pure VLM, full-3D analysis, and the hybrid method. The inviscid VLM does not account for camber, hence the vertically displaced position relative to the methods which include viscosity.

Using the Southampton Multi–fidelity solver to estimate hinge moments

The challenge with using the Southampton multi–fidelity solver to compute high–lift surface hinge moments is that an estimate of the pressure forces along the full length of all three surfaces needs to be made using only pressure force data from the six sections shown in Figures 5.8 and 5.9. The surfaces vary in both size and shape along their length, and the location of the hinge line changes. Figure 5.13 shows the variation in effective angle–of–attack, α_{eff}, at all spanwise positions from the wing root to wing tip, calculated using the Southampton multi–fidelity solver. The large spanwise variation in α_{eff} seen here further complicates the situation, as local α needs to be accounted for alongside geometry, local chord, and hinge line placement when calculating the hinge moment.

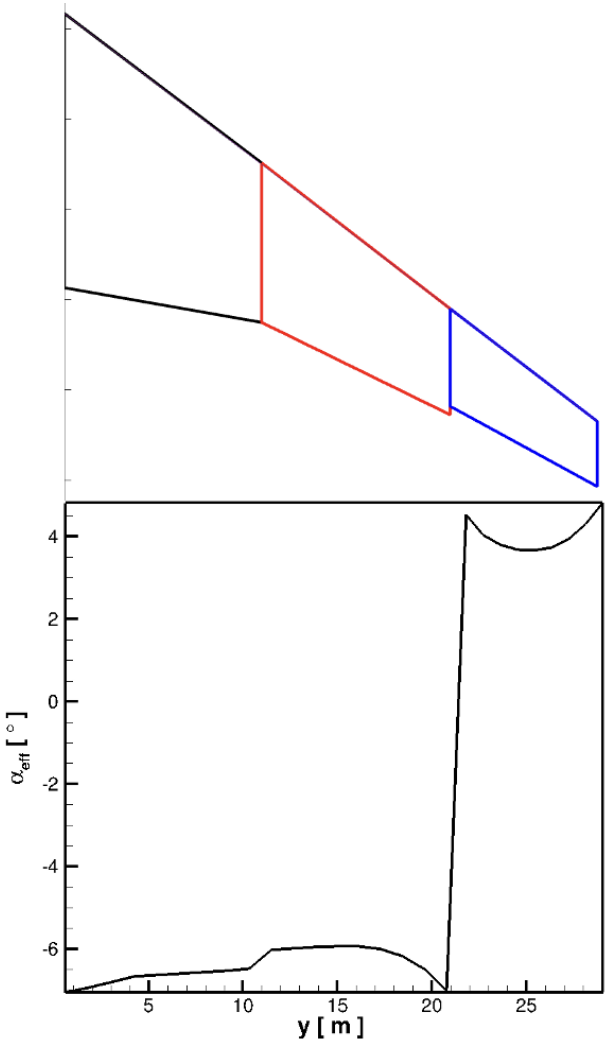

FIGURE 5.13: α_{eff} against spanwise position, y. The free-stream angle–of–attack used was $\alpha_{\infty,\text{sizing}} = -2.5°$.

The effective angle–of–attack at each of the six sections is recorded in Table 5.2. These values were interpolated from Figure 5.13. Hinge moment calculation requires summation of all moment contributions by the small surface pressure forces on each panel. As the sectional lift data was only recorded for increments of 1 degree angle–of–attack, a MATLAB script was written to compute interpolated C_P values for any arbitrary angle–of–attack between the integer alphas calculated for each section using

DLR-Tau. Shown in Figure 5.14 is the geometry for the slat panel at Section 1 – the most inboard section. As recorded in Table 5.2, α_{eff} at this location is $-6.7°$. This value lies between the computed values of $\alpha = -7°$ and $-6°$. The pressure forces are visualised for these α's in Figures 5.14a and 5.14c respectively. Figure 5.14b shows the pressure coefficients interpolated from these two angles–of–attack.

Table 5.2: Effective angle–of–attack at each of the 6 viscous sections along with their non-dimensional spanwise location and local chord length.

Section	**Non-dimensional Spanwise Position [y/b]**	**Local Chord Length, c_i [m]**	α_{eff}
Section 1	0.147	11.83	−6.7
Section 2	0.364	8.19	−6.3
Section 3	0.379	7.90	−6.2
Section 4	0.716	5.40	−4.0
Section 5	0.731	5.06	0.7
Section 6	0.977	3.27	4.6

Figure 5.14 demonstrates interpolation of C_P's at a single spanwise location. To compute this C_P profile's contribution to it's panel's hinge moment, the total size of each surface pressure force needs to be known. Data exported by DLR-Tau for each angle–of–attack include the surface pressure forces, so the exact size of each surface element does not need to be known directly, as it would if only C_P was exported. However, as each chord section used by DLR-Tau was scaled to 1m in length, the force values must be scaled by a factor equal to the local chord. Scaling by the local chord, c_i, allows the elemental force vectors on the panel surface to be a true estimate of their full-sized values, per unit span. Table 5.2 also includes the local chord lengths for each of the viscous sections. These chord lengths values can be interpolated to get good estimates of c_i's at intermediate spanwise positions. This facilitates the generation of 'quasi-sections' – chord sections based on geometry of Sections 1-6, but scaled to the estimated local chord size. Figure 5.15 shows the three panels of the HL-CRM generated using quasi-sections. Also shown are the hinge lines about which the moment contributions of each quasi-section are calculated. The vector defining the hinge line for each of the three high-lift surfaces (taken from the data assembled in Table 3.6) was used to produce these.

Once the quasi-sections can be generated, α_{eff} values interpolated for each quasi-section, and hinge lines placed appropriately, the summation of the forces along the span can take place. Each surface force vector was scaled by local chord, c_i, and by quasi-section width, δy. Eqn. 2.21 was used to compute the small moment contribution of each force element about that panel's respective hinge line. A value of $\delta y = 0.1m$ was used for the quasi-sectional lift. Table 5.3 shows the preliminary results from this proof-of-concept rapid method for estimating high-lift surface loads. There is a considerable degree of discrepancy, particularly in the hinge moment for Flap 2. Sources of possible error are plentiful and include:

- Incorrect α_{eff} due to VLM setup used in Southampton multi–fidelity solver. There are a number of different possible VLM configurations, including those with twist, without twist, with multiple surfaces representing the leading and trailing edge panels. Further investigation is required to understand what, if any, impact these different VLM geometries make on the problem.

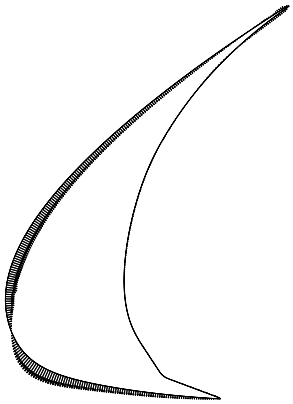

(A) $\alpha_{\text{eff}} = -7^\circ$

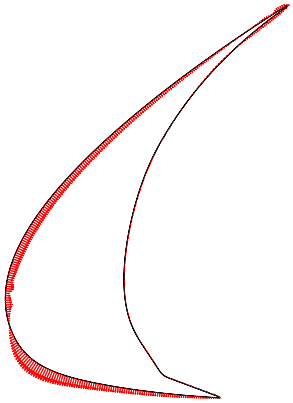

(B) $\alpha_{\text{eff}} = -6.7^\circ$ (interpolated)

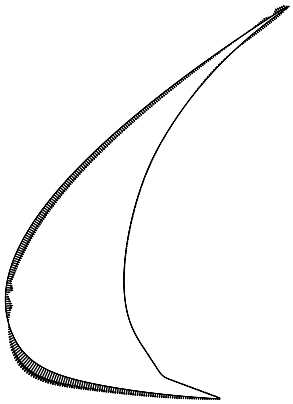

(C) $\alpha_{\text{eff}} = -6^\circ$.

FIGURE 5.14: Graphical illustration of the C_P interpolation. 5.14a and 5.14c are show the 'true' surface pressure forces as calculated by DLR-TAU at $\alpha = -7^\circ$ and -6° respectively. 5.14b shows the surface C_P estimates at $\alpha_{\text{eff}} = -6.7^\circ$ interpolated from these computed C_P values.

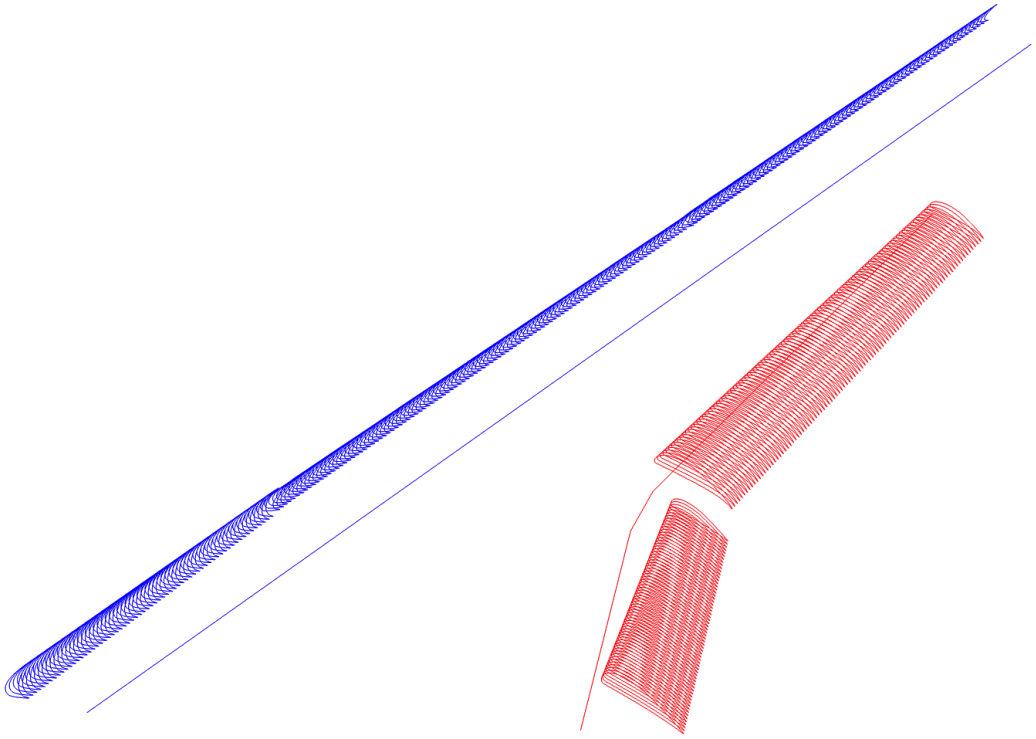

FIGURE 5.15: Plot of interpolated surfaces constructed using only the six sectional geometries and corresponding hinge lines.

- Poor surface force data at more extreme values of α_{eff}.
- Relevant 3D effects not captured using the rapid CFD that had an impact on hinge moment when using full 3D. For example, the 3D flow features seen causing the complex skin friction plot in Figures 3.11b and 3.11c will not be captured by this quasi-3D method and this may have an impact on the estimated moments generated
- Geometry approximation made using 'quasi-sections' did not represent the true wing geometry accurately enough. Adding more sections will increase the computational cost and complexity of the problem, but will make the geometry interpolation more faithful to the true wing sections.

Further work is required to understand which of these, if any are the cause of the discrepancy. Though the results were not as close as was hoped, the results were within the correct order of magnitude, including (in the case of Flap 1) within the 35% of the 3D value. The 100× computational cost improvement over the 3D method provides significant incentive to refine this process further.

To summarise, hinge moment estimates were made at a low computational cost compared to the approach which used 3D CFD in Section 3.2.2. Six 2D chordwise sections were taken at 6 different spanwise locations, and their geometries were meshed using the best practice methods outlined in Chapter 4. These grids were then used to compute a database of viscous lift polars. A Vortex Lattice grid was made from the planform shape of the wing, and the viscous database and the vortex lattice were used as inputs to the Southampton multi–fidelity solver. Lift polars computed using the Southampton multi–fidelity solver were compared to 3D values and showed good agreement. The convergence limit of the Southampton multi–fidelity solver was then

TABLE 5.3: Comparison of hinge moment calculated using 3D CFD and using the Southampton multi–fidelity solver.

	Hinge moment estimate [kNm]	
Surface	**3D Tau**	**Southampton Multi-fidelity Solver**
Flap 1	49	37
Flap 2	49	9
Slat	38	22

used to estimate the sizing flow condition of the CRM and this was compared to the sizing flow condition estimated using 3D CFD. They showed strong agreement. Finally, a technique to integrate the sectional force data along the wing, taking into account wing geometry and effective angle–of–attack, α_{eff}, was introduced. This produces estimates of the hinge moments at a small computational cost which were then compared to the corresponding values obtained with 3D CFD. However, for this novel method to be useful for aircraft conceptual design and high–lift actuation sizing, the discrepancies identified need to be better understood and eliminated.

Chapter 6

Impact of High-Lift Actuation on Dynamic Aeroelastic Response

The distribution of mass of the wing causes a significant effect on the dynamic properties of a structure. However, dynamic aeroelastic effects are typically considered less during initial design efforts. The potential concequence of this is that unforeseen dynamics are only discovered later in the design process, and if harmful, may have to be overcome through mass distribution alterations [35]. Knowledge of the high–lift actuation system mass and distribution could therefore allow for more precise aeroelastic tailoring in the early phases of design. Aeroelastic tailoring involves controlling the directional stiffness of an aircraft structural design to achieve light weight airframe designs [36], and is an example of passive aeroelastic control [37].

It was discussed in Section 2.1 that a significant contribution to the non–structural mass distribution within the wing is made by the high–lift geared rotary actuators (GRAs) [39], [40]. These reduction gearboxes turn high RPM rotation from hydraulic motors into high torque rotation that is used to deploy the flaps and the slats. These dense GRAs are small fractions of a metre in any dimension, and are therefore small enough to be considered lumped masses from an aeroelastic analysis perspective. Every slat and flap panel has two, with the largest and heaviest being in the the trailing edge (TE) of each wing, due to the torque demand of the large trailing edge flap panels. The sizes of these masses can be estimated from knowledge of the torque required of them and from industrial data which sizes the actuators.

It is the prospect of reducing the uncertainty in dynamic aeroelasticity and aircraft sizing that has motivated this chapter's study. In [1] and 3.1.4, a low–cost actuation mass estimation method was presented which used industrial data to correlate rated output torque with mass for high–lift GRAs. This method was used to estimate the mass of the high–lift actuation system including the GRAs in the high–lift configuration of the NASA Common Research Model (CRM), an open source model of a representative wide–bodied jet airliner. Herewith, we investigate the impact including precise mass values of high–lift actuators on wing design and sizing for the same test case. The work is unique in its attempt to unite low speed design decisions on the high speed aeroelastic analysis and has been achieved through three main steps:

1. Estimation of the actuator masses and locations by analysing the required performance of the high–lift actuation system at low flight speeds.

2. Formulation of various actuation mass cases which depend on design decisions motivated more by minimization of either cost or mass.

3. Quantification of the impact of these mass cases on flutter and gust loads analysis, compared to the baseline configuration.

6.1 Aeroelastic Analysis

As well as clean wing [80] and high–lift geometries [81], detailed wingbox structures based on the CRM outer mold line have been developed and made available [82], [83]. This allows for an investigation into the impact of high–lift actuation mass on flutter and gust loads. The wingbox model of the CRM was provided in Nastran BDF format and consists of a shell-based primary structure with implicit stiffening elements. Engine masses and nacelle aerodynamic loads are not included but leading and trailing edge flap panel masses are modeled using Concentrated Mass Element Connection (CONM2) lumped masses connected with Interpolation Constraint Elements (RBE3). The wingbox layout shown in Figure 6.2 contains 13,878 nodes and 35,509 elements.

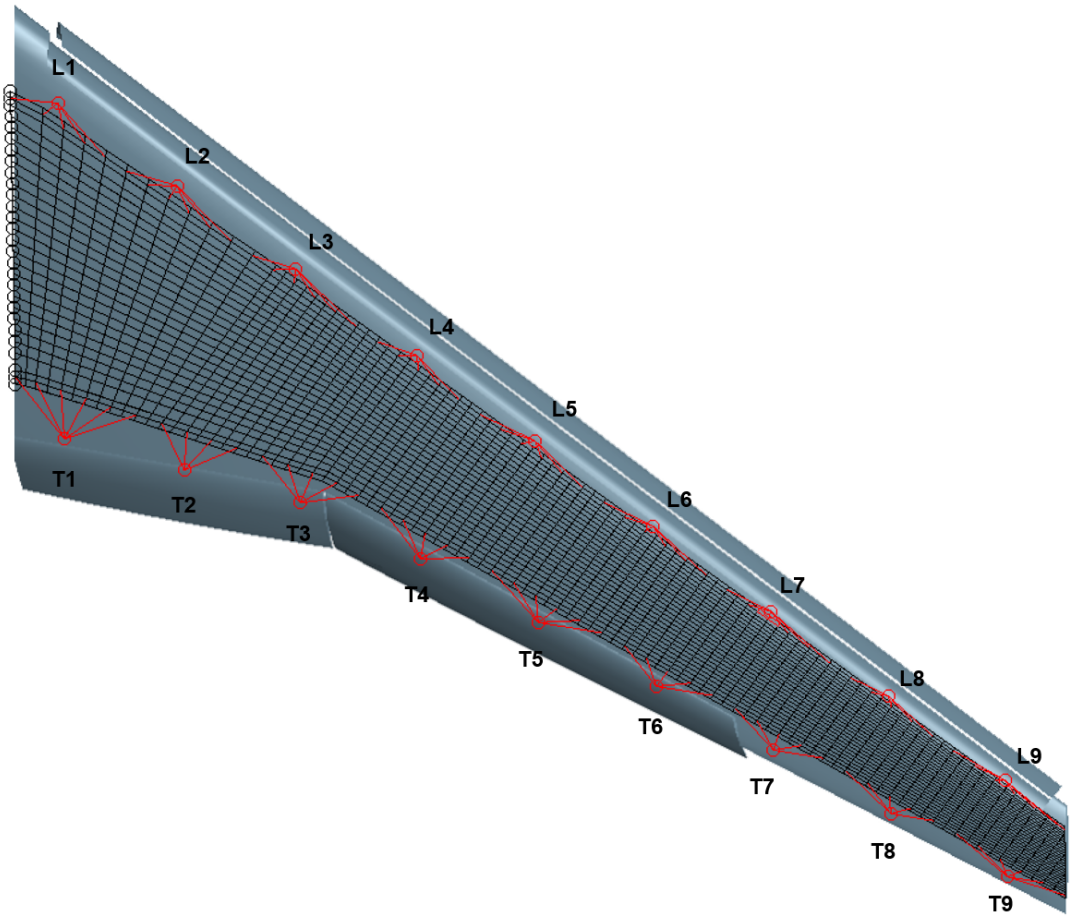

FIGURE 6.1: Finite element model superimposed on the CAD geometry of the NASA HL–CRM, showing the labeled RBE3 nodes on the leading and trailing edges

6.1.1 Structural and Aerodynamic Models

Several aeroelastic analyses were performed during this study with the goal of quantifying the impact of the high–lift actuation system on the dynamic aeroelastic response of the wing at representative flight conditions. The aeroelastic analyses included stability (flutter) and gust responses and were carried out using MSC NASTRAN. The numerical model of the CRM includes both a Finite Element structural model and an overlaying aerodynamic lattice grid, both shown in Figure 6.2. Actuator masses are modeled as additional non–structural lumped masses and are distributed along

TABLE 6.1: Added mass at leading edge nodes for each case

Configuration ID	**Case**	**Number of slat panels**	**Added mass (kg) at each node**								
			L1	**L2**	**L3**	**L4**	**L5**	**L6**	**L7**	**L8**	**L9**
Baseline	N/A	1									
1	N/A	1	6.04								5.58
2	Low mass	2	4.72				9.66				4.30
	Low cost		4.72				9.71				4.99
3	Low mass	4	4.18		8.45		8.29		8.09		3.79
	Low cost		4.18		8.57		8.57		8.57		4.39
4	Low mass	8	3.87	7.81	7.72	7.64	7.59	7.69	7.69	7.38	3.63
	Low cost		3.88	7.88	7.88	7.88	7.88	7.88	7.88	7.88	4.00

TABLE 6.2: Added mass at trailing edge nodes for all cases

Case	**Added mass at each node [kg]**								
	T1	**T2**	**T3**	**T4**	**T5**	**T6**	**T7**	**T8**	**T9**
Baseline									
With TEGRAs	19.66		23.36	15.31		16.69			

the leading and trailing edges of the wing according to the values given in Tables 6.1 and 6.2. The node locations can be seen in Figure 6.1. Kinematic constraints were introduced to represent the structural joint between these added masses and the rest of the wing. The structural joint with the fuselage, instead, is represented as a cantilever constraint at the wing root section (through SPC MSC NASTRAN cards).For cases with more than one slat panel, the 'interior' nodes (nodes except L1 and L9) have an added mass equal to the sum of the two closest leading edge GRAs. The results presented in the upcoming paragraphs were obtained performing the aeroelastic analyses on the CRM model both in its baseline configuration and with all the distributions of added masses on the trailing and leading edge presented respectively in Table 6.2 and 6.1. In MSC NASTRAN, aerodynamic forces are computed with a Doublet Lattice Method (DLM) code in which the flow solution, is represented by a discrete distribution of vorticity, unlike in traditional finite–volume CFD methods. The final solution of aerodynamic forces depends on the intensity of these plainly distributed vortices, and is found by imposing the non–penetration boundary conditions on each aerodynamic panel. Specifically, in the aeroelastic solvers provided by MSC NASTRAN for stability and gust analysis (SOL 145 and SOL 146 respectively) the aerodynamic forces are expressed in the reduced frequency domain as

$$\tilde{f_a} \;=\; q_{dyn}\, Q_{hh}(M,k)\, \tilde{q} \tag{6.1}$$

where Q_{hh} is the Generalized Aerodynamic Forces (GAF) matrix that represents modal forces, dependent on Mach number and reduced frequency, M and k, respectively. The term $\tilde{q}$ is the Laplace transform of the modal coordinates. In addition to this, splines are defined to interpolate aerodynamic forces, which are evaluated on aerodynamic panels, on structural nodes. For reasons of computational costs GAF matrices are computed by MSC NASTRAN on prescribed reduced frequencies, which are given as input through the MKAERO cards. In general, the maximum reduced frequency must always be smaller than a quarter of the chordwise distributed aerodynamic panels, or $k_{MAX} < \frac{\bar{c}}{4\Delta x}$, being Δx is the typical box length. Then an interpolation is performed in order to evaluate forces for all values of k. For the presented test cases, the chosen reduced frequencies are reported in Table 6.3.

TABLE 6.3: List of reduced frequencies, k, at which GAF matrices are computed

Parameter	**Values**											
k	0.0	0.01	0.1	0.11	0.125	0.143	0.167	0.2	0.25	0.33	0.5	1.15

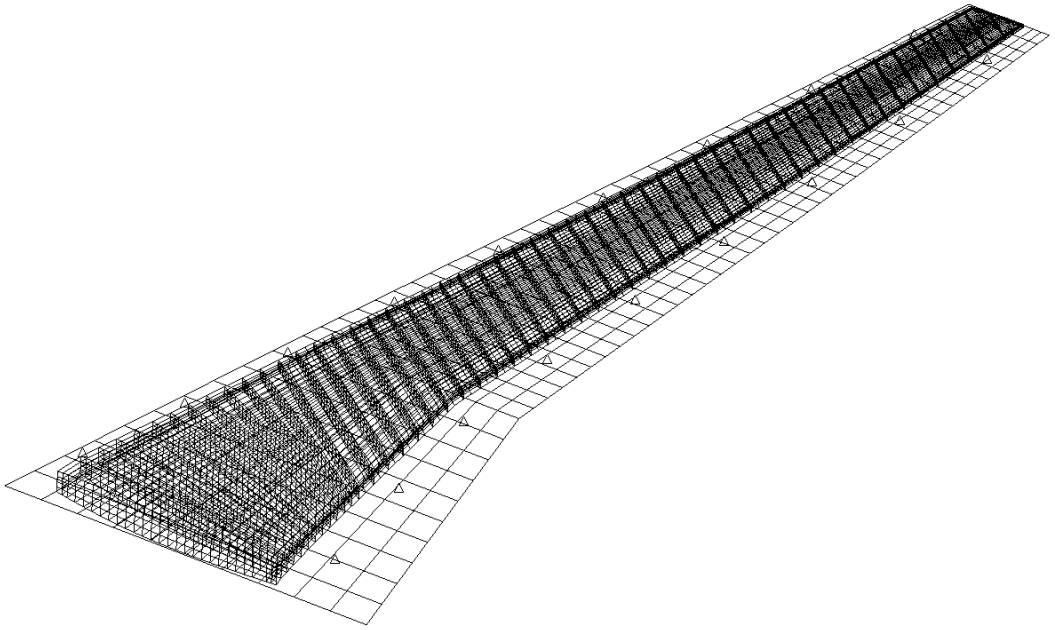

FIGURE 6.2: Structural and aerodynamic mesh of NASA CRM model

6.1.2 Flutter Analysis

By investigating the impact of the mass and placement of the trailing edge high–lift actuators on the clean wing flutter profile, we will be quantifying the impact of low speed regime design decisions on the high speed aircraft performance. As such, this will form one more step in the process of unifying low speed and high speed design regimes. In aeroelasticity there are three main methods to perform a flutter analysis, which are:

- k method
- pk method
- pknl method

Despite being very similar, in some cases they could have slightly different performances, especially for velocities not close to the flutter one. In this study the pknl method was used. It has basically the same approach of the pk, but specialized for constant Mach number. It is generally used in order to evaluate the dependency of dynamic stability on dynamic pressure. Indeed, with a constant Mach and a set of velocities, on the base of a standard atmosphere model one can evaluate stability, in terms of damping ratio and frequency of the aeroelastic modes, over ranges of dynamic pressures representing changes of altitude (like climb or descent manoeuvres).

6.1.3 Gust Response

Gust response analysis was performed using a subset of the Discrete Gust Design Criteria from Certification Specifications and Acceptable Means of Compliance for

Large Aeroplanes (CS-25) [65]. The gust shape follows a "1–cosine" distribution given by

$$U = \begin{cases} \frac{U_{\text{ds}}}{2}\left[1 - \cos\left(\frac{\pi\, s}{H}\right)\right] & \text{for } 0 \leq s \leq 2H \\ 0 & \text{otherwise} \end{cases} \tag{6.2}$$

where s is the distance penetrated into the gust [m], and H [m] is the gust gradient, defined as the distance parallel to the aircraft flight path for the gust to reach its peak velocity. CS–25 specifies H to vary between 9 and 107 m, or between 9 and 12.5 times the mean geometric chord, whichever range is larger. Using mean geometric chord from Table 3.4, this means $9 \leq H \leq 107$ m. The parameter U_{ds} is the design gust velocity in equivalent airspeed, given by:

$$U_{\text{ds}} = U_{\text{ref}}\, F_g \left(\frac{H}{107}\right)^{\frac{1}{6}} \tag{6.3}$$

where U_{ref} is the reference gust velocity and varies with altitude, h, as shown in Figure 6.3a and Equation (6.4). It is derived based on gust velocities which are expected to occur once in 70,000 flight hours.

$$U_{\text{ref}}\,[\text{m/s}] = \begin{cases} 17.07 - 8.005 \times 10^{-4} \cdot h & \text{for } 0 \leq h \leq 4572\,\text{m} \\ 13.41 - 5.140 \times 10^{-4} \cdot (h - 4572) & \text{for } 4572 < h \leq 18,288\,\text{m} \end{cases} \tag{6.4}$$

The term F_g is the flight profile alleviation factor, and has the effect of reducing U_{ref}. As the aircraft is not flown at any altitude 100% of the time, the probability of encountering a U_{ref}–sized gust can be reduced proportionately. This parameter depends on the maximum operating altitude, Z_{mo} [m], the ratio of the maximum landing weight (MLW) to the maximum take–off weight (MTOW), R_1, and the ratio the maximum zero–fuel weight (MZFW) to MTOW, R_2. This is quantified as

$$F_g = \frac{1}{2}\left[1 - \frac{Z_{mo}}{76,200} + \sqrt{R_1 \tan\left(\frac{\pi}{4} R_2\right)}\right] \tag{6.5}$$

The commercial aircraft analogue of the CRM used throughout this study is the Boeing 777–200. Using the values of MTOW, MZFW, and MLW from Table 3.4, $R_1 = 0.817$ and $R_2 = 0.789$. Maximum operating altitude for the 777-200 is stated in [84] as $Z_{mo} = 13,100$ m, giving a value of $F_g = 0.796$. Combining Equations (6.4) and (6.5) with Z_{mo} allows for a complete picture of the range of gust velocities to be considered within the flight envelope. The shaded area in Figure 6.3a shows this range. Gusts beyond the vertical line on the right do not need to be considered because this is beyond the maximum operating altitude of the aircraft. In the area below the shaded region, gusts are spatially short and of low intensity to not cause any relevant structural response. Gusts in the area above the shaded region are spatially long and temporally slow, producing more relevant problems to trajectory tracking than structural loads alleviation. Figure 6.3b shows a range of gust profiles, H, from 9 to 107 m for sea level and Z_{mo}. These gust profiles can be thought of as vertical "slices" through the shaded area of Figure 6.3a. For the sea level and Z_{mo} range in Figure 6.3b, these are plots of sections A–A and B–B in Figure 6.3a, respectively.

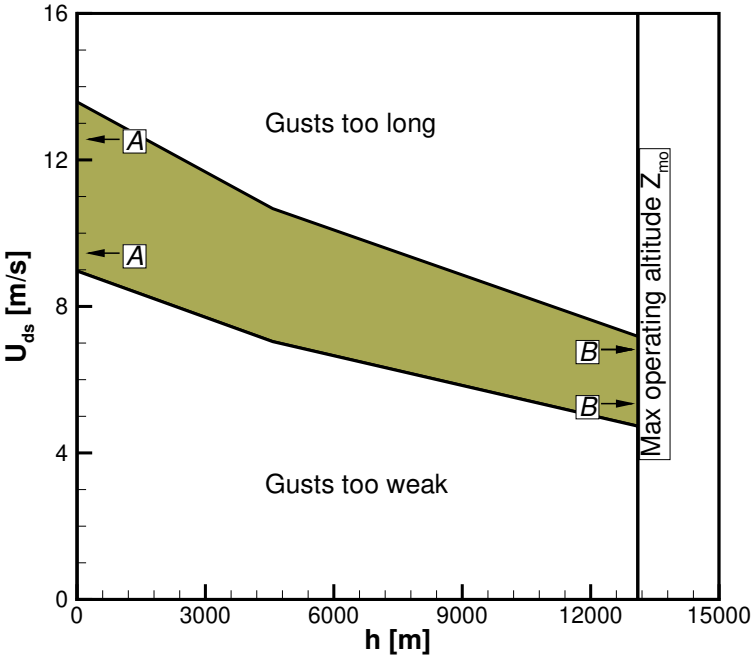

(A) Variation of design gust velocity with altitude for two different gust gradient lengths.

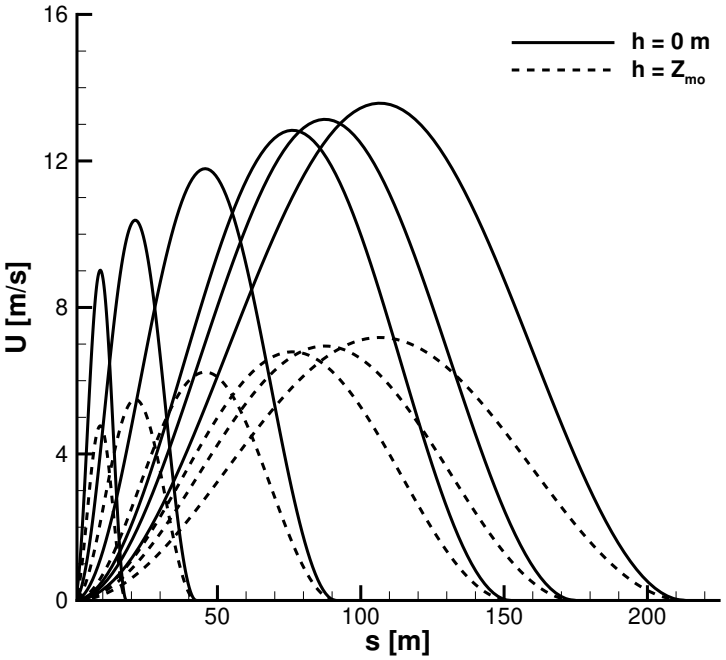

(B) Range of gust profiles required for NASA CRM at sea level.

FIGURE 6.3: Design gust velocity variation and profile.

6.2 Results

This Section deals with the aeroelastic results obtained with the NASA CRM model. First, aeroelastic stability is investigated, comparing the baseline configuration with the proposed ones. Then, the gust loads analysis is performed, considering first a comprehensive range of gust wavelengths and then picking the most significant of them to carry out an investigation on how the proposed configurations impact the dynamic aeroelastic response. For all cases, the original CRM model is taken to be the "baseline configuration". Additional cases were run to assess the impact of the high–lift actuator masses. Each additional case corresponds to a particular configuration, combining different actuator masses, different design philosophies, and mass distributions.

6.2.1 Flutter Analysis

The results presented in this study are obtained with both Mach and velocity constant and equal to $M = 0.85$ and $U_\infty = 289$ m/s, respectively. The range of density (analogous to altitude on the base of a Standard Atmosphere model) defines the dynamic pressure, q, which spans 0 to 68.9 kPa, covering the full range of possible flight conditions, and a considerable extent of unrealistic flight conditions (a Mach 1 flow at sea level conditions is approximately $q = 71$kPa). The baseline configuration is first considered. The stability plots are shown in Figure 6.4 in terms of damped frequency, f, and damping ratio, g. Some branches of these graphs show discontinuities, which in these cases could be due to the rough and not homogeneous distribution of reduced frequencies, which could imply a badly performing interpolation. Although a finer distribution of reduced frequencies could be defined for smoother plots, this is far from the main goal of this study, which is mainly focused on investigating the effect on flutter dynamic pressure and frequency of the proposed actuators design. It is not unexpected to find that at low altitudes, i.e. on the lower end of the dynamic pressure range, the modeshapes are uncoupled and their frequencies match those of the structural model. The increasing dynamic pressure has a coupling effect between structure and fluid. The aeroelastic plant is found to lose its stability, for the baseline configuration, at $q = 51.25$ kPa, where the damping ratio becomes positive[1], as highlighted in Figure 6.4b, at a corresponding frequency $\omega = 4.86$ Hz. One observes an increasing coupling between second bending and torsional mode around flutter, as showed by the sudden veering of the damping ratio plot.

The eigenvalue traces were computed for all the high–lift configurations. It is found out that all of them lead to almost the same results. Attention is mainly focused on the aeroelastic root which leads to instability, which is put in comparison with the result obtained with the baseline model, as shown in Figure 6.5. Here, only the 8 slat configuration (with the low cost design approach) is representative of all the proposed ones, because of the almost perfectly overlaying plots. This is also shown in Table 6.4, where the reported percentage variations of flutter dynamic pressure and damped modeshape frequency with respect to the baseline ones are nearly the same. Two observations are worth mentioning. First, independently on the arrangement of high–lift actuator added masses, the instability of the aeroelastic plant is found to be postponed for all cases. This is a first indication that these lumped masses have a beneficial impact on the aeroelastic characteristics. The second observation is for the trend of the modeshapes at subcritical dynamic pressures. At low dynamic pressures, the damping ratio appears to be slightly smaller in module compared to the baseline configuration, while approaching the critical point (as soon as the eigenvalue

[1]Damping, in this analysis, is the ratio of real over imaginary part of the aeroelastic eigenvalue.

trace starts veering) the effect of coupling between fluid and structure appears to increase the absolute value of it (which then leads to a "delayed" flutter). Modeshape frequency, on the other hand, appears to be smaller on all the range of dynamic pressure, even at the bottom end of it, where the eigenvalue is representative of the structural normal modes (again unsurprising because of the extra weight). This gives a preliminary idea of how these high–lift actuator masses will impact the gust response, which is described in the upcoming paragraph.

TABLE 6.4: Percentage change in flutter dynamic pressure and frequency for each GRA mass configuration compared to baseline

Configuration	**Dynamic pressure**		**Frequency**	
	Low cost	**Low mass**	**Low cost**	**Low mass**
1	+3.99%	+3.99%	-4.689%	-4.689%
2	+3.99%	+3.99%	-4.695%	-4.690%
3	+3.99%	+3.99%	-4.694%	-4.688%
4	+3.99%	+3.99%	-4.689%	-4.682%

6.2.2 Gust Response

Gust load analyses is now presented. Although the full range of gust profiles need to be considered for certification purposes, most attention is paid to the 25-chord length one, corresponding to a gust gradient distance, H, of 12.5 times the MAC. Empirical data has shown that legacy aircraft demonstrate critical response at close to this gust length [86]. For the CRM with MAC $= 7m$, this corresponds to $H = 87.5$ m and is the gust length that has been used in the analysis. Figure 6.6 shows the response of the baseline CRM wing to a selection of gust inputs within the specified certification range. The red line shows the 25-chord gust wavelength, the response to which demonstrates the least damping (subsequent peaks are higher than with other wavelengths).

The gust responses here presented are obtained setting a dynamic pressure of 12.22 kPa, corresponding to an altitude of $7,620$ m, where the gust amplitude is evaluated according to the CS-25 regulations aforementioned. This flight condition roughly represents something close to a cruise condition.

From a structural engineering viewpoint, it is interesting to evaluate the response of the structure to a vertical gust in terms of wing root bending moment and torque, which are critical parameters to be considered when sizing structural elements of a wing. In the FE model, the wing is clamped at its root section in such a way to represent the rigid joint to the fuselage. The support reactions at this particular location are analysed in order to evaluate the effects of the gust. In particular, it is interesting to compare the response between the baseline configuration and the newly proposed ones with high–lift actuation devices, as shown in Figure 6.7, illustrating the time history of the structural response. The amplitude of the first peak in the oscillatory behaviour of the structural is particularly interesting because it tells the maximum stress experienced by the structure when a gust occurs. The results prove that all the proposed configurations provide structural benefits, showing a non negligible load alleviation both on wing root bending moment and torque, as highlighted both in Figure 6.7 and 6.8, which is nearly the same for both the proposed design philosophies. The variation of the damping ratio and frequency associated to the bending mode eigenvalues described in the previous section is here confirmed by the time history of bending moment. Indeed, one can observe that although the load alleviation at the

maximum amplitude of the response, the following oscillations suggest a less damped behaviour, as well as a slightly lower frequency.

Table 6.5 quantifies the percentage reductions of the maximum wing root bending moment and torque with respect to the baseline configuration. The trend towards a smaller change in peak bending moment torque is seen with increasing number of leading edge slats. This is due to the increased added mass at the leading edge when more slats are included.

TABLE 6.5: Percentage change in maximum bending moment and torque for each GRA mass configuration compared to baseline

Configuration	**Bending moment**		**Torque**	
	Low cost	**Low mass**	**Low cost**	**Low mass**
1	-1.224%	-1.203%	-1.415%	-1.387%
2	-1.444%	-1.158%	-1.327%	-1.344%
3	-1.103%	-1.116%	-1.283%	-1.302%
4	-1.087%	-1.104%	-1.284%	-1.299%

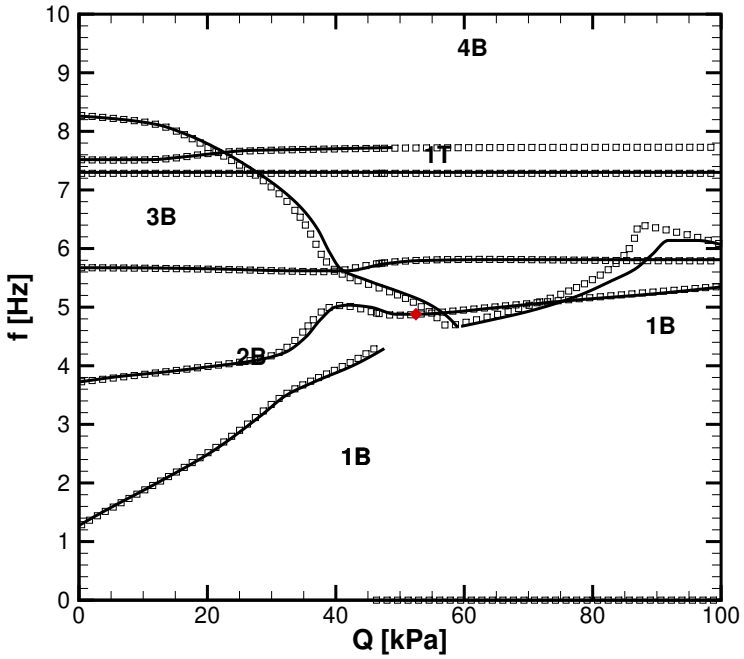

(A) Damped natural frequency, f

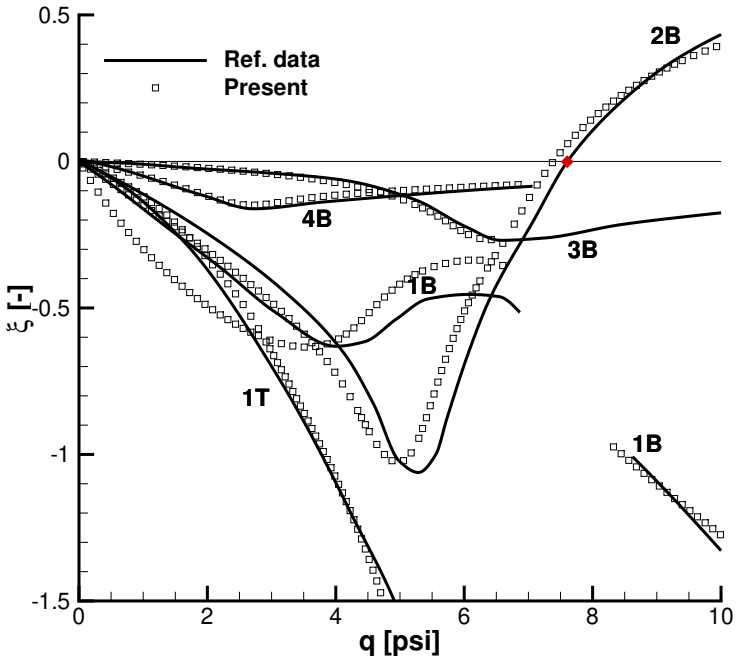

(B) Damping ratio, ξ

FIGURE 6.4: Eigenvalue traces for CRM baseline wing in comparison to reference data in [83][85]. "T" denotes a torsional mode, and "B" a bending mode.

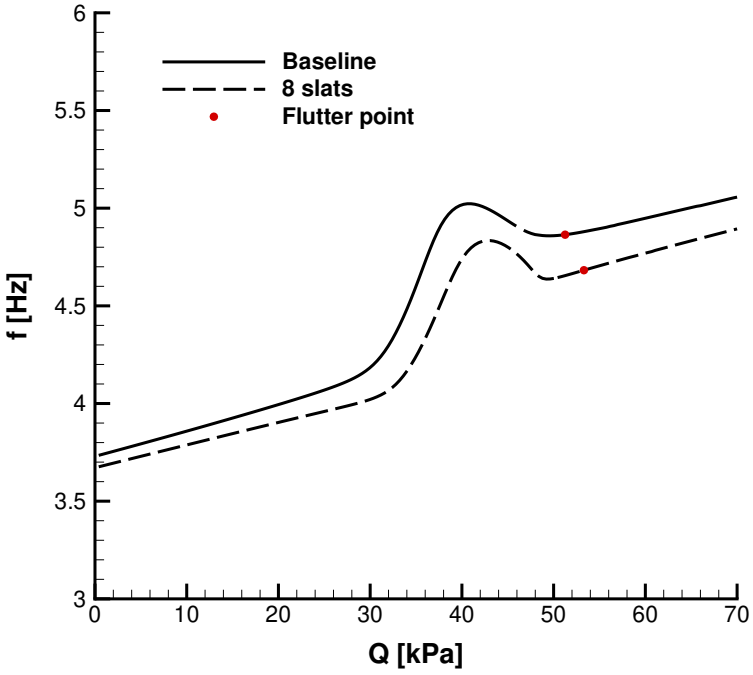

(A) Damped natural frequency, f

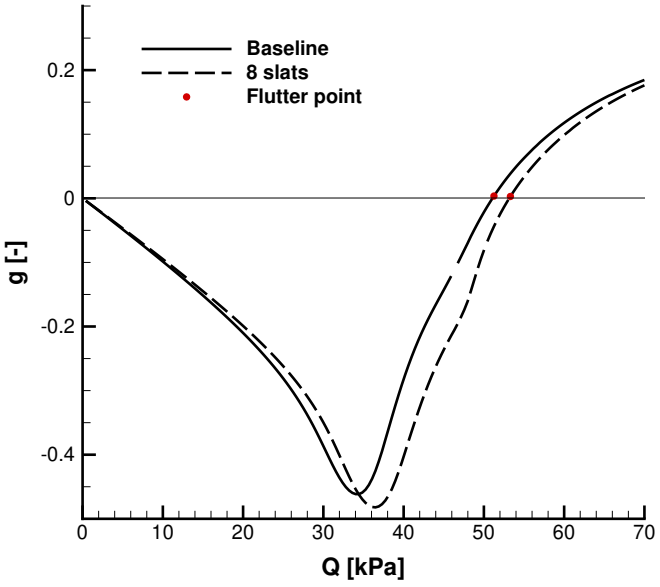

(B) Damping ratio, ξ

FIGURE 6.5: Eigenvalue traces for the 2nd bending mode in the baseline and 8 slat (low cost) configurations. Traces for other configurations were identical to the 8 slat case.

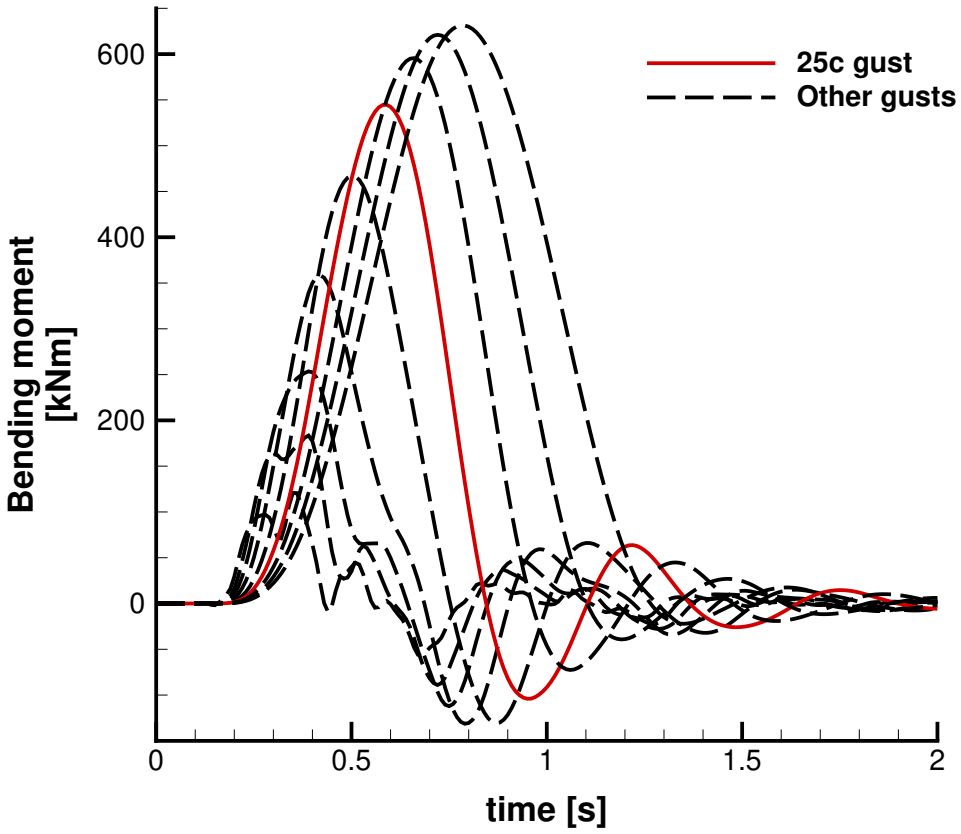

FIGURE 6.6: Gust responses to certification range of values at $q =$ 12.01kPa and $M = 0.85$. The 25c gust wavelength (red) is the least damped and close to the largest.

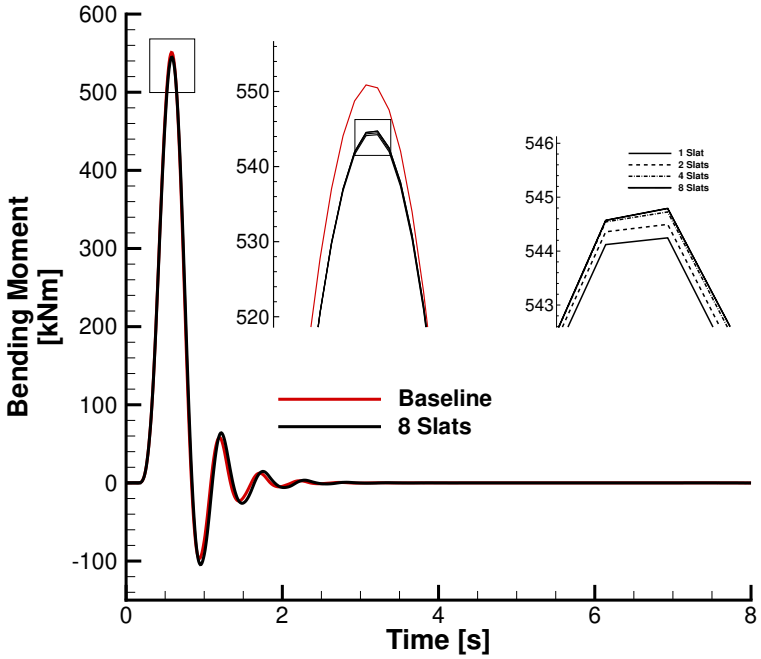

(A) Low cost leading edge actuators

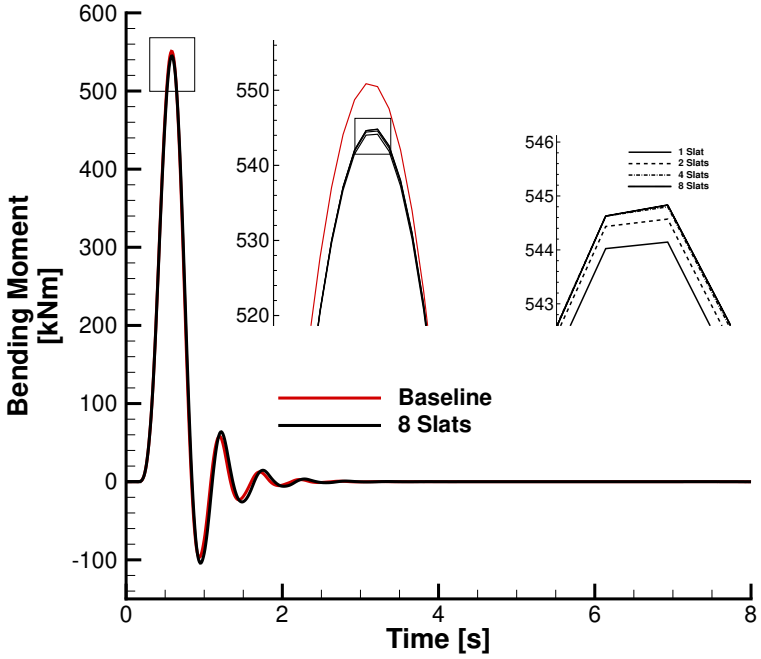

(B) Low mass leading edge actuators

FIGURE 6.7: Comparison of peak gust response in wing root bending for low cost and low mass leading edge design philosophies

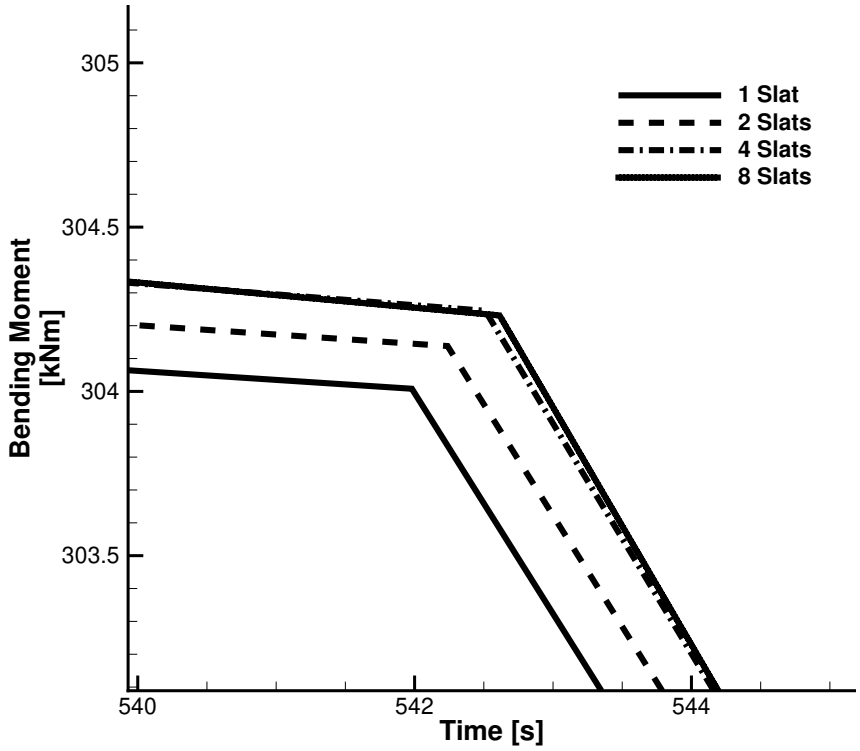

(c) Low cost (detail).

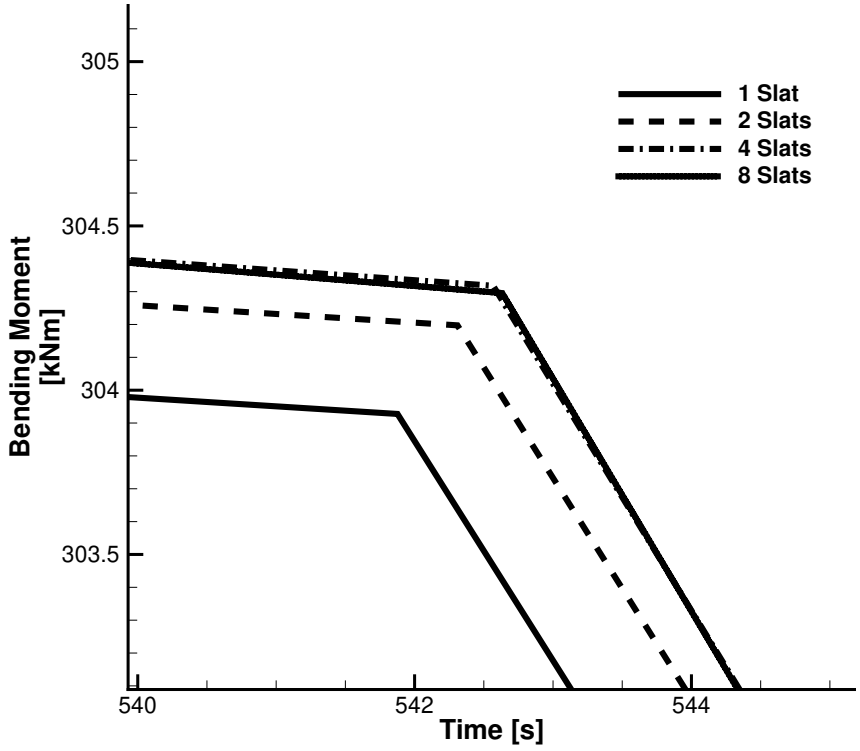

(d) Low mass (detail).

FIGURE 6.7: Gust response comparison to baseline case of different slat configurations for wing root bending moment.

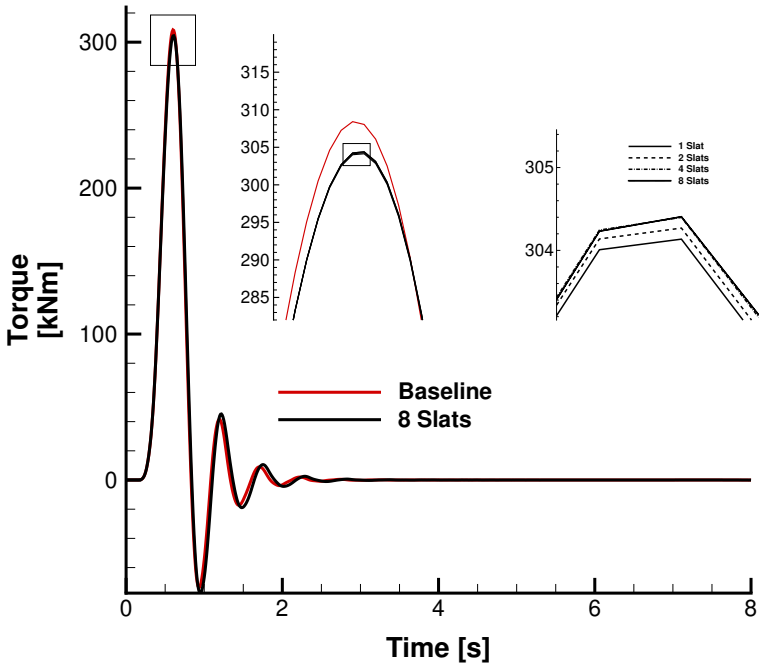

(A) Low cost leading edge actuators

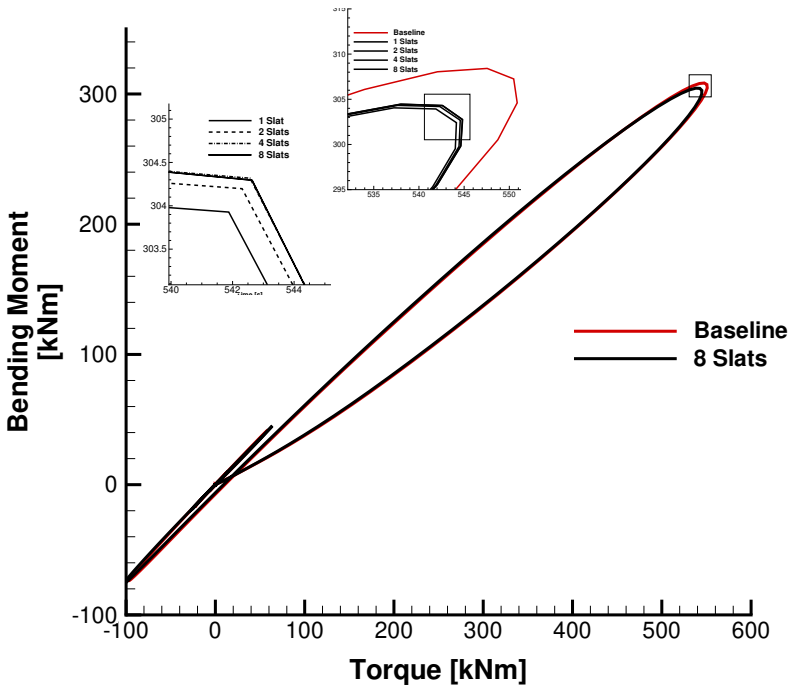

(B) Low mass leading edge actuators

FIGURE 6.8: Gust response comparison to baseline case of different slat configurations for wing root torque

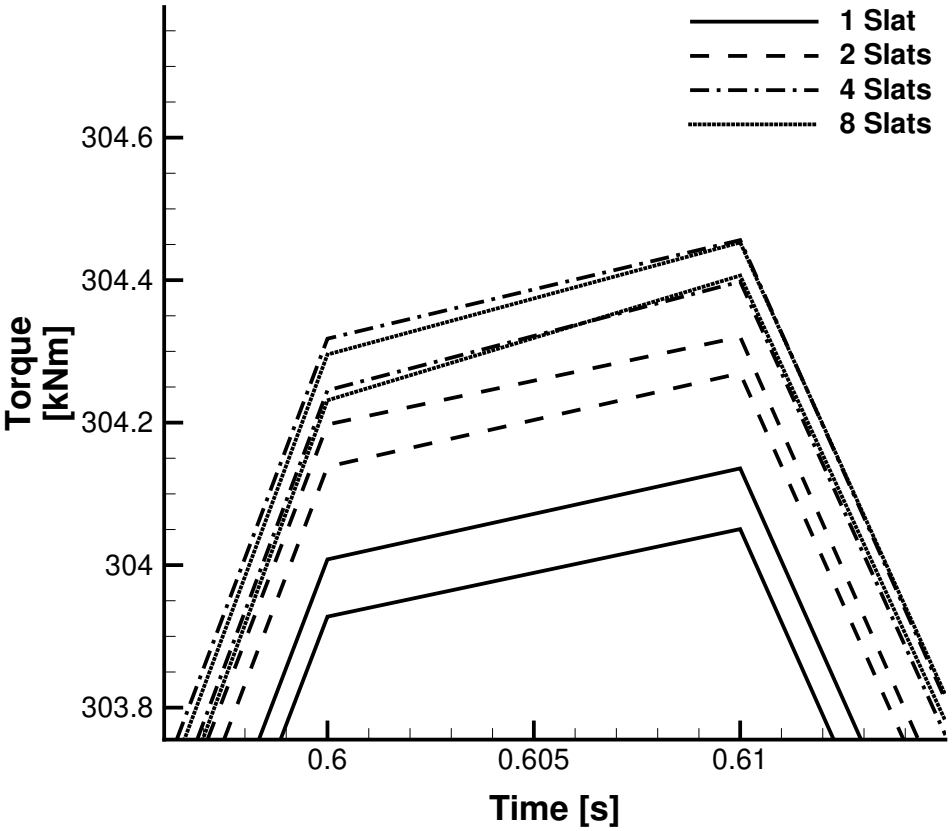

(c) Comparison of peak gust response in wing root bending for low cost and low mass leading edge design philosophies

FIGURE 6.8: Gust response comparison to baseline case of different slat configurations for wing root torque

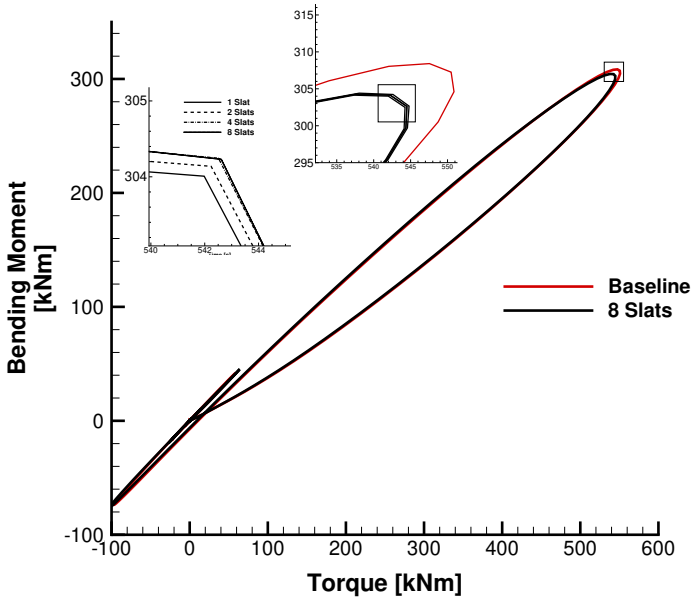

(A) Low cost configurations

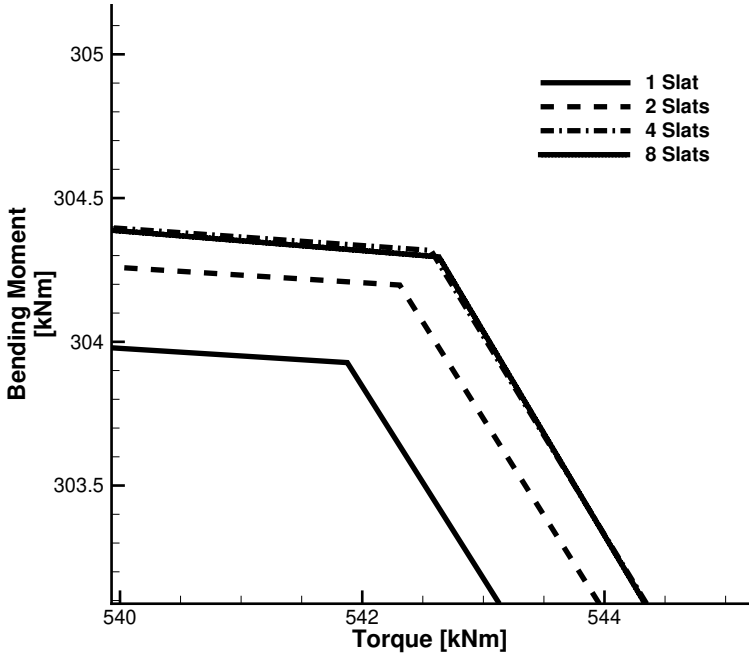

(B) Low mass configurations

FIGURE 6.9: Locus of bending moment–torque values for the full time history of the gust response

6.3 Conclusions

It was found that all high–lift mass configurations had the effect of increasing the dynamic pressure flutter dynamic by approximately 4%. The added high–lift actuation mass was also found to have a disproportionately large gust load alleviating effect for gusts of length 25 times the MAC. In these cases wing root bending moment and torque were reduced by 1.3-1.5% compared to the aeroelastic model without added masses. This result is meaningful because it demonstrates that peak loads during gust encounters are smaller due to the added masses of the high–lift system, which play the benign effect of a passive loads reduction mechanism. As a result, the occurrence of flutter and the gust loads analyses can be carried out more accurately, combining low–speed characteristics in assessing high–speed performances. The caveat in doing this is the ability to estimate the high–lift masses, first, and then to include such non–structural masses into the various analyses of the design process.

Chapter 7

Conclusions and Future Work

7.1 Project summary

The research detailed within this thesis has been primarily focused on developing a method of high-lift actuation sizing early in the aircraft design cycle, and demonstrating a method of performing the necessary loads calculations using low cost methods. An application of this capability was demonstrated by using the actuation sizing data to quantify the dynamic aeroelastic response of the wing. It was shown that the large trailing edge GRAs required for the flap surfaces had a positive impact on the dynamic aeroelastic phenomena of gust and flutter.

7.2 Part I: A priori high–lift system sizing using industrial data

In Chapter 3, actuation weight and size data provided by Moog Aircraft Group was used to make a series of correlations between design torque and mass/volumetric size. These correlations were then used in combination with the high-lift actuation design philosophy to demonstrate a method of estimating the all-up high-lift actuation weight from the high-lift surface aerodynamic loads. A comparison was made to a real aircraft (COMAC C919) for which the high-lift deployment loads and final actuation weight were both known. These demonstrated good agreement, albeit with fairly significant error bars, as shown in Figure 3.7. The error bar extent was caused by the large uncertainty in mass of the GRAs for a given rated output torque (i.e. significant scatter seen in Figure 3.4).

The optimality of a wing design depends considerably on the weight and the aerodynamics. Work by Martins et al. [87] and others uses high-fidelity RANS CFD and FEM with coupled-adjoints to accurately predict the aerodynamic performance and load-bearing weight of the wing structure, but use crude methods based only on wing area to estimate the secondary wing weight. These optimisation approaches lack consistency in fidelity, which increases uncertainty assessing the optimal configuration.

Furthermore, there is distinct lack of consideration for the high–lift design at the concept phase and with the MDO community. As an example, Bons et al. [25] produced a high-fidelity aerodynamic shape optimization of a full configuration regional jet which included "*consider[ing] the impact of adding constraints such as climb rate, take–off field length, and buffet onset margin*". In order to assess the TOFL and LFL, some prediction of the aerodynamic performance of the aircraft in a high–lift configuration was required. As no high–fidelity model of the high–lift devices was available, conceptual–level, parameter–based formulae from common aircraft design references to estimate lift and drag were opted for. There is therefore a clear requirement for

a fidelity–consistent approach to incorporate the high–lift design and weight estimation early in the design cycle to allow a designer to understand the impacts of design decisions on the all–up wing weight which has been demonstrated in this chapter.

7.3 Part II: High-lift panel loads estimation using low-cost methods

The method for estimating high-lift panel hinge moments in Part I suffers from the high computational cost associated with performing full 3D CFD simulations. This makes it unsuitable for preliminary aircraft design, where low computational cost tools are essential to exploring a large design space. Reducing this computational cost motivated this part of the work.

Hinge moment estimates were made using a comparatively low computational cost method, involving only 2D computations. Six 2D chordwise sections were taken at 6 different spanwise locations, and their geometries were meshed using the best practice methods from Chapter 4. These grids were then used to compute a database of viscous lift polars. A Vortex Lattice grid was made from the planform shape of the wing, and the viscous database and the vortex lattice were used as inputs to the Southampton multi–fidelity solver. Lift polars computed using the Southampton multi–fidelity solver were compared to 3D values and showed good agreement. The convergence limit of the Southampton multi–fidelity solver was then used to estimate the sizing flow condition of the CRM and this was compared to the sizing flow condition estimated using 3D CFD, demonstrating good agreement. Finally, a technique to integrate the sectional force data along the wing, taking into account wing geometry and effective angle–of–attack, α_{eff}, was introduced. This produced estimates of the hinge moments at a small computational cost compared to the corresponding values obtained with 3D CFD.

7.4 Part III: Impact of high-lift actuation on dynamic aeroelastic response

An estimate of the masses of the leading and trailing edge geared rotary actuators for a hypothetical high–lift system of the NASA Common Research Model were made. Various GRA mass configurations have been used in conjunction with a finite element model of the CRM wing in an attempt to quantify the impact of these masses on the dynamic aeroelastic phenomena of flutter and gust response. It was found that all high–lift mass configurations had the effect of increasing the flutter dynamic pressure by approximately 4%. The added high–lift actuation mass was also found to have a disproportionately large gust load alleviating effect for gusts of length 25 times the mean aerodynamic chord. In these cases wing root bending moment and torque were reduced by 1.3-1.5% compared to the aeroelastic model without added masses. This result is meaningful because it demonstrates that peak loads during gust encounters are smaller due to the added masses of the high–lift system, which have the effect of a passive loads reduction mechanism. As a result, the occurrence of flutter and gust load analyses can be carried out more accurately earlier in the design cycle, combining low–speed characteristics (high–lift design) in assessing high–speed performances (gust and flutter).

As gust loading represents one of the critical loads cases which are used to size the aircraft structure, the $\approx 1\%$ wing root bending moment alleviation seen when high-lift actuator masses are included allow for a potential reduction in structural weight commensurate with this peak stress reduction.

7.5 Future work

7.5.1 Part I: A priori high–lift system sizing using industrial data

Future work includes better understanding the cause of the PDU and GRA mass scatter, and whether certain data points can be discarded due to e.g. particular design constraints imposed on outlier GRAs. This level of detail would require further collaboration with Moog but will allow for a tightening of the mass estimate error bars. The actuation mass estimation methodology could be further refined by better understanding how the all-up actuation mass is related to the total GRA/PDU mass. As outlined in Section 3.1.3, Moog provided information that "*GRA and PDU weight makes up approximately 68% and 52% of the trailing edge and leading edge actuation weight respectively*". Whether this holds true across a wide range of aircraft sizes and architectures is not clear and a refinement of the methods to scale up GRA and PDU mass to the all-up actuation mass would further reduce the uncertainty.

A further verification of the end-to-end method with the Airbus XRF-1 would be extremely beneficial. The Airbus XRF-1 is extremely similar to the real Airbus A330, for which the actuation system weight will be known by Airbus. This would allow for an estimate to be made using loads calculated from the high-definition geometry available for this research model. The corresponding actuation weight estimation could then be compared to the Airbus A330 value.

7.5.2 Part II: High-lift panel loads estimation using low-cost methods

The proof of concept showed considerable promise, with the hinge moment estimates about 30% below that of the 3D estimate for Flap 1 and the Slat. The value for Flap 2 was $5\times$ too small, but time constraints prevented a proper investigation of causes of this discrepancy. Future work will include investigating the impact on the hinge moment estimate of:

- Different VLM geometries including spanwise twist, separate lattices to represent the high-lift surfaces, and different mesh densities.
- Increasing the number of spanwise viscous lift sections. Although the goal is to accomplish the hinge moment estimate with as little computational overhead as possible, as part of the investigation into the limitations of the model, knowledge of the impact of quantity of sections will be gathered.

Further verification of the method will take place at more moderate angles–of–attack where the conditions are further away from the numerical instabilities seen at these extreme values of α.

7.5.3 Impact of high-lift actuation on dynamic aeroelastic response

Further work is needed to refine the mass estimates of the GRAs and to include other actuation weight such as torque tubes, angled gear boxes and wing-tip brakes into

the added mass model. A larger range of gust profiles will also be considered as part of the further work to understand how much these added masses alleviate gust loads for other cases. However, the work presented here has demonstrated the importance of having reliable leading and trailing edge mass estimates as early as possible in the design cycle. Accurately quantifying these could allow lighter wing structures, owing to the reduced uncertainty the peak loads encountered during the gusts that typically dictate the structural sizing of an aircraft wing.

Higher fidelity structural models such as the semi-open source Airbus XRF-1 model would also be a worthwhile future effort. Computing the gust and flutter effects using higher fidelity URANS CFD calculations instead of the VLM would provide more confidence in the results.

7.6 Research output

The high lift actuation sizing methodology was presented at the AIAA SciTech Forum, January 2020 [1].

The robust multi-element mesh generation for 2D viscous lift computation was presented at the AIAA Aviation Forum special session on n Mesh Effects for CFD Solutions, June 2020 **Moss2020b**.

The impact of high-lift actuator sizing on dynamic aeroelasticity was presented at the AIAA SciTech Forum, January 2021 [3].

The author contributed to the peer-reviewed paper on iterative errors in unsteady simulations presented in the Journal of Verification, Validation and Uncertainty Quantification [88].

Bibliography

[1] B. R. Moss, A. Da Ronch, and N. Tyler, "High-Lift Actuation Weight Estimation using Low Cost Methods," AIAA, 2020.

[2] B. R. Moss, A. K. Bagheri, and A. D. Ronch, "Effect of mesh characteristics on the flow solutions around a multi–element airfoil using su2," in *AIAA AVIATION 2020 FORUM*. DOI: 10.2514/6.2020-3218. eprint: https://arc.aiaa.org/doi/pdf/10.2514/6.2020-3218. [Online]. Available: https://arc.aiaa.org/doi/abs/10.2514/6.2020-3218.

[3] B. R. Moss, A. D. Ronch, and C. Conti, "Quantifying the impact of high-lift actuator mass on dynamic aeroelasticity for the nasa common research model," in *AIAA Scitech 2021 Forum*. DOI: 10.2514/6.2021-0907. eprint: https://arc.aiaa.org/doi/pdf/10.2514/6.2021-0907. [Online]. Available: https://arc.aiaa.org/doi/abs/10.2514/6.2021-0907.

[4] Airbus, "Global Networks, Global Citizens: Airbus Global Market Forecast," Tech. Rep., 2018, p. 83. [Online]. Available: https://www.airbus.com/content/dam/corporate-topics/publications/media-day/GMF-2018-2037.pdf.

[5] ——, *Airbus plans to further adapt to COVID-19 environment - Company - Airbus*. [Online]. Available: https://www.airbus.com/newsroom/press-releases/en/2020/06/airbus-plans-to-further-adapt-to-covid19-environment.html (visited on 10/13/2021).

[6] I. A. T. Association. "Climate change: Three targets and four pillars." (2018), [Online]. Available: http://www.iata.org/policy/environment/Pages/climate-change.aspx (visited on 07/12/2019).

[7] E. Weiss, *Defining the Future of Travel | Accenture*. [Online]. Available: https://www.accenture.com/us-en/insights/travel/travel-recovery-new-era (visited on 04/21/2021).

[8] Eurocontrol, "Study into the impact of the global economic crisis on airframe utilisation," Tech. Rep., 2011, p. 40. [Online]. Available: https://www.eurocontrol.int/sites/default/files/content/documents/official-documents/facts-and-figures/coda-reports/study-impact-global-economic-crisis-2011.pdf.

[9] M. Drela, "Low Order Aeromechanical Modeling for Conceptual Design of Fuel-Efficient Aircraft," *Eighth International Conference on Flow Dynamics*, 2011.

[10] J. D. Anderson, *Modern compressible flow with historical perspective*, 3rd ed. McGraw Hill, 2003.

[11] C Irving, *Wide-body: the triumph of the 747*. W. Morrow, 1993, ISBN: 9780688099022.

[12] P. Piperni, A. DeBlois, and R. Henderson, "Development of a Multilevel Multidisciplinary-Optimization Capability for an Industrial Environment," *AIAA Journal*, vol. 51, no. 10, pp. 2335–2352, 2013. DOI: 10.2514/1.J052180.

[13] M Butchers, "Uncertainty quantification & management in high value manufacturing special interest group, Annual 485 Report," *The Knowledge Transfer Network*, vol. 486, 2015.

[14] C. P. van Dam, J. C. Vander Kam, and J. K. Paris, "Design-Oriented High-Lift Methodology for General Aviation and Civil Transport Aircraft," *Journal of Aircraft*, vol. 38, no. 6, pp. 1076–1084, 2001. DOI: 10.2514/2.2875.

[15] A. Rizzi, "Modeling and simulating aircraft stability and control - The SimSAC project," *Progress in Aerospace Sciences*, vol. 47, no. 8, pp. 573–588, 2011. DOI: 10.1016/j.paerosci.2011.08.004.

[16] P. R. Spalart, "Strategies for turbulence modelling and simulations," *International Journal of Heat and Fluid Flow*, vol. 21, no. 3, pp. 252–263, 2000, ISSN: 0142727X. DOI: 10.1016/S0142-727X(00)00007-2.

[17] R. M. Cummings, W. H. Mason, S. A. Morton, and D. R. McDaniel, *Applied Computational Aerodynamics: A Modern Engineering Approach*, ser. Cambridge Aerospace Series. Cambridge University Press, 2015. DOI: 10.1017/CBO9781107284166.

[18] L. Eça, G. Vaz, M. Hoekstra, S. Pal, E. Muller, D. Pelletier, A. Bertinetti, R. Difonzo, L. Savoldi, R. Zanino, A. Zappatore, Y. Chen, K. J. Maki, H. Ye, J. Drofelnik, B. Moss, and A. Da Ronch, "Overview of the 2018 Workshop on Iterative Errors in Unsteady Flow Simulations," *Journal of Verification, Validation and Uncertainty Quantification*, vol. 5, no. 2, Aug. 2020, 021006, ISSN: 2377-2158. DOI: 10.1115/1.4047922. eprint: https://asmedigitalcollection.asme.org/verification/article-pdf/5/2/021006/6561613/vvuq_005_02_021006.pdf. [Online]. Available: https://doi.org/10.1115/1.4047922.

[19] F. Palacios, J. Alonso, K. Duraisamy, M. Colonno, J. Hicken, A. Aranake, A. Campos, S. Copeland, T. Economon, A. Lonkar, T. Lukaczyk, and T. Taylor, "Stanford University Unstructured (SU^2): An open-source integrated computational environment for multi-physics simulation and design," in *51st AIAA Aerospace Sciences Meeting including the New Horizons Forum and Aerospace Exposition*, American Institute of Aeronautics and Astronautics, 2013. DOI: 10.2514/6.2013-287. [Online]. Available: https://doi.org/10.2514/6.2013-287.

[20] DLR, *TAU-Code User Guide*, 2017.

[21] J. Katz and A. Plotkin, *Low-Speed Aerodynamics*, ser. Cambridge Aerospace Series. Cambridge University Press, 2001, ISBN: 9780521665520. [Online]. Available: https://books.google.co.uk/books?id=rAS1DmBRLo8C.

[22] J. Katz and A. Plotkin, *Low-Speed Aerodynamics*, 2nd Ed. Cambridge University Press, 2001, ISBN: 0-521-66219-2.

[23] G. K. W. Kenway and J. R. R. A. Martins, "Multipoint Aerodynamic Shape Optimization Investigations of the Common Research Model Wing," *AIAA Journal*, vol. 54, no. 1, pp. 113–128, 2015. DOI: 10.2514/1.j054154.

[24] J. R. R. A. Martins, G. K. W. Kenway, and T. Brooks, "Multidisciplinary Design Optimization of Aircraft Configurations Part 2: High-fidelity aerostructural optimization," no. May, pp. 1–47, 2017. DOI: 10.2514/3.45532.

[25] N. Bons, C. A. Mader, J. Martins, A. Cuco, and F. Odaguil, "High-Fidelity Aerodynamic Shape Optimization of a Full Configuration Regional Jet," *2018 AIAA/ASCE/AHS/ASC Structures, Structural Dynamics, and Materials Conference*, no. January, pp. 1–14, 2018. DOI: 10.2514/6.2018-0106. [Online]. Available: https://arc.aiaa.org/doi/10.2514/6.2018-0106.

[26] P. K. C. Rudolph, "High-Lift Systems on Commercial Subsonic Airliners," *NASA Contractor Report 4746*, 1996.

[27] B. N. Nield, "An Overview of the 777 High Lift Aerodynamic Design," *High Lift and Separation Control Conference*, 1995.

[28] O. Dababneh and T. Kipouros, "A review of aircraft wing mass estimation methods," *Aerospace Science and Technology*, vol. 72, no. January, pp. 256–266, 2018, ISSN: 12709638. DOI: 10.1016/j.ast.2017.11.006.

[29] C. Bai, L. Mingqiang, S. Zhong, W. Zhe, M. Yiming, and F. Lei, "Wing weight estimation considering constraints of structural strength and stiffness in aircraft conceptual design," *International Journal of Aeronautical and Space Sciences*, vol. 15, no. 4, pp. 383–395, 2014, ISSN: 20932480. DOI: 10.5139/IJASS.2014.15.4.383.

[30] *Airbus A320 Specs including the new NEO. - Modern Airliners.* [Online]. Available: https://modernairliners.com/airbus-a320-introduction/airbus-a320-specs/ (visited on 10/13/2021).

[31] G. K. Kenway and J. R. Martins, "Multipoint high-fidelity aerostructural optimization of a transport aircraft configuration," *Journal of Aircraft*, vol. 51, no. 1, pp. 144–160, 2014, ISSN: 15333868. DOI: 10.2514/1.C032150.

[32] S. I. PAI and W. R. SEARS, "Some aeroelastic properties of swept wings," *Journal of the Aeronautical Sciences*, vol. 16, no. 2, pp. 105–115, 1949. DOI: 10.2514/8.11736. eprint: https://doi.org/10.2514/8.11736. [Online]. Available: https://doi.org/10.2514/8.11736.

[33] G. J. Kennedy and J. R. Martins, "A parallel aerostructural optimization framework for aircraft design studies," *Structural and Multidisciplinary Optimization*, vol. 50, no. 6, pp. 1079–1101, 2014. DOI: 10.1007/s00158-014-1108-9.

[34] R. Pepper, C. van Dam, and P. Gelhausen, in ser. Multidisciplinary Analysis Optimization Conferences. American Institute of Aeronautics and Astronautics, 2003, ch. Design methodology for high-lift systems on subsonic transport aircraft.

[35] C. Jutte and B. K. Stanford, "Aeroelastic Tailoring of Transport Aircraft Wings: State-of-the-Art and Potential Enabling Technologies," *NASA STI Programme*, no. April, p. 34, 2014.

[36] M. H. Shirk, T. J. Hertz, and T. A. Weisshaar, "Aeroelastic Tailoring - Theory, Practice, and Promise.," *Journal of Aircraft*, vol. 23, no. 1, pp. 6–18, 1986, ISSN: 00218669. DOI: 10.2514/3.45260.

[37] T. A. Weisshaar, *Aircraft Aeroelastic Analysis and Design.* 1995.

[38] P. O. Jemitola and J. P. Fielding, "Conceptual design and optimization methodology for box wing aircraft," *Cranfield University, PhD Thesis*, vol. PhD, p. 210, 2012.

[39] D. Zaccai, "Design Framework for Trailing Edge High-Lift Systems," pp. 1–185, 2014. [Online]. Available: https://repository.tudelft.nl/islandora/object/uuid:40c18b6c-69a4-4365-afbd-4c61f390a522/datastream/OBJ/download.

[40] P. K. C. Rudolph, *Mechanical Design of High Lift Systems for High Aspect Ratio Swept Wings*. 1998, pp. 1–82.

[41] E. Torenbeek, "Development and Application of a Comprehensive, Design-sensitive Weight Predicition Method for Wing Structures of Transport Category Aircraft," TU Delft, Tech. Rep. LR-693, 1992.

[42] K. T. van den Kieboom and A. Elham, "Combined Aerostructural Wing and High-Lift System Optimization," *17th AIAA/ISSMO Multidisciplinary Analysis and Optimization Conference*, 2016. DOI: 10.2514/6.2016-3510.

[43] D. Reckzeh, "Aerodynamic design of the high-lift-wing for a Megaliner aircraft," *Aerospace Science and Technology*, vol. 7, no. 2, pp. 107–119, 2003. DOI: 10.1016/S1270-9638(02)00002-0.

[44] D. Raymer, *Aircraft Design / RDS-Student: A Conceptual Approach*, ser. AIAA Education Series. American Institute of Aeronautics & Astronautics, 2013, ISBN: 9781600869211. [Online]. Available: https://books.google.co.uk/books?id=bvxllgEACAAJ.

[45] R Stanton, "Cargo/Transport Statistical Weight Estimation Equations," Vought Aircraft, Tech. Rep. 2-59320/9R-50549, 1969.

[46] A Jackson, "Preliminary Design Weight Estimation Program," Aero-Commander Div., Tech. Rep. 511-009, 1971.

[47] K. T. van Den Kieboom and A. Elham, "Concurrent wing and high-lift system aerostructural optimization," *Structural and Multidisciplinary Optimization*, 2017. DOI: 10.1007/s00158-017-1787-0.

[48] P. Meredith, "Viscous phenomna affecting high-lift systems and suggestions for future CFD development," *AGARD*, vol. CP315, 1993.

[49] A. Flaig and R Hilbig, "High-lift design for large civil aricraft," *AGARD*, vol. CP515, pp. 31–7, 1993.

[50] C. P. Van Dam, "The aerodynamic design of multi-element high-lift systems for transport airplanes," *Progress in Aerospace Sciences*, vol. 38, no. 2, pp. 101–144, 2002. DOI: 10.1016/S0376-0421(02)00002-7.

[51] J Roskam, *Airplane Design: Preliminary sizing of airplanes*, ser. Airplane Design. Roskam Aviation and Engineering Corporation, 1985. [Online]. Available: https://books.google.co.uk/books?id={_}olYAAAAYAAJ.

[52] E Torenbeek, *Synthesis of Subsonic Airplane Design: An introduction to the preliminary design of subsonic general aviation and transport aircraft, with emphasis on layout, aerodynamic design, propulsion and performance*. Springer Netherlands, 1982, ISBN: 9789024727247.

[53] N. Cumpsty, *Jet Propulsion: A Simple Guide to the Aerodynamic and Thermodynamic Design and Performance of Jet Engines*. Cambridge University Press, 2003.

[54] European Aviation Safety Agency, "Certification Specifications and Acceptable Means of Compliance for Large Aeroplanes 25," p. 885, 2018. DOI: 10.1002/9780470664797.

[55] D. Zaccai, F. Bertels, and R. Vos, "Design methodology for trailing-edge high-lift mechanisms," *CEAS Aeronautical Journal*, vol. 7, no. 4, pp. 521–534, 2016. DOI: 10.1007/s13272-016-0202-7.

[56] S. K. Gupta, A. K. Gupta, and D. Sagar, "Modelling of relative height of hydraulic jump in horizontal prismatic channel using c programming," 2013.

[57] N. Tyler, 2021.

[58] Weimeng. "Comac c919 on airliners.net." (2017).

[59] *3rd AIAA CFD High Lift Prediction Workshop*, 2017. [Online]. Available: https://hiliftpw.larc.nasa.gov/ (visited on 09/02/2019).

[60] *Home*. [Online]. Available: https://commonresearchmodel.larc.nasa.gov/.

[61] Boeing Company, "B777-200 performance summary," Tech. Rep., 2009, pp. 1–11. [Online]. Available: https://thekritic.net/publications/777{_}perf.pdf.

[62] S. M. Tony Sclafani, Jeff Slotnick, Mark Chaffin, Jason Feinman, "3rd AIAA high–lift prediction workshop. Case 1 : Grid Convergence Study," AIAA, Tech. Rep., 2017. [Online]. Available: https://hiliftpw.larc.nasa.gov/Workshop3/HiLiftPW3-Presentations/Summary{_}Case1.pdf.

[63] P. R. Spalart and S. R. Allmaras, "One-equation turbulence model for aerodynamic flows," *Recherche aerospatiale*, no. 1, pp. 5–21, 1994, ISSN: 00341223. DOI: 10.2514/6.1992-439.

[64] J. R. Edwards and S. Chandra, "Comparison of eddy viscosity-transport turbulence models for three-dimensional, shock-separated flowfields," *AIAA Journal*, vol. 34, no. 4, pp. 756–763, 1996, ISSN: 0001-1452. DOI: 10.2514/3.13137. [Online]. Available: https://doi.org/10.2514/3.13137.

[65] EASA, *Certification Specifications for Large Aeroplanes*, 2006. DOI: 10.1002/9780470664797. arXiv: arXiv:1011.1669v3. [Online]. Available: https://www.easa.europa.eu/sites/default/files/dfu/CS-25Consolidatedversion.pdf.

[66] D. S. Lacy, T. B. Company, B. C. Airplanes, T. B. Company, B. C. Airplanes, L. Beach, A. Engineer, P. Development, A. Engineer, and L. Beach, "Development of the High Lift Common Research Model Transonic Transports," no. January, pp. 1–24, 2016. DOI: 10.2514/6.2016-0308.

[67] T. G. H Megson, *Aircraft Structures for Engineering Students*, 4th. 1387, ISBN: 9780750667395.

[68] P. K. C. Rudolph, "High-Lift Systems on Commercial Subsonic Airliners," Tech. Rep. September, 1996, pp. 1–154.

[69] D. Kharlamov, J. Drofelnik, A. Da Ronch, and S. Walker, "Rapid Load Calculations Using an Efficient Unsteady Aerodynamic Solver," *AIAA Aviation Forum*, 2018. DOI: 10.2514/6.2018-3621.

[70] M. Franciolini, A. Da Ronch, J. Drofelnik, D. Raveh, and A. Crivellini, "Efficient infinite-swept wing solver for steady and unsteady compressible flows," *Aerospace Science and Technology*, vol. 72, pp. 217–229, 2018. DOI: 10.1016/j.ast.2017.10.034.

[71] G. Yang, A. Da Ronch, D. Kharlamov, and J. Drofelnik, "Wing twist optimisation using aerodynamic solvers of different fidelity," *31st Congress of the International Council of the Aeronautical Sciences*, no. September, pp. 1–28, 2018.

[72] Pointwise, *Pointwise Software*, 2019. [Online]. Available: https://www.pointwise.com/products/index.html (visited on 11/05/2019).

[73] ——, *Delauny and Advancing Front methods algorithm.* [Online]. Available: https://www.pointwise.com/doc/user-manual/grid/solve/unstructured-domains/attributes-tab/algorithm.html (visited on 05/11/2020).

[74] CFD-online, *Y plus wall distance estimation – CFD-Wiki, the free CFD reference.* [Online]. Available: https://www.cfd-online.com/Wiki/Y{_}plus{_}wall{_}distance{_}estimation (visited on 11/07/2019).

[75] H. Schlichting, *Boundary Layer Theory*, 7th ed. 1979, ISBN: 0-07-055334-3.

[76] J. B. Tseng and C. E. Lan, "Calculation of aerodynamic characteristics of airplane configurations at high angles of attack," NASA, Tech. Rep., 1988. [Online]. Available: https://ntrs.nasa.gov/archive/nasa/casi.ntrs.nasa.gov/19880019507.pdf.

[77] R. J. S. Simpson, R. Palacios, and J. Murua, "Induced-Drag Calculations in the Unsteady Vortex Lattice Method," *AIAA Journal*, vol. 51, no. 7, pp. 1775–1779, 2013. DOI: 10.2514/1.j052136.

[78] D. Schwamborn, T. Gerhold, and R. Heinrich, "The DLR TAU-Code: Recent Applications in Research and Industry," *European Conference on Computational Fluid Dynamics, ECCOMAS CFD 2006*, pp. 1–25, 2006.

[79] J. Drofelnik, D. Kharlamov, and Y. Sun, "Rapid Calculation of Unsteady Aircraft Loads," *6th European Conference on Computational Mechanics*, 2018.

[80] W. Mackie, K. Kagarice, and C. Fast, "Development of a Common Research Model for Applied CFD Validation Studies," Tech. Rep., 2006, pp. 201–202. DOI: 10.1109/ivelec.2006.1666254.

[81] D. S. Lacy and A. J. Sclafani, "Development of the high lift common research model (HL-CRM): A representative high lift configuration for transonic transports," *54th AIAA Aerospace Sciences Meeting*, vol. 0, no. January, pp. 1–24, 2016. DOI: 10.2514/6.2016-0308.

[82] C. V. Jutte, B. K. Stanford, and C. D. Wieseman, "Internal Structural Design of the Common Research Model Wing Box for Aeroelastic Tailoring," NASA, Tech. Rep. March, 2015.

[83] D. S. Lacy, "Common Research Model (CRM) Wingbox Finite Element Models," Tech. Rep., 2015, pp. 2–5. [Online]. Available: https://commonresearchmodel.larc.nasa.gov/files/2014/02/CRM{_}wingboxFEM{_}description{_}1.pdf.

[84] Modern Airliners, *Boeing 777 Specs*, 2020. [Online]. Available: modernairliners.com/boeing-777/boeing-777-specs/ (visited on 11/07/2020).

[85] S Rivers, *Wing box FEM files.* [Online]. Available: https://commonresearchmodel.larc.nasa.gov/fem-file/wingbox-fem-files/ (visited on 12/01/2020).

[86] A. P. Ricciardi, M. J. Patil, R. A. Canfield, and N. Lindsley, "Evaluation of quasi-static gust loads certification methods for high-altitude long-endurance aircraft," *Journal of Aircraft*, vol. 50, no. 2, pp. 457–468, 2013, ISSN: 15333868. DOI: 10.2514/1.C031872.

[87] J. R. R. A. Martins, G. K. W. Kenway, and T. Brooks, "Multidisciplinary Design Optimization of Aircraft Configurations Part 1: A modular coupled adjoint approach," no. May, pp. 1–47, 2016. DOI: 10.13140/RG.2.2.10513.22886.

[88] L. Eca, G Vaz, M Hoekstra, S Pal, E Muller, D Pelletier, A Bertinetti, R Difonzo, L Savoldi, R Zanino, A Zappatore, Y Chen, K Maki, H Ye, J. Drofelnik, B. R. Moss, and A. D. Ronch, "On the Role of Iterative Errors in Unsteady Flow Simulations," *American Society of Mechanical Engineers Journal of Verification, Validation and Uncertainty Quantification (under review)*, vol. 2, pp. 2–7,